TAMPEREEN TEKNILLINEN YLIOPISTO
TAMPERE UNIVERSITY OF TECHNOLOGY

SANTERI LAMPINEN

FORCE-REFLECTED BILATERAL TELEOPERATION OF A HYDRAULIC MANIPULATOR

Master of Science thesis

Examiners: Prof. Jouni Mattila
D. Sc. Janne Koivumäki
Examiners and topic approved by the
Faculty Council of the Faculty of
Engineering Sciences
on 9th August 2017

ABSTRACT

SANTERI LAMPINEN: Force-Reflected Bilateral Teleoperation
of a Hydraulic Manipulator
Tampere University of Technology
Master of Science thesis, 62 pages, 14 Appendix pages
November 2017
Master's Degree Programme in Automation Technology
Major: Fluid Power Automation
Examiners: Prof. Jouni Mattila and D. Sc. Janne Koivumäki
Keywords: Teleoperation, Robotics, Haptic, Model-Based Control, Virtual decomposition control

Teleoperation has been under study from the mid 1940s, when the first mechanical master-slave manipulators were built to allow safe handling of nuclear material within a hot cell. Since then, need to operate within dangerous, out of reach, uncomfortable, or hazardous environments has then motivated researchers to study teleoperation further.

In this thesis, teleoperation of a hydraulic manipulator with electrically driven master manipulator was studied. The workspace of the hydraulic slave manipulator is 5 m in height and it can reach 3 m. The master manipulator has a workspace approximating full arm movement pivoting at the shoulder. Further, the slave manipulator is capable of lifting over 1000 kg, while the master manipulator can lift only 2 kg.

Objective of this thesis is to implement virtual decomposition control (VDC) type controller to the master manipulator and create communication channel for the two manipulators. The VDC approach is a subsystem model based feedforward controller. Similar controller for the slave manipulator has been implemented previously. Performance of the developed teleoperation system will be evaluated with experimental implementation measuring the free space motion tracking in two degrees of freedom motion.

Results from the experimental implementation indicate accurate motion tracking between the two manipulators. Experimental results indicate less than 15 mm position error between the two manipulators, which considering the size of the HIAB can be considered promising.

TIIVISTELMÄ

SANTERI LAMPINEN: Hydraulisen puomin voimatakaisinkytketty etäohjaus
Tampereen teknillinen yliopisto
Diplomityö, 62 sivua, 14 liitesivua
Marraskuu 2017
Automaatiotekniikan koulutusohjelma
Pääaine: Fluid Power Automation
Tarkastajat: Prof. Jouni Mattila ja TkT. Janne Koivumäki
Avainsanat: Etäohjaus, Virtual Decomposition Control, Robotiikka

Teleoperaatiota on tutkitto jo 1940-luvulta lähtien, kun ensimmäiset mekaaniset isäntä-orja manipulaattorit rakennettiin, jotta radioaktiivista materiaalia pystyttiin käsittelemään turvallisesti. Siitä alkaen tarve työskennellä vaarallisissa, epämukavissa tai ihmiselle haitallisissa ympäristöissä on motivoinut etäoperaatiojärjestelmien kehittämisessä.

Tässä työssä tutkitaan hydraulisen puomin etäoperointia sähköisesti ohjatun haptisen manipulaattorin avulla. Työssä tutkitun hydraulisen nostimen ulottuma on jopa neljän metrin korkeuteen ja kolmen metrin päähän poispäin manipulaattorin rungosta. Vastaavasti ohjaimena käytetyn haptisen manipulaattorin työalueen koko muistuttaa ihmisen käden liikettä olkapäästä alkaen. Voimantuotoltaan hydraulinen puomi pystyy helposti tuottamaan jopa 10 000 N voiman, kun taas isäntäohjaimena toimiva haptinen ohjain pystyy tuottamaan maksimissaan 20 N voimia.

Työn tavoitteena on toteuttaa uusi mallipohjainen säätöjärjestelmä, nimeltä Virtual Decomposition Control (VDC), isäntä-manipulaattorina käytetylle haptiselle ohjaimelle. Sen jälkeen manipulaattorit on tarkoitus yhdistää työssä suunnitellun kommunikointilohkon välityksellä toisiinsa toteuttaen teleoperaatiojärjestelmän. Järjestelmän toimivuutta tullaan arvioimaan käytännön kokein, missä isäntä-manipulaattoria käytetään orja-manipulaattorin liikuttamiseen ilmassa.

Kokeellisten mittausten perusteella teleoperaatiojärjestelmän liikkeenseuranta toimii odotetulla tavalla, antaen lupaavia tuloksia. Karteesiseen X-suuntaan saavutettu tarkkuus oli alle 15 mm ja Y-suuntaan alle 5 mm. Ottaen huomioon ohjattavan hydraulisen nostimen työalueen koon, voidaan tuloksia pitää erittäin lupaavina.

PREFACE

I would like to express my deepest gratitude to Professor Jouni Mattila for providing me this opportunity to work on such an interesting and challenging case. Janne Koivumäki deserves my gratitude as well for his guidance and support over this project. I would also like to thank all the staff and my colleagues at the Laboratory of Automation for providing supportive and encouraging working atmosphere.

I also want to thank my parents for encouraging and supporting me for all these years.

Tampere, 22.11.2017

Santeri Lampinen

CONTENTS

LIST OF ABBREVIATIONS AND SYMBOLS

CAD	Computer Aided Design
DH	Denavit-Hartenberg
DOF	Degree of Freedom
PID	Proportional, Integral and Derivative control
VCP	Virtual cutting point
VDC	Virtual decomposition control
VPF	Virtual power flow

α_i	required rotation of the $z_i - 1$-axis about the x_i-axis to become parallel to the z_i-axis, one of the four DH-parameters
α_n	load distribution factor, n $\in \{1, 2\}$
a_i	kinematic length of link i, one of the four DH-parameters
$\{\mathbf{A}\}$	a coordinate system (frame)
$\mathbf{A}_i^{i-1}$	a transformation matrix
$\mathbf{C}$	positive-definite filter coefficient
$\mathbf{C_A}(^{\mathbf{A}}\omega)$	centrifugal and Coriolis forces of rigid body related to frame $\{\mathbf{A}\}$
d_i	distance between axes $x_i - 1$ and x_i along the $z_i - 1$-axis, one of the four DH-parameters
$^{\mathbf{T_{cc}}}\eta$	internal force/moment vector
$^{\mathbf{A}}\boldsymbol{f}$	force vector of frame $\{\mathbf{A}\}$
$^{\mathbf{A}}\boldsymbol{F}$	force/moment vector of frame $\{\mathbf{A}\}$
$^{\mathbf{A}}\boldsymbol{F_r}$	required force/moment vector of frame $\{\mathbf{A}\}$
$^{\mathbf{A}}\boldsymbol{F}^*$	net force/moment vector of frame $\{\mathbf{A}\}$
$\boldsymbol{F}_e$	force exerted from the environment, toward the slave manipulator
$\boldsymbol{F}_h$	force exerted from the operator, toward the master manipulator
g	acceleration due to gravity
$\mathbf{G_A}$	A vector of gravity terms of rigid body related to frame $\{\mathbf{A}\}$
$\mathbf{I_A}$	The moment of inertia related to frame $\{\mathbf{A}\}$
$\mathbf{I_0}(t)$	The moment of inertia matrix around the center of mass
$\mathbf{I_3}(t)$	3×3 identity matrix
$\boldsymbol{J}_D$	displacement Jacobian
$\mathbf{K_A}$	positive definite gain matrix of rigid body related to frame $\{\mathbf{A}\}$
k_x	piston velocity feedback gain of VDC-controller
k_{fp}	piston force feedback gain of VDC-controller
L_p	Lebesgue space, p $\in \{2, \infty\}$
$\mathbf{M_A}$	mass matrix of rigid body related to frame $\{\mathbf{A}\}$

${}^{\mathbf{A}}\boldsymbol{\omega}$	angular velocity related to frame $\{\mathbf{A}\}$
$p_{\mathbf{A}}$	virtual power flow related to frame $\{\mathbf{A}\}$
${}^{\mathbf{A}}\mathbf{R}_{\mathbf{B}}$	a rotation matrix
$({}^{\mathbf{A}}\boldsymbol{r}_{\mathbf{AB}}\times)$	a skew-symmetric matrix operator from vector ${}^{\mathbf{A}}\boldsymbol{r}_{\mathbf{AB}}$
σ_c	binary selective factor defining contact with rigid environment
σ_f	binary selective factor defining contact with flexible environment
$\boldsymbol{\theta}_A$	parameter vector related to frame $\{\mathbf{A}\}$
θ_i	required rotation of $x_i - 1$-axis about the $z_i - 1$ -axis to become parallel to the x_i-axis, one of the four DH-parameters
$\boldsymbol{\tau}_{Mi}$	torque of motor i, i $\in \{1, 2\}$
$\boldsymbol{\tau}_{Mir}$	required torque of motor i, i $\in \{1, 2\}$
${}^{\mathbf{A}}\boldsymbol{U}_{\mathbf{B}}$	transformation matrix used in VDC approach
${}^{\mathbf{A}}\mathbf{v}$	velocity vector related to frame $\{\mathbf{A}\}$
${}^{\mathbf{A}}\boldsymbol{V}$	linear/angular velocity vector related to frame $\{\mathbf{A}\}$
${}^{\mathbf{A}}\boldsymbol{V}_{\boldsymbol{r}}$	required linear/angular velocity vector related to frame $\{\mathbf{A}\}$
$\mathbf{v}_{md}$	desired velocity of the master manipulator
$\mathbf{v}_{sd}$	desired velocity of the slave manipulator
$\mathbf{Y}_{\mathbf{A}}$	regressor matrix related to frame $\{\mathbf{A}\}$
$\boldsymbol{Z}_e$	environmental impedance
$\boldsymbol{Z}_t$	transmitted impedance

1. INTRODUCTION

Robotic manipulators have been under a significant interest after their first introduction in the 1950s, and the popularity of robotics is ever growing. Within the coming decades, robotics research and technology will grow substantially according to euRobotics [1]. The first robots were relatively simple mechanical machines designed for simple material handling tasks where as robotic manipulators nowadays can possess over six degrees of freedom (DOF) and perform tasks ranging from complicated assembly tasks to milling, welding, and measurement, to name a few.

Further, the field of robotics extends to cover some heavy duty hydraulic robotic manipulators used widely in industrial applications. From control perspective, controllers for such manipulators can be designed in a similar way as for more traditional electrically actuated robots. The key difference is the nonlinearities of hydraulic systems that arouses problems and need for a more sophisticated control methods. Hydraulic valves and actuators are highly nonlinear systems that impose difficulties from control aspect. In addition, hydraulic cylinders have high frictions that also contribute to the challenges of controlling hydraulic systems.

Teleoperation and telerobotics is another much studied field of science that started gaining the interest of scientists in mid 1940s, when the need to operate within environments hazardous to humans became necessary. Especially handling of nuclear material was done with teleoperation to avoid harm from radiation [2]. These kind of environments may be within high levels of radiation, extraterrestrial or otherwise dangerous for human health. In addition teleoperated systems may be used to scale human operations to micro and macro environments for accurate and non fatiguing operations.

In order to implement a teleoperation system to any kind of application, control of both the master and the slave manipulator has to be accurate and capable of handling operation in environments specified by the task. Besides accurate and fast control, stability is also required from the control system. In fact stability is the primary requirement of any control system and an unstable system is typically useless and potentially dangerous (see [3], [4]). Control system is needed to produce desired behavior of the manipulator with accurate motion/force control. The most common way to implement controllers for

robotic manipulators is to utilize Proportional, Integral and Derivative (PID) control on each individual actuator of the manipulator. Desired positions for each joint are calculated from the desired manipulator tip position using inverse kinematics functions. PID control is accurate and useful mainly for static operations, where high accuracy is needed for steady state situations. For motion/force tracking applications where high dynamic accuracy is needed, PID control has severe limitations [5, p. 5]. Limitations of PID control became evident especially when fast and accurate motions of the manipulator are required. In such conditions, a more sophisticated approach is required.

Dynamics based control of a robot can be used to accommodate needs of more sophisticated motion/force control of a robot. Such architecture is illustrated in Figure 1.1. In dynamics based control, a feedforward term F(s) is added to act beside feedback control C(s). In ideal case, the feedforward term F(s) is exactly inverse of the controlled plant G(s) for any frequency. Ideal feedforward would further result in infinite control bandwidth [5, p. 6]. In reality, such accuracy for the dynamic model cannot be achieved for complicated systems. The feedback controller C(s) compensates for parametric uncertainties of the feedforward controller and reacts to external disturbances.

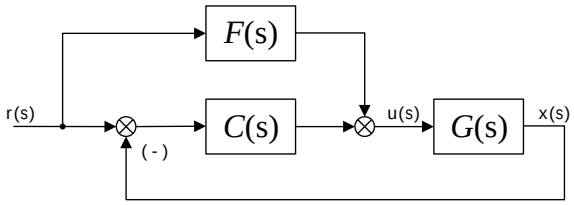

Figure 1.1 *Dynamics based feedforward and PID feedback control system.*

Design of the feedforward term F(s) is completely based on the inverse dynamics of the controlled plant and the feedback controller can be designed independently. Highly coupled nonlinear control systems, such as robotic manipulators, benefit most from dynamics based control systems. Unfortunately complete dynamics of the robot are often hard to model accurately and computational burden of such system grows substantially with the number of DOF. In fact it is shown to grow proportional to the fourth power of the number of DOF of motion, when using Lagrangian dynamics. Another, computationally more efficient, way of modeling the inverse dynamics of a manipulator is the Newton-Euler method.

In this thesis, a novel control design method, called *Virtual Decomposition Control* (VDC) [5], is used to control teleoperated hydraulic robotic manipulators. The key idea behind VDC is to apply dynamics based control to generalized high dimensional robotic system with an arbitrary structure, in a computationally efficient way. Within this thesis the concept of VDC is presented in a simplified form. The complete formulation of VDC for

a general system is given in [5].

With virtual decomposition control, a dynamics based feedforward controller is created independently on a subsystem level, where each rigid link is controlled independently based on it's dynamic behavior. In this way the computational burden remains low, and accuracy of the controller is very high, as shown for electrically driven robots in [6–10] and for hydraulic driven robots in [11–16]. Within this thesis both electric and hydraulic manipulators will be used.

The aim of this thesis is to create a teleoperation system using an electrically operated manipulator to control a heavy-duty hydraulic manipulator. Controllers for both manipulators are implemented using VDC, and the manipulators will be connected with teleoperation scheme, shown in [17]. The Aim of force-reflected bilateral teleoperation is to have a teleoperation system, where the slave manipulator tracks the motion of the master manipulator and allow the human operator to feel the contact forces at the remote environment from the master manipulator [5, p. 303].

Within the scope of this thesis, VDC will be implemented to the master manipulator and a communication channel for the teleoperation system will be designed. The control system of the slave manipulator has been done in [15] and will be used here with minor modifications. Performance of the teleoperation system will be evaluated with experimental trials in free motion and in constrained motion by establishing contact to a flexible environment.

This thesis restricts to cover motion in only 2-DOF planar plane, although theory and the kinematics of the master manipulator are covered for full 6-DOF motion. Further, the stability of the teleoperation system and the master manipulator are not shown within the scope of this thesis, although proven by the VDC approach as shown in [5]. Frictional forces of the master manipulator are also neglected, and rightly so, because the masses of the manipulator are very small. Lastly the communication delay of the teleoperation system is neglected.

The structure of this thesis is divided into six chapters. Chapter 2 introduces the reader with necessary mathematical preliminaries. Chapter 3 shows the steps of application of VDC approach into the Phantom Premium haptic manipulator. First kinematics of the manipulator are covered, followed by introduction and implementation of VDC into the master manipulator. In chapter 4, teleoperation is discussed and the scheme presented in [17] is introduced. Chapter 5 discusses the experimental implementation, where the teleoperation system is experimentally evaluated. In chapter 6, conclusions are drawn and future work is discussed.

2. MATHEMATICAL PRELIMINARIES

In this chapter, mathematical tools and methods, used throughout this thesis, are defined. These mathematical tools are used later in this thesis in the application of virtual decomposition control to the target system. This chapter is largely based on mathematical methods given in [5] and well known books on robotics, [18] and [19].

First coordinate systems, followed by orientation transformation expressions, are introduced. After that, velocity and force expressions in body frame are discussed. This leads to rigid body dynamics expressed in body frame. Mathematical background of virtual decomposition control is also given in this chapter, starting with the concept of virtual decomposition control. Finally, *virtual power flow* is introduced followed by the concept of *virtual stability*.

2.1 Coordinate Systems and Orientation Expressions

Throughout this thesis, coordinate systems, defined in [5, p. 24], are constructed of three mutually orthogonal three-dimensional unit vectors as bases. These coordinate systems are called *frames* for simplicity. According to this definition, frame $\{\mathbf{A}\}$ with its bases denoted as

$$\{\mathbf{A}\} = [\vec{a_x}, \vec{a_y}, \vec{a_z}] \tag{2.1}$$

where $\vec{a_x}, \vec{a_y}, \vec{a_z}$ are individual axes of frame $\{\mathbf{A}\}$.

Definition 2.1. *A three-dimensional vector $\vec{x}$ can be expressed in an arbitrary frame, such as $\{\mathbf{A}\}$, as defined in [5, p. 24], as ${}^{\mathbf{A}}\mathbf{x} = [\vec{a_x} \cdot \vec{x}, \vec{a_y} \cdot \vec{x}, \vec{a_z} \cdot \vec{x}]^T \in \mathbb{R}^3$ subject to*

$$\vec{x} = \{\mathbf{A}\}^{\mathbf{A}}\mathbf{x}. \tag{2.2}$$

Let frames $\{\mathbf{A}\}$ and $\{\mathbf{B}\}$ have common origin and different orientation. Frame $\{\mathbf{A}\}$ is used to express the components of a vector $\vec{x}$. Rotation matrices are used to map the physical vector $\vec{x}$, expressed in frame $\{\mathbf{A}\}$, to the same physical vector expressed in frame $\{\mathbf{B}\}$. In view of Definition 2.1, vector $\vec{x}$ can be expressed in frame $\{\mathbf{B}\}$ as ${}^{B}\mathbf{x} = \mathbf{A}\mathbf{R}_{\mathbf{B}}{}^{A}\mathbf{x}$.

In a more general format, rotation transformation can be expressed as

$$\{\mathbf{B}\} = \mathbf{A}\mathbf{R}_\mathbf{B}\{\mathbf{A}\} \tag{2.3}$$

where ${}^{A}\mathbf{R}_{B} \in \mathbb{R}^{3\times3}$ denotes a rotation matrix connecting frame $\{\mathbf{A}\}$ with frame $\{\mathbf{B}\}$. [5, p. 25]

Within the scope of this thesis, all frames will be applied in such a way, that rotations between two consecutive frames, namely $\{\mathbf{A}\}$ and $\{\mathbf{B}\}$, can be described with at most two rotations, one about the Z-axis and one about the X-axis respectively. In view of [18, p. 23], rotation of θ about z-axis can be expressed as

$$\mathbf{{}^{A}R_{B}} = \begin{bmatrix} cos(\theta) & -sin(\theta) & 0 \\ sin(\theta) & cos(\theta) & 0 \\ 0 & 0 & 1 \end{bmatrix} \tag{2.4}$$

and correspondingly rotation about x-axis can be described as

$$\mathbf{{}^{A}R_{B}} = \begin{bmatrix} 1 & 0 & 0 \\ 0 & cos(\alpha) & -sin(\alpha) \\ 0 & sin(\alpha) & cos(\alpha) \end{bmatrix} \tag{2.5}$$

where α denotes rotation of frame $\{\mathbf{B}\}$ with respect to frame $\{\mathbf{A}\}$.

2.2 Denavit-Hartenberg Convention

Denavit-Hartenberg (DH) convention, later called DH-convention, is a general method used to define relative position and orientation of two consecutive links systematically [18, p. 43]. With this information, it is possible to calculate direct kinematics equations for an open-chain manipulator.

Calculating forward kinematics to a manipulator, composed of successive rigid links, begins with identifying the links and the joints of the manipulator. In the scope of this thesis, only revolute joints are considered, and so the only joint variable needed is the revolution angle, θ_i, around the rotation-axis, which in DH-convention is always the z-axis. To define DH-parameters for a manipulator, four parameter, namely $a_i, \alpha_i, d_i, \theta_i$, need to be defined for each successive coordinate frame. These parameters define rigid transformation between neighboring rigid links. Figure 2.1 defines these parameters in a general case of revolute joint.

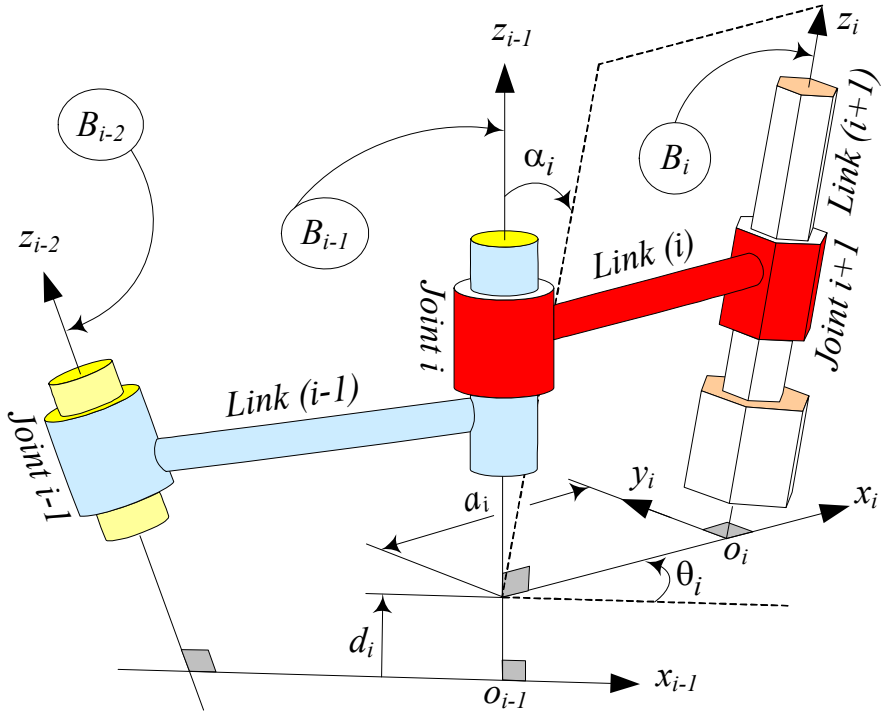

Figure 2.1 *DH parameters α_i, a_i, θ_i and d_i defined for joint i and link i [19, p. 236].*

According to [19, p. 235], the DH-parameters can be defined as in the following manner:

- a_i Distance between axes $z_i - 1$ and z_i along the x_i -axis. a_i is the kinematic length of link (i).
- α_i Required rotation of the $z_i - 1$-axis about the x_i-axis to become parallel to the z_i-axis.
- d_i Distance between axes $x_i - 1$ and x_i along the $z_i - 1$-axis.
- θ_i Required rotation of $x_i - 1$-axis about the $z_i - 1$ -axis to become parallel to the x_i-axis.

According to [18, p.45], the transformation matrix between each link can be formed from the DH-parameters as

$$\mathbf{A}_i^{i-1} = \begin{bmatrix} c\alpha_i & -s\theta_i c\alpha_i & s\theta_i s\alpha_i & a_i c\theta_i \\ s\alpha_i & c\theta_i c\alpha_i & -c(\theta_i)s(\alpha_i) & a_i s\theta_i \\ 0 & s\alpha_i & c\alpha_i & d_i \\ 0 & 0 & 0 & 1 \end{bmatrix}, \tag{2.6}$$

where i is the order number of the link, $c\alpha_i$ is $cos\ \alpha_i$, $s\alpha_i$ is $sin\ \alpha_i$, $c\theta_i$ is $cos\ \theta_i$ and $s\theta_i$ is $sin\ \theta_i$.

Transformation matrix, in Equation 2.6, comprises of rotation matrix and translation vector with respect to the original coordinate frame $\{O_{i-1}\}$. To calculate the total transformation between multiple links, only multiplication of single transformation matrices is required, as defined in [18, p. 42]

$$\mathbf{A}_n^0(\theta) = \mathbf{A}_1^0(\theta_1)\mathbf{A}_2^1(\theta_2)...\mathbf{A}_n^{n-1}(\theta_n) \tag{2.7}$$

where θ_i is the rotation of joint i.

2.3 Expressions of Velocity and Force Vectors

Let an arbitrary frame $\{A\}$ be attached to a rigid body, and let $\vec{f_A} \in \mathbb{R}^3$ and $\vec{m_A} \in \mathbb{R}^3$ be directed vectors representing the force and moment applied to the origin of frame $\{A\}$. Further, let $\vec{v_A} \in \mathbb{R}^3$ and $\vec{\omega_A} \in \mathbb{R}^3$ be directed vectors representing the linear and angular velocities of frame $\{A\}$.

For convenience and simplicity, linear and angular velocities, as well as forces and moments, are integrated into linear/angular velocity vector and force/moment vector, in order to ease the transformations of velocities and forces/moments among different frames [5, p. 29]. Considering the VDC approach, this notation is useful in transformations among different frames, as will be seen in subsection 2.4. According to [5, p. 29], the following two definitions are used to define these velocity and force vectors.

Definition 2.2. *Let ${}^A v \in \mathbb{R}^3$ and ${}^A\omega \in \mathbb{R}^3$ be the linear and angular velocity vectors of frame $\{A\}$, expressed in frame $\{A\}$, respectively. The linear/angular velocity vector in frame $\{A\}$ is defined by*

$${}^A V \stackrel{\text{def}}{=} \begin{bmatrix} {}^A v \\ {}^A\omega \end{bmatrix} \in \mathbb{R}^6. \tag{2.8}$$

Definition 2.3. *Let ${}^A f \in \mathbb{R}^3$ and ${}^A m \in \mathbb{R}^3$ be the force and moment vectors measured and expressed in frame $\{A\}$, respectively. The force/moment vector in frame $\{A\}$ is defined by*

$${}^A F \stackrel{\text{def}}{=} \begin{bmatrix} {}^A f \\ {}^A m \end{bmatrix} \in \mathbb{R}^6. \tag{2.9}$$

2.4 The Duality of Linear/Angular Velocity and Force/Moment Transformations

Consider a rigid freely moving body, subject to a pair of physical force and moment vectors. Let frame $\{\mathbf{A}\}$ and $\{\mathbf{B}\}$ be fixed to the rigid body. According to [5, p. 29] and [18, p. 120], the following relations hold

$$^{\mathbf{B}}\boldsymbol{V} = {}^{\mathbf{A}}\boldsymbol{U}_{\mathbf{B}}^{T}\,{}^{\mathbf{A}}\boldsymbol{V} \tag{2.10}$$

$$^{\mathbf{A}}\boldsymbol{F} = {}^{\mathbf{A}}\boldsymbol{U}_{\mathbf{B}}\,{}^{\mathbf{B}}\boldsymbol{F}, \tag{2.11}$$

where

$$^{\mathbf{A}}\boldsymbol{U}_{\mathbf{B}} = \begin{bmatrix} {}^{\mathbf{A}}\mathbf{R}_{\mathbf{B}} & \mathbf{0}_{3\times3} \\ ({}^{\mathbf{A}}\boldsymbol{r}_{\mathbf{AB}}\times){}^{\mathbf{A}}\mathbf{R}_{\mathbf{B}} & {}^{\mathbf{A}}\mathbf{R}_{\mathbf{B}} \end{bmatrix} \in \mathbb{R}^{6\times6} \tag{2.12}$$

denotes a force/moment transformation matrix, which transforms the force/moment vector, measured and expressed in frame $\{B\}$, to the same force/moment vector, measured and expressed in frame $\{A\}$. Further, in (2.12), $\mathbf{0}_{3\times3}$ denotes an empty 3×3 square matrix, and ${}^{\mathbf{A}}\boldsymbol{r}_{\mathbf{AB}} \in \mathbb{R}^{3\times3}$ denotes a vector from the origin of frame $\{\mathbf{A}\}$ to the origin of frame $\{\mathbf{B}\}$, expressed in frame $\{\mathbf{A}\}$. The cross product $({}^{\mathbf{A}}\boldsymbol{r}_{\mathbf{AB}}\times) \in \mathbb{R}^{3\times3}$ denotes skew-symmetric matrix defined as

$$({}^{\mathbf{A}}\boldsymbol{r}_{\mathbf{AB}}\times) = \begin{bmatrix} 0 & -r_z & r_y \\ r_z & 0 & -r_x \\ -r_y & r_x & 0 \end{bmatrix} \tag{2.13}$$

where r_x, r_y and r_z are the distances from origin of frame $\{\mathbf{A}\}$ to the origin of frame $\{\mathbf{B}\}$, along the axes of frame $\{\mathbf{A}\}$ [20, p. 158].

By taking the inverse of the transformation matrix, defined in (2.12), the transformation matrix can be written as

$$^{\mathbf{A}}\boldsymbol{U}_{\mathbf{B}}^{-1} = \begin{bmatrix} {}^{\mathbf{A}}\mathbf{R}_{\mathbf{B}}^{T} & \mathbf{0}_{3\times3} \\ -{}^{\mathbf{A}}\mathbf{R}_{\mathbf{B}}^{T}({}^{\mathbf{A}}\boldsymbol{r}_{\mathbf{AB}}\times) & {}^{\mathbf{A}}\mathbf{R}_{\mathbf{B}}^{T} \end{bmatrix} \in \mathbb{R}^{6\times6}\,. \tag{2.14}$$

With equation (2.14), linear/angular velocity and force/moment transformations, defined in (2.10) and (2.11), can be inversely written as

$$^{\mathbf{A}}\boldsymbol{V} = {}^{\mathbf{A}}\boldsymbol{U}_{\mathbf{B}}^{-T}\,{}^{\mathbf{B}}\boldsymbol{V} \tag{2.15}$$

$$^{\mathbf{B}}\boldsymbol{F} = {}^{\mathbf{A}}\boldsymbol{U}_{\mathbf{B}}^{-1}\,{}^{\mathbf{A}}\boldsymbol{F}, \tag{2.16}$$

respectively. This property is called *kineto-statics duality* [18, p.118].

2.5 Rigid Body Dynamics in a Body Frame

This section defines required expressions needed to calculate rigid body dynamics in a body frame for a single rigid body. In order to define required expressions, a net force/-moment vector, similar to Definition 2.3, needs to be defined.

Let frame $\{\mathbf{A}\}$ be attached to a rigid body. According to [5, p. 30], the net force and moment vectors applied to frame $\{\mathbf{A}\}$ can be defined as

$$\vec{f}^{*}_{\mathbf{A}} = \{\mathbf{A}\}^{\mathbf{A}} f^{*} \tag{2.17}$$

$$\vec{m}^{*}_{\mathbf{A}} = \{\mathbf{A}\}^{\mathbf{A}} m^{*}, \tag{2.18}$$

where $\vec{f}^{*}_{\mathbf{A}}$ and $\vec{m}^{*}_{\mathbf{A}}$ denotes the sum of all force and moment vectors applied to the rigid body, respectively, then ${}^{\mathbf{A}}f^{*} \in \mathbb{R}^3$ and ${}^{\mathbf{A}}m^{*} \in \mathbb{R}^3$ denotes the same force and moment vectors expressed in frame $\{\mathbf{A}\}$, accordingly.

Definition 2.4. *Let ${}^{\mathbf{A}}f^{*} \in \mathbb{R}^3$ and ${}^{\mathbf{A}}m^{*} \in \mathbb{R}^3$ be the net force and moment vectors exerted to a rigid body and being measured and expressed in a body frame $\{\mathbf{A}\}$,respectively. The net force/moment vector of the rigid body in frame $\{\mathbf{A}\}$ is defined in [5, p. 30] as*

$${}^{\mathbf{A}}\boldsymbol{F}^{*} \overset{\text{def}}{=} \begin{bmatrix} {}^{\mathbf{A}}f^{*} \\ {}^{\mathbf{A}}m^{*} \end{bmatrix} \in \mathbb{R}^6. \tag{2.19}$$

With the net force/moment vector defined, necessary tools for rigid body dynamics are obtained. To define dynamics equations, two frames, namely $\{\mathbf{A}\}$ and $\{\mathbf{B}\}$, are considered and they are attached to a rigid object. Frame $\{\mathbf{B}\}$ is assumed to be at the center of mass, and frame $\{\mathbf{A}\}$ is used to express the dynamics equations. According to [5, p. 31], the rigid body dynamics can be expressed as

$$\mathbf{M}_{\mathbf{A}} \frac{d}{dt}({}^{\mathbf{A}}\boldsymbol{V}) + \mathbf{C}_{\mathbf{A}}({}^{\mathbf{A}}\omega)\,{}^{\mathbf{A}}\boldsymbol{V} + \mathbf{G}_{\mathbf{A}} = {}^{\mathbf{A}}\boldsymbol{F}^{*}, \tag{2.20}$$

where $\mathbf{M}_{\mathbf{A}}$ denotes the mass matrix, $\mathbf{C}_{\mathbf{A}}$ Coriolis and centrifugal forces, and $\mathbf{G}_{\mathbf{A}}$ the gravity term of the rigid body. These terms are formed as

$$\mathbf{M}_{\mathbf{A}} = \begin{bmatrix} m_{\mathbf{A}}\mathbf{I}_3 & -m_{\mathbf{A}}({}^{\mathbf{A}}r_{\mathbf{AB}}\times) \\ m_{\mathbf{A}}({}^{\mathbf{A}}r_{\mathbf{AB}}\times) & \mathbf{I}_{\mathbf{A}} - m_{\mathbf{A}}({}^{\mathbf{A}}r_{\mathbf{AB}}\times)^2 \end{bmatrix} \in \mathbb{R}^{6\times 6} \tag{2.21}$$

$$\mathbf{C}_{\mathbf{A}} = \begin{bmatrix} \mathbf{C}_{11} & \mathbf{C}_{12} \\ \mathbf{C}_{21} & \mathbf{C}_{22} \end{bmatrix} \in \mathbb{R}^{6\times 6} \tag{2.22}$$

$$\mathbf{G}_{\mathbf{A}} = \begin{bmatrix} m_{\mathbf{A}}\,{}^{\mathbf{A}}\mathbf{R}_{\mathbf{I}}\,\mathbf{g} \\ m_{\mathbf{A}}({}^{\mathbf{A}}r_{\mathbf{AB}}\times)\,{}^{\mathbf{A}}\mathbf{R}_{\mathbf{I}}\,\mathbf{g} \end{bmatrix} \in \mathbb{R}^{6\times 1}. \tag{2.23}$$

In (2.21) – (2.23), $\mathbf{I}_3 \in \mathbb{R}^{3\times3}$ denotes 3×3 identity matrix, $m_\mathbf{A}$ the mass of the rigid body, $\mathbf{g} \in \mathbb{R}^3$ the gravitational vector, and $\mathbf{I_A} \in \mathbb{R}^{3\times3}$ the inertial matrix around frame $\{A\}$, which is defined as

$$\mathbf{I_A} = {}^\mathbf{A}\mathbf{R_I}\mathbf{I_0}(t){}^\mathbf{I}\mathbf{R_A}, \tag{2.24}$$

where $\mathbf{I_0}(t) \in \mathbb{R}^{3\times3}$ denotes the inertia tensor around the center of mass. Furthermore, in (2.22), $\mathbf{C}_{11}$, $\mathbf{C}_{12}$, $\mathbf{C}_{21}$, and $\mathbf{C}_{22}$ are defined as

$$\mathbf{C}_{11} = m_\mathbf{A}({}^\mathbf{A}\omega\times) \tag{2.25}$$
$$\mathbf{C}_{12} = -m_\mathbf{A}({}^\mathbf{A}\omega\times)({}^\mathbf{A}\boldsymbol{r}_\mathbf{AB}\times) \tag{2.26}$$
$$\mathbf{C}_{21} = m_\mathbf{A}({}^\mathbf{A}\boldsymbol{r}_\mathbf{AB}\times)({}^\mathbf{A}\omega\times) \tag{2.27}$$
$$\mathbf{C}_{22} = ({}^\mathbf{A}\omega\times)\mathbf{I_A} + \mathbf{I_A}({}^\mathbf{A}\omega\times) - m_\mathbf{A}({}^\mathbf{A}\boldsymbol{r}_\mathbf{AB}\times)({}^\mathbf{A}\omega\times)({}^\mathbf{A}\boldsymbol{r}_\mathbf{AB}\times) \tag{2.28}$$

where $({}^\mathbf{A}\omega\times)$ denotes a skew-symmetric matrix representing angular velocities.

Finally, a linear parametrization expression can be formed from (2.20) to be used by parameter adaption to compensate parametric uncertainties and errors. Let ${}^\mathbf{A}V_r \in \mathbb{R}^6$ be the required vector of ${}^\mathbf{A}V \in \mathbb{R}^6$. According to [5, p. 32] the following expression is defined

$$\mathbf{Y_A}\boldsymbol{\theta}_\mathbf{A} \overset{def}{=} \mathbf{M_A}\frac{d}{dt}({}^\mathbf{A}V_r) + \mathbf{C_A}({}^\mathbf{A}\omega){}^\mathbf{A}V_r + \mathbf{G_A}. \tag{2.29}$$

Regressor matrix $\mathbf{Y_A} \in \mathbb{R}^{6\times13}$ and the parameter vector $\boldsymbol{\theta}_\mathbf{A} \in \mathbb{R}^{13}$ are presented in [5], Appendix A.

2.6 Virtual Cutting Points and Oriented Graphs

Before the concept of virtual decomposition control can be introduced, two important concepts, used in virtual decomposition control, needs to be introduced first. The concept of a virtual *cutting point* allows decomposition of a complex robotic manipulator into subsystems. Definition for the cutting point is given in [5, p. 34] as

Definition 2.5. *A cutting point is a directed separation interface that conceptually cuts through a rigid body. At the cutting point, the two parts resulting from the virtual cut maintain equal position and orientation. The cutting point is interpreted as a driving cutting point by one part and is simultaneously interpreted as a driven cutting point by another part. A force vector $f \in \mathbb{R}^3$ and a moment vector $m \in \mathbb{R}^3$ are exerted from one part to which the cutting point is interpreted as a driving cutting point to the other part to which the cutting point is interpreted as a driven cutting point.*

With the help of virtual cutting points, a complex robot can be broken down into smaller components. To represent the topological structure and the control relations of the decomposed robot, a simple oriented graph is used. A simple oriented graph is define in [5, p. 34] as

Definition 2.6. *A graph consists of nodes and edges. A directed graph is a graph in which all the edges have directions. An oriented graph is a directed graph in which each edge has a unique direction. A simple oriented graph is an oriented graph in which no loop is formed. [21]*

Structure of the decomposed system is expressed with a simple oriented graph so that each virtual cutting point represent a directed edge and each subsystem represent a node in the graph.

2.7 Virtual Stability

Finally, after the system is virtually decomposed into subsystems, concept of *virtual stability* can be considered. Before introducing virtual stability, concepts of *non-negative accompanying functions* and *virtual power flow* are introduced. In addition, Lebesgue space is introduced as a mathematical method for proving stability of the system.

2.7.1 Non-negative Accompanying Function

A non-negative accompanying function is assigned to each subsystem of the virtually cut complex robot to conduct stability and convergence analysis. The following definition for non-negative accompanying function $\nu(t) \in \mathbb{R}$ is given in [5, p. 35].

Definition 2.7. *A non-negative accompanying function $\nu(t) \in \mathbb{R}$ is a piecewise differentiable function possessing the following properties:*

(i) *$\nu(t) \geq 0$ for $t > 0$, and*

(ii) *$\dot{\nu}(t)$ exists almost everywhere.*

2.7.2 Virtual Power Flow

Dynamic interactions between successive subsystems are characterized by *virtual power flows* (VPFs). Virtual power flow is defined in [5, p. 35] as

Definition 2.8. *With respect to frame* $\{\mathbf{A}\}$*, the virtual power flow (VPF) is defined as the inner product of the linear/angular velocity vector error and the force/moment vector error, that is*

$$p_{\mathbf{A}} \stackrel{\text{def}}{=} ({}^{\mathbf{A}}\boldsymbol{V}_r - {}^{\mathbf{A}}\boldsymbol{V})^T({}^{\mathbf{A}}\boldsymbol{F}_r - {}^{\mathbf{A}}\boldsymbol{F}) \tag{2.30}$$

where ${}^{\mathbf{A}}\boldsymbol{V}_r \in \mathbb{R}^6$ *and* ${}^{\mathbf{A}}\boldsymbol{F}_r \in \mathbb{R}^6$ *denotes the required vectors of* ${}^{\mathbf{A}}\boldsymbol{V} \in \mathbb{R}^6$ *and* ${}^{\mathbf{A}}\boldsymbol{F} \in \mathbb{R}^6$*, respectively.*

Consider two frames, $\{\mathbf{A}\}$ and $\{\mathbf{B}\}$, being attached to a common rigid body. Assuming that the same constraints hold for the linear/angular velocity vector and force/moment vector as hold their required counterparts. From this follows

$${}^{\mathbf{B}}\boldsymbol{V}_r = {}^{\mathbf{A}}\mathbf{U}_{\mathbf{B}}^T{}^{\mathbf{A}}\boldsymbol{V}_r \tag{2.31}$$

$${}^{\mathbf{A}}\boldsymbol{F}_r = {}^{\mathbf{A}}\mathbf{U}_{\mathbf{B}}{}^{\mathbf{B}}\boldsymbol{F}_r \tag{2.32}$$

then it follows from (2.10), (2.11) and (2.30) – (2.32) that

$$p_{\mathbf{A}} = p_{\mathbf{B}} \tag{2.33}$$

holds as well. This result indicates that the VPF defined by (2.30) is invariant to frames fixed to a common rigid body. [5, p. 30]

2.7.3 Lebesgue Space

Lebesgue spaces are essential in proving the virtual stability, and therefore necessary to cover to some extent. The following two definitions are given in [5, p. 16]

Definition 2.9. *Lebesgue space, denoted as* L_p *with p being a positive integer, contains all Lebesgue measurable and integrable functions f(t) subject to*

$$\|f\|_p = \lim_{T\to\infty}\left[\int_0^T |f(t)|^p d\tau\right]^{\frac{1}{p}} < +\infty. \tag{2.34}$$

Definition 2.10. *A vectored Lebesgue measurable function* $\boldsymbol{f}(t) = [f_1(t), f_2(t), \dots f_n(t)]^T \in L_p, p = 1, 2, \dots, \infty$*, implies* $f_i(t) \in L_p$ *for all* $i \in \{1, n\}$.

Especially two particular cases, L_2 and L_∞, are important considering virtual stability. The following cases are given in [5, p. 16]:

(a) A Lebesgue measurable function $f(t)$ belongs to L_2 if and only if $\lim_{T\to\infty}\int_0^T |f(t)|^2\, d\tau < +\infty$

(b) A Lebesgue measurable function $f(t)$ belongs to L_∞ if and only if $\max_{t\in[0,\infty)} |f(t)| < +\infty$

2.7.4 Virtual Stability

Finally, after the system is virtually decomposed into subsystems and all the necessary mathematical methods and relevant concepts are defined, concept of *virtual stability* can be considered. The following definition, given in [5, p. 36], defines virtual stability that eventually is used to proof the stability of the whole complex robot.

Definition 2.11. *A subsystem that is virtually decomposed from a complex robot is said to be virtually stable with its affiliated vector $\mathbf{x}(t)$ being a virtual function in L_∞ and its affiliated vector $\mathbf{y}(t)$ being a virtual function in L_2, if and only if there exists a non-negative accompanying function*

$$\nu(t) \geq \frac{1}{2}\mathbf{x}(t)^T\mathbf{P}\mathbf{x}(t) \tag{2.35}$$

such that

$$\dot{\nu}(t) \leq -\mathbf{y}(t)^T\mathbf{Q}\mathbf{y}(t) - s(t) + \sum_{\{\mathbf{A}\}\in\Phi} p_{\mathbf{A}} - \sum_{\{\mathbf{C}\}\in\Psi} p_{\mathbf{C}} \tag{2.36}$$

holds, subject to

$$\int_0^T s(t)d\tau \geq -\gamma_s \tag{2.37}$$

with $0 \leq \gamma_s \leq \infty$, where $\boldsymbol{P}$ and $\boldsymbol{Q}$ are two block-diagonal positive-definite matrices, set Φ contains frames being placed at the driven cutting points of this subsystem and set Ψ contains frames being placed at the driving cutting points of this subsystem, and $p_{\mathbf{A}}$ and $p_{\mathbf{C}}$ denote the virtual power flows in Definition 2.8.

It should be noted that the *virtual stability* requires the appearance of VPFs in the time derivative of the non-negative accompanying function for each subsystem [5, p. 37]. To show that two adjacent subsystems are *virtually stable* and also equivalent to a single *virtually stable* subsystem, Zhu has given the following Lemma in [5, p 37] as

Lemma 2.1. *Every two adjacent subsystem that are virtually stable can be equivalent to a single subsystem that is virtually stable in the sense of Definition 2.11. Every virtual function in L_p affiliated with any one of the two adjacent subsystem remains to be a virtual function in L_p affiliated with the equivalent subsystem for $p = 2, \infty$.*

Proof for Lemma 2.1 has been shown in [5, p 37].

When virtual stability of every subsystem has been proven in the sense of Definition 2.11, the following theorem has been given and proven in [5, p. 38], to guarantee that the entire complex robot is L_2 and L_∞ stable.

Theorem 2.1. *Consider a complex robot that is virtually decomposed into subsystems and is represented by a simple oriented graph in Definition 2.6. If every subsystem is virtually stable in the sense of Definition 2.11, then all virtual functions in L_2 are functions in L_2 and all virtual functions in L_∞ are functions in L_∞.*

Theorem 2.1 is the single most important theorem of VDC. According to the theorem, equivalence of *virtually stability* of every subsystem, and further the stability of the entire system is established. With this theorem, stability of the entire system can be proven by proving each subsystem to be *virtually stable*. Theorem 2.1 can be considered as the theoretical foundation of the *virtual decomposition control*. [5, p.40]

3. APPLYING THEORY TO TARGET SYSTEM

In this chapter, virtual decomposition control is applied to the Phantom Premium 3.0L 6 DOF manipulator. Phantom Premium is a haptic manipulator, designed and manufactured by former SensAble Technologies, recently acquired by 3D Systems. The manipulator has 6 DOF movement, with a workspace area approximating full arm movement pivoting at the shoulder. In addition, a force-feedback can be applied around all six DOF. An illustrative picture of the haptic device is presented on Figure 3.1. The device consists of successive rigid links and one closed kinematic chain. Operating each joint and providing the force-feedback is six electric motors with their respective amplifiers and control electronics located inside the base of the device. Within the scope of this thesis, only joint 2 and 3 are actuated, while the rest are considered rigid and unactuated. However, the kinematics for the manipulator are presented without any simplifications to help future work with the manipulator.

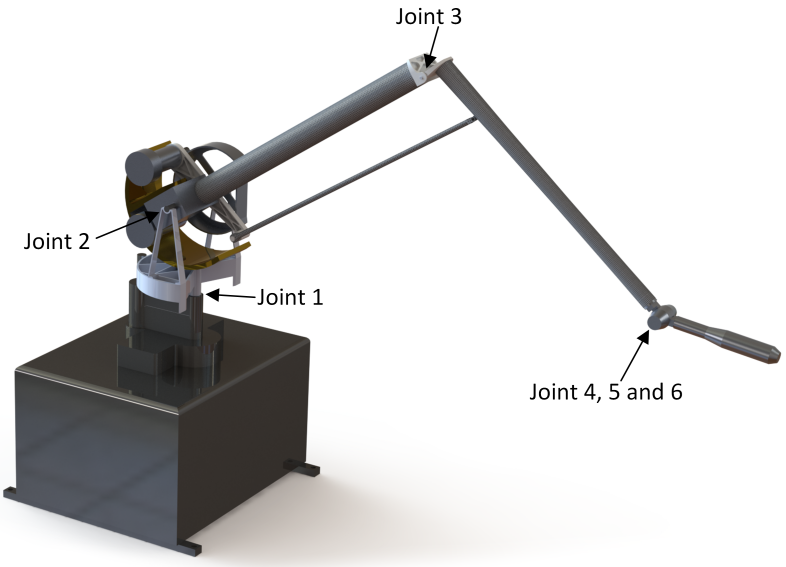

Figure 3.1 *Phantom Premium*

One assumption of VDC is that the kinematics of the target system are known. Kinematics of the phantom premium are therefore discussed first, and after that virtual decomposition of the haptic device is discussed. Finally, a force estimation method for the exogenous force of the manipulator is outlined.

3.1 Kinematics of Phantom Premium 3.0/6DOF

Kinematics of the Phantom Premium are calculated using DH-parameters, that are obtained by manual measurements of the haptic device. The device consists of only rigid links and revolute joints, which makes the parametrization and determination of frames straightforward. Figure 3.2 illustrates joint locations and link lengths of the haptic device. The unit of lenghts in the figure is mm.

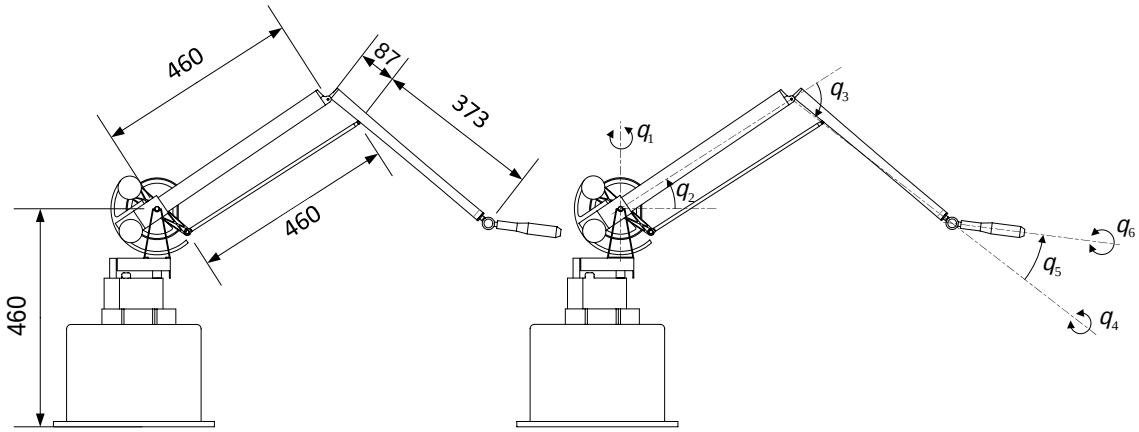

Figure 3.2 *Joints and dimensions of the Phantom Premium*

Coordinate frames of the system are determined according to the DH-convention and right hand rule. All angles are set to be positive counter-clockwise. Selected coordinate frames of the Phantom Premium are illustrated in Figure 3.3. DH-parameters are formed between these frames so that the overall transformation is the same whether calculated through any one of the possible routes at the closed kinematic chain. Identified DH-parameters for the target manipulator are presented in Table 3.1, where link *2'* and *3'* denote alternative kinematic route from frame $\{\mathbf{B_1}\}$ to $\{\mathbf{T_{cc}}\}$.

Table 3.1 *DH-parameters of Phantom Premium*

Link	$a\ [mm]$	α	$v\ [mm]$	ν	*End frame*
1	0	90	460	θ_1	$\{\mathbf{B_1}\}$
2	460	0	0	θ_2	$\{\mathbf{B_{12}}\}$
3	87	0	0	θ_3	$\{\mathbf{T_{cc}}\}$
2'	87	0	0	$\theta_1 + \theta_3$	$\{\mathbf{B_{22}}\}$
3'	460	0	0	θ_3	$\{\mathbf{T_{cc}}\}$
4	373	0	0	0	$\{\mathbf{S_{tcp}}\}$
5	0	-90	0	θ_4	
6	0	90	0	θ_5	
7	0	0	0	θ_6	$\{\mathbf{T_{tcp}}\}$

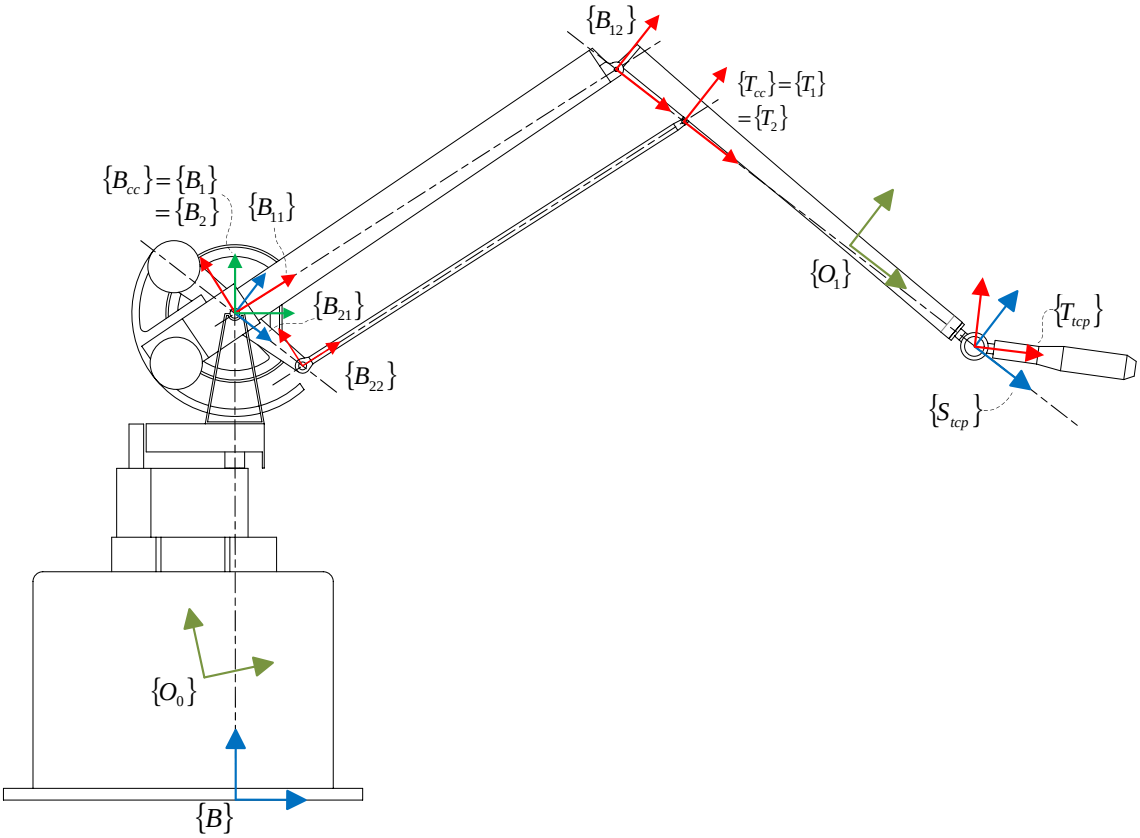

Figure 3.3 *Phantom Coordinate Frames*

Kinematics of the studied manipulator are divided into two parts; forward kinematics and differential kinematics. These can be computed with the help of DH-parameters presented in Table 3.1.

3.1.1 Forward Kinematics

Forward kinematics are used to determine the position and orientation of the end effector with respect to the base frame as a function of the joint space variables, $\theta_1 - \theta_6$ [19, p. 259]. Having DH-parameters identified for the studied manipulator, forward kinematics for each link can be calculated using (2.6). After calculating transformation matrix for each consecutive links, forward kinematics for the entire manipulator can be calculated according to (2.7).

Formulation of the full transformation matrix for the manipulator is presented in Appendix B, and here is presented only equations for calculating the end effector position

expressed in frame $\{\mathbf{B}\}$, using the joint angles θ_1 – θ_3.

$$p_x = l_1 \cos(\theta_1)\left(\cos(\theta_2+\theta_3)+\cos(\theta_2)\right) \tag{3.1}$$

$$p_y = l_1\left(\sin(\theta_2+\theta_3)+\sin(\theta_2)+1\right) \tag{3.2}$$

$$p_z = l_1 \sin(\theta_1)\left(\cos(\theta_2+\theta_3)+\cos(\theta_2)\right), \tag{3.3}$$

where $l_1 = 460mm$.

Within the scope of this thesis, joints θ_1, θ_4, θ_5 and θ_6 are considered fixed. The transformation matrix for end effector position and rotation can thus be simplified from the full 6 DOF form that was presented in Appendix B. With this simplification, the transformation matrix can be written as

$$\boldsymbol{A}^{\mathbf{B}}_{\mathbf{S_{tcp}}} = \begin{bmatrix} {}^{\mathbf{B}}\mathbf{R}_{\mathbf{T_{tcp}}} & \boldsymbol{p}_{\mathbf{S_{tcp}}} \\ 0 \quad 0 \quad 0 & 1 \end{bmatrix}, \tag{3.4}$$

where

$${}^{\mathbf{B}}\mathbf{R}_{\mathbf{T_{tcp}}} = \begin{bmatrix} \cos(\theta_2+\theta_3) & -\sin(\theta_2+\theta_3) & 0 \\ \sin(\theta_2+\theta_3) & \cos(\theta_2+\theta_3) & 0 \\ 0 & 0 & 1 \end{bmatrix} \tag{3.5}$$

and

$$\boldsymbol{p}_{\mathbf{S_{tcp}}} = \begin{bmatrix} p_x \\ p_y \\ p_z \end{bmatrix} = \begin{bmatrix} l_1\left(\cos(\theta_2+\theta_3)+\cos(\theta_2)\right) \\ l_1\left(\sin(\theta_2+\theta_3)+\sin(\theta_2)+1\right) \\ 0 \end{bmatrix} \tag{3.6}$$

Remark 3.1. *With the simplification of the manipulator kinematics, frames* $\{\mathbf{T_{tcp}}\}$ *and* $\{\mathbf{S_{tcp}}\}$ *become aligned with each other.*

Orientation of the end effector with respect to frame $\{\mathbf{B}\}$ can be determined with equation (3.5) and position of the end effector with respect to frame $\{\mathbf{B}\}$ can be determined using (3.6).

3.1.2 Differential Kinematics

With forward differential kinematics, end effector velocity can be determined from the joint velocities, and inversely joint velocities can be identified from end effector velocity [19, p. 442,465]. The relationship between end effector orientation and position and the

joint variables can be derived by differentiating the forward kinematic equations presented in (3.6) with respect to the joint variables [18, p. 79].

This relationship is called displacement Jacobian, $\boldsymbol{J}_D$ [19, p. 444], or geometric Jacobian, $\boldsymbol{J}_P$ [18, p. 79], and it can be determined as

$$\boldsymbol{J}_D = \begin{bmatrix} \frac{\partial p_x}{\partial \theta_1} & \frac{\partial p_x}{\partial \theta_2} & \frac{\partial p_x}{\partial \theta_3} \\ \frac{\partial p_y}{\partial \theta_1} & \frac{\partial p_y}{\partial \theta_2} & \frac{\partial p_y}{\partial \theta_3} \\ \frac{\partial p_z}{\partial \theta_1} & \frac{\partial p_z}{\partial \theta_2} & \frac{\partial p_z}{\partial \theta_3} \end{bmatrix} \tag{3.7}$$

The displacement Jacobian is presented in Appendix B in its full form without simplifications. With the joint variable θ_1 assumed rigid, the Jacobian is simplified to the following form

$$\begin{aligned} \boldsymbol{J}_D &= \begin{bmatrix} \frac{\partial p_x}{\partial \theta_2} & \frac{\partial p_x}{\partial \theta_3} \\ \frac{\partial p_y}{\partial \theta_2} & \frac{\partial p_y}{\partial \theta_3} \end{bmatrix} \\ &= \begin{bmatrix} -l_1 \ (\sin(\theta_2 + \theta_3) + \sin(\theta_2)) & -l_1 \ \sin(\theta_2 + \theta_3) \\ l_1 \ (\cos(\theta_2 + \theta_3) + \cos(\theta_2)) & l_1 \ \cos(\theta_2 + \theta_3) \end{bmatrix} \end{aligned} \tag{3.8}$$

Using equation (3.8) and according to [19, p. 442], the linear velocity of the end effector can be calculated from the joint variables as

$$\dot{\boldsymbol{p}}_{\mathbf{S_{tcp}}} = \boldsymbol{J}_D \dot{\boldsymbol{\theta}}, \tag{3.9}$$

where $\dot{\boldsymbol{p}}_{\mathbf{S_{tcp}}} = [\,\dot{p}_x \quad \dot{p}_z]^T \in \mathbb{R}^2$ denotes a linear velocity vector of the origin of frame $\{\mathbf{S_{tcp}}\}$ expressed in frame $\{\mathbf{B}\}$, and $\dot{\boldsymbol{\theta}} = [\,\dot{\theta}_2 \quad \dot{\theta}_3]^T \in \mathbb{R}^2$ denotes a simplified joint velocity vector.

In case the Cartesian velocity of the end effector is known, but the respective joint velocities are unknown, inverse velocity kinematics need to be applied. With forward velocity kinematics determined, inverse velocity kinematics can be resolved from equation (3.7) by determining its inverse. Once again the full inverse Jacobian is presented in Appendix B and only the simplified 2 DOF version is presented here.

$$\boldsymbol{J}_D^{-1} = \frac{-1}{l_1 \ \sin(\theta_3)} \begin{bmatrix} -\cos(\theta_2 + \theta_3) & -\sin(\theta_2 + \theta_3) \\ \cos(\theta_2 + \theta_3) + \cos(\theta_2) & \sin(\theta_2 + \theta_3) + \sin(\theta_2) \end{bmatrix} \tag{3.10}$$

According to [19, p. 466], the joint variables can be determined from the linear velocity

vector $\dot{\boldsymbol{p}}_{\mathbf{S_{tcp}}}$ with equation (3.10), as

$$\dot{\boldsymbol{\theta}} = \boldsymbol{J}_D^{-1}\, \dot{\boldsymbol{p}}_{\mathbf{S_{tcp}}} \tag{3.11}$$

3.2 Virtual Decomposition Control of Phantom Premium 3.0

In this section *virtual decomposition control* is applied into the Phantom Premium 3.0/ 6DOF haptic manipulator. Theory used in this section is based on [5] and essential theory is also discussed shortly beside the application of VDC into the target system.

This section is organized so that first short introduction on VDC is given. Then the manipulator under study is virtually decomposed into subsystems. Then kinematics of the Phantom Premium are presented in a form used by VDC. Following the kinematics, dynamics of the rigid links and then the joints are discussed. Finally, after the kinematic and dynamic equations have been formed, control equations are defined.

3.2.1 Short introduction on Virtual Decomposition Control

The *virtual decomposition control* differs from traditional dynamics based control methods, because instead of using complete dynamics of the manipulator to base the control equations on, dynamics of smaller subsections are considered. In this way, no matter how complicated the dynamics of the manipulator are, the dynamics of the subsections, e.g. each individual component, remain relatively simple. Further, L_2 and L_∞ stability and convergence of the entire system is maintained. This leads to an efficient way to handle control problems of systems with hyper degrees of freedom. The VDC approach is developed especially for controlling complex robotics systems. A notable advantage of VDC approach is that if one subsystem is changed or modified, only the respective local control equations, concerning that particular subsystem, are affected, while the rest of the system remains unchanged. [5, p. 9]

To prove stability within VDC, each subsystem is first shown to be virtually stable in the sense of Definition 2.11. When each subsystem is shown to be virtually stable, L_2 and L_∞ stability of the whole system follows in the sense of Lemma 2.1.

Steps describing the implementation of VDC into a robotic system can be organized as

Step 1: Virtually decompose the robot and assign coordinate system for each link, joint and object.

Step 2: Derive velocity and required velocity mappings, starting from the base and moving toward the tip

Step 3: Calculate dynamics based compensation for each link, joint and object.

Step 4: Calculate force/moment transformations, starting from the tip and moving toward the base of the manipulator.

Step 5: Ensure virtual stability on subsystem level for each subsystem. Stability of the entire system follows in view of Theorem 2.1.

In the steps shown for VDC implementation, remarkable is how the velocities are calculated starting from the base of the system and moving toward the tip of the system. Further, the forces of each subsystem are moved through the kinematic chain starting from the tip and moving toward the base of the system. This behavior comes from the recursive manner of VDC approach and is a reason for its computational efficiency. This is also visualized in Figure 3.4.

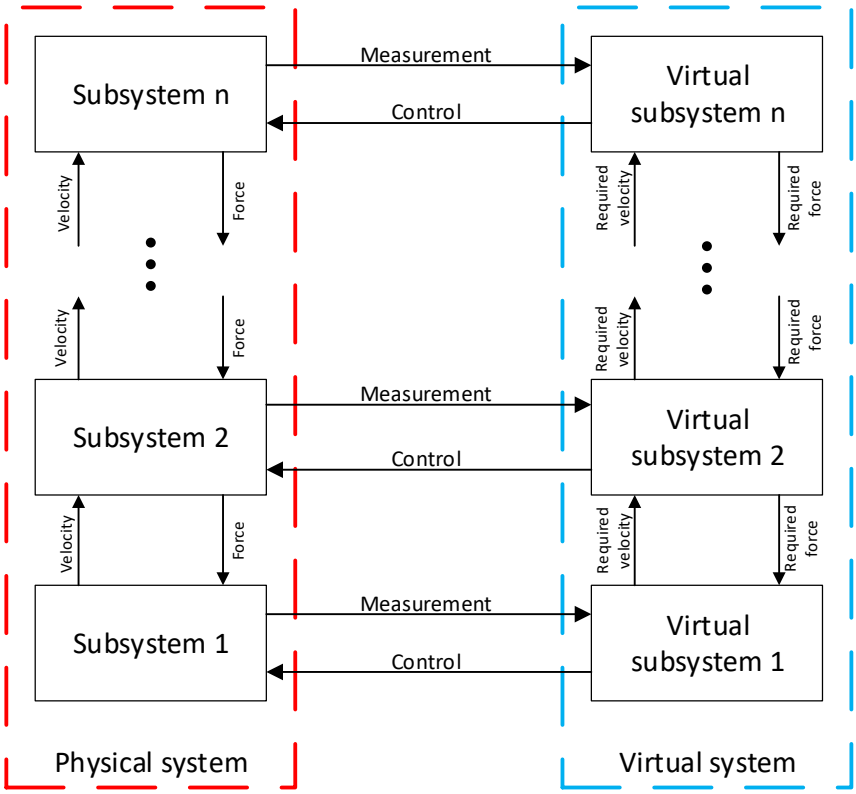

Figure 3.4 *Virtual Decomposition Control approach. [22]*

3.2.2 Virtual Decomposition of Phantom Premium

First step in VDC approach is to virtually decompose the system under study into subsystems along virtual cutting points that are placed so that there are only *open chains* and *objects* present. Within VDC approach, an *object* denotes a rigid body on which the motion and force control specifications are given [5, p. 68]. An *object* may be connected to multiple *open chains* and in addition may be in contact with the environment. An *open chain* comprises of rigid links connected by joints and has two *cutting points* located at each end. An *open chain* may be connected to two *objects* at most and it may not be in contact with the environment as opposed to *objects*.

Within the scope of this thesis, joints 1, 4, 5 and 6 of the studied manipulator are considered unactuated, leading to a case, where only two *virtual cutting points* are needed to decompose the studied manipulator into subsystems. Decomposed structure of the manipulator is presented in Figure 3.5. As can bee seen from the figure, the target system comprises of one *zero-mass object* that is rigidly grounded, one *closed chain* that needs to be decomposed into two *open chains*, and an *object* that is in contact with the environment. The *open chains* are connected to the *zero-mass object* in a common axis, and consists of four rigid links. In addition it has two motors and four unactuated rotational joints. Within the scope of this thesis, friction of the four joints are assumed to be zero.

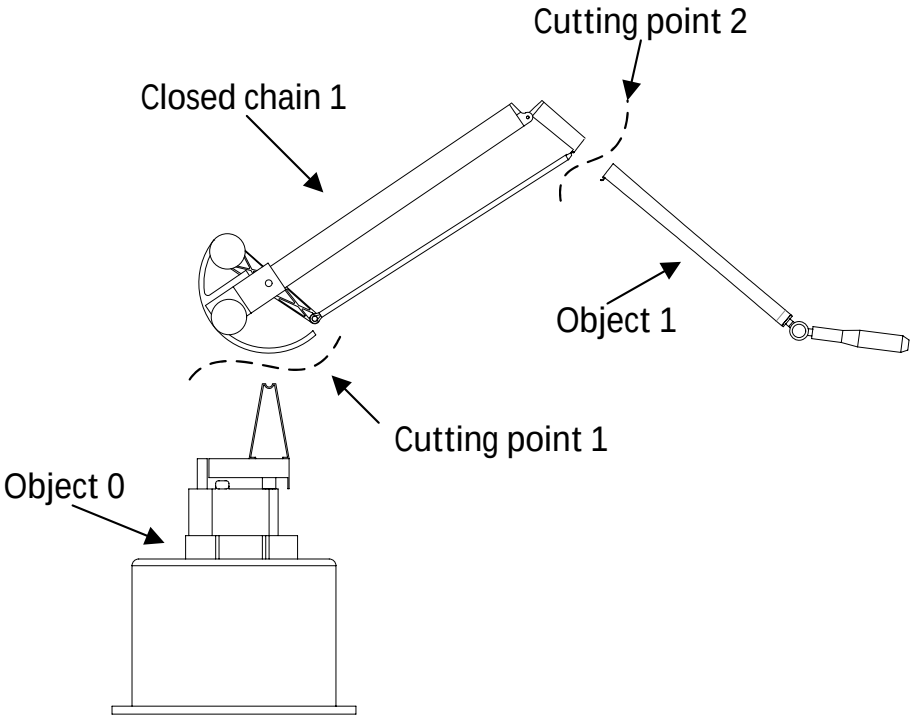

Figure 3.5 *Decomposition of Phantom Premium*

According to VDC approach, all *closed chains* need to be decomposed into *open chains*

[5, p. 64]. Thus the *closed chain* structure needs to be decomposed into two *open chain* structures as shown in Figure 3.6. The decomposition of the *closed chain* is done in a similar manner as in [15]. The base of the target system is rigid and fixed to the ground so it can be modeled as a *zero-mass object* to which no motion control specifications are applied. In view of Figure 3.5 and 3.6, a simple oriented graph of the system can be formed, which is presented in Figure 3.7.

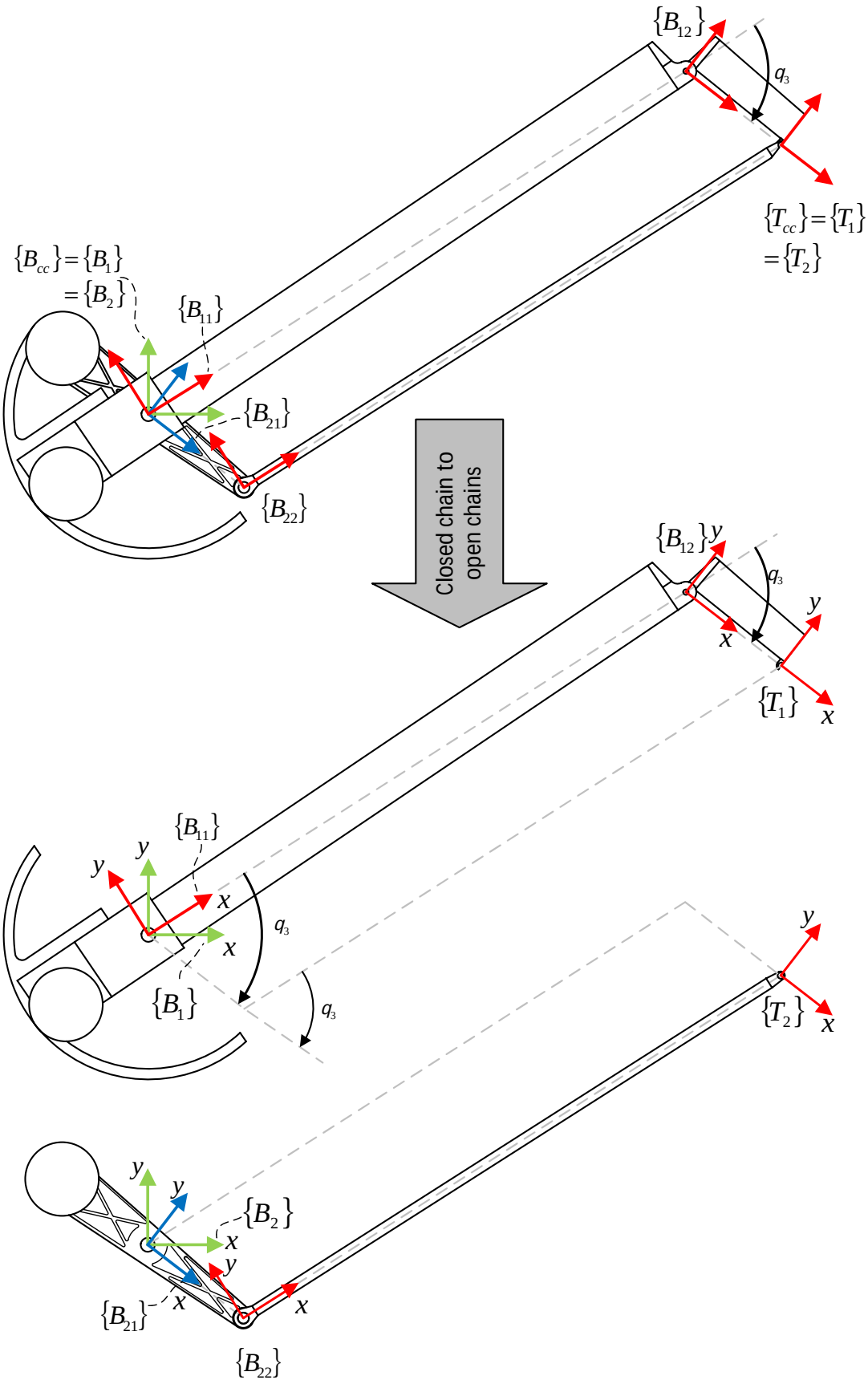

Figure 3.6 *Decomposition of closed chain 1 into two open chains*

As shown in Figure 3.3, 3.5, 3.6 and 3.7, the *virtual cutting points* of the system can be described as follows:

- The *zero-mass object* has one *driving cutting point* associated with frame $\{\mathbf{B_{cc}}\}$ and two *driven cutting points* associated with frames $\{\mathbf{B_{11}}\}$ and $\{\mathbf{B_{21}}\}$.
- The *open chain 1* has one *driving cutting point* associated with frame $\{\mathbf{B_1}\}$ and one *driven cutting point* associated with frame $\{\mathbf{T_1}\}$.
- The *open chain 2* has one *driving cutting point* associated with frame $\{\mathbf{B_2}\}$ and one *driven cutting point* associated with frame $\{\mathbf{T_2}\}$.
- The *object 1* has two *driven cutting points* associated with frames $\{\mathbf{T_1}\}$ and $\{\mathbf{T_2}\}$.

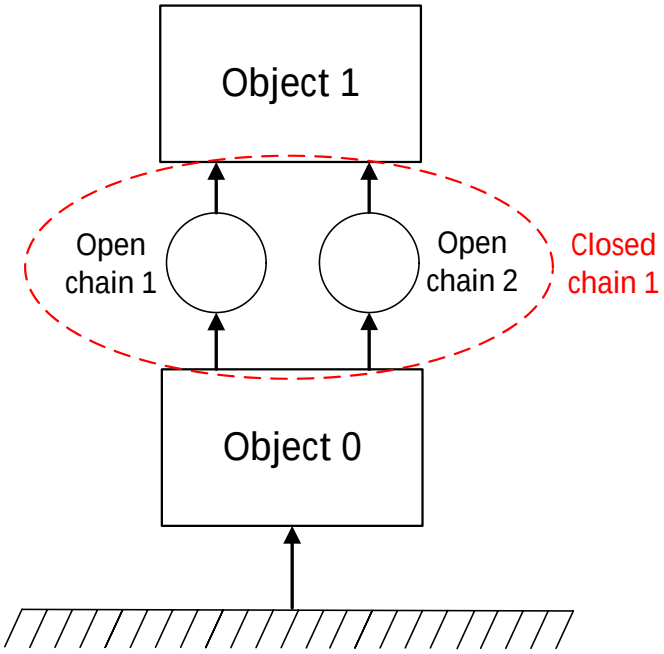

Figure 3.7 *A simple oriented graph of the Phantom Premium*

Without the simplification of the kinematic structure of the manipulator, there would need to be additional *open chain* between the *zero-mass object* and the ground for joint 1 of the manipulator and another *open chain* just after *object 2* for joints 4, 5 and 6. Furthermore, according to VDC conventions an *open chain* cannot be in contact with the environment so an additional *object* would need to be placed at the handle of the master manipulator.

3.2.3 Kinematics

In this section, essential kinematics computations and velocity transformations among different body-attached frames are given. Kinematics equations for velocity transformations are based on theory given in sections 2.3 and 2.4. Kinematics computations are calculated in an iterative manner starting from the non-moving base and computing one rigid link at a time toward the end effector.

All the frames of the system are oriented in such a manner that all the revolute joints rotate around Z-axis, while the X-axis points toward the next successive frame. This convention allows presentation of angular velocities of each joint with help of the following vector:

$$\mathbf{z}_\tau = \begin{bmatrix} 0 & 0 & 0 & 0 & 0 & 1 \end{bmatrix}^T \in \mathbb{R}^6 \tag{3.12}$$

Linear/angular velocity vector of the fixed and stationary frames $\{\mathbf{B_{cc}}\}$, $\{\mathbf{B_1}\}$ and $\{\mathbf{B_2}\}$ is known and can be written as

$${}^{\mathbf{B_{cc}}}\boldsymbol{V} = {}^{\mathbf{B_1}}\boldsymbol{V} = {}^{\mathbf{B_2}}\boldsymbol{V} = \begin{bmatrix} 0 & 0 & 0 & 0 & 0 & 0 \end{bmatrix}^T \in \mathbb{R}^6 \tag{3.13}$$

In view of (2.10) and Figure 3.6, the linear/angular velocity vectors of the open chain 1 can be computed as

$${}^{\mathbf{B_{11}}}\boldsymbol{V} = {}^{\mathbf{B_1}}\boldsymbol{U}_{\mathbf{B_{11}}}^T \, {}^{\mathbf{B_1}}\boldsymbol{V} + \mathbf{z}_\tau \dot{\boldsymbol{\theta}}_{\mathbf{2}} \tag{3.14}$$

$${}^{\mathbf{B_{12}}}\boldsymbol{V} = {}^{\mathbf{B_{11}}}\boldsymbol{U}_{\mathbf{B_{12}}}^T \, {}^{\mathbf{B_{11}}}\boldsymbol{V} + \mathbf{z}_\tau \dot{\boldsymbol{\theta}}_{\mathbf{3}} \tag{3.15}$$

$${}^{\mathbf{T_1}}\boldsymbol{V} = {}^{\mathbf{B_{12}}}\boldsymbol{U}_{\mathbf{T_1}}^T \, {}^{\mathbf{B_{12}}}\boldsymbol{V} \tag{3.16}$$

In the same manner, the linear/angular velocities of the open chain 2 can be computed as

$${}^{\mathbf{B_{21}}}\boldsymbol{V} = {}^{\mathbf{B_2}}\boldsymbol{U}_{\mathbf{B_{21}}}^T \, {}^{\mathbf{B_2}}\boldsymbol{V} + \mathbf{z}_\tau \left(\dot{\boldsymbol{\theta}}_{\mathbf{2}} + \dot{\boldsymbol{\theta}}_{\mathbf{3}} \right) \tag{3.17}$$

$${}^{\mathbf{B_{22}}}\boldsymbol{V} = {}^{\mathbf{B_{21}}}\boldsymbol{U}_{\mathbf{B_{22}}}^T \, {}^{\mathbf{B_{21}}}\boldsymbol{V} - \mathbf{z}_\tau \dot{\boldsymbol{\theta}}_{\mathbf{3}} \tag{3.18}$$

$${}^{\mathbf{T_2}}\boldsymbol{V} = {}^{\mathbf{B_{22}}}\boldsymbol{U}_{\mathbf{T_2}}^T \, {}^{\mathbf{B_{22}}}\boldsymbol{V} + \mathbf{z}_\tau \dot{\boldsymbol{\theta}}_{\mathbf{3}} \tag{3.19}$$

Finally, the linear/angular velocity of the frame $\{\mathbf{O_1}\}$ can be computed as

$${}^{\mathbf{T_{cc}}}\boldsymbol{V} = {}^{\mathbf{T_1}}\boldsymbol{V} = {}^{\mathbf{T_2}}\boldsymbol{V} \tag{3.20}$$

$$\begin{aligned} {}^{\mathbf{O_1}}\boldsymbol{V} &= {}^{\mathbf{T_{cc}}}\boldsymbol{U}_{\mathbf{O_1}}^T \, {}^{\mathbf{T_{cc}}}\boldsymbol{V} \\ &= {}^{\mathbf{S_{tcp}}}\boldsymbol{U}_{\mathbf{O_1}}^T \, {}^{\mathbf{S_{tcp}}}\boldsymbol{V} \end{aligned} \tag{3.21}$$

3.2.4 Dynamics

After kinematics equations for the linear/angular velocities of each frame are defined, the dynamics of the system and each individual rigid bodies can be considered. Dynamics equations given within this section are based on theories presented in section 2.5. Dynamics computations of the manipulator can be calculated in an iterative manner similar to the kinematics computations, but as opposed to the kinematics computations, dynamics computations are first calculated for the end effector and from there on one rigid link at a time moving toward the base of the manipulator.

This method of calculating the dynamics of the manipulator is called Newton–Euler method. Lagrangian dynamics is a more common way of calculating manipulator dynamics but much more computationally complex. Complexity of the Lagrangian method is O(n^4), whereas Newton–Euler methods complexity is O(n) [20, p. 190].

Dynamics of the *object 1* can be written according to theory presented in section 2.5 and [5, p. 73] as

$$\mathbf{M}_{\mathbf{O_1}}\frac{d}{dt}({}^{\mathbf{O_1}}\boldsymbol{V}) + \mathbf{C}_{\mathbf{O_1}}({}^{\mathbf{O_1}}\omega){}^{\mathbf{O_1}}\boldsymbol{V} + \mathbf{G}_{\mathbf{O_1}} = {}^{\mathbf{O_1}}\boldsymbol{F}^*, \tag{3.22}$$

where ${}^{\mathbf{O_1}}\boldsymbol{V} \in \mathbb{R}^6$ is obtained from (3.21). In view of [5, p. 73], the net force/moment vector of frame $\{\mathbf{O_1}\}$ is also governed by

$${}^{\mathbf{O_1}}\boldsymbol{F}^* = {}^{\mathbf{O_1}}\boldsymbol{U}_{\mathbf{T_{cc}}}\,{}^{\mathbf{T_{cc}}}\boldsymbol{F} - {}^{\mathbf{O_1}}\boldsymbol{U}_{\mathbf{S_{tcp}}}\,{}^{\mathbf{S_{tcp}}}\boldsymbol{F}, \tag{3.23}$$

where ${}^{\mathbf{S_{tcp}}}\boldsymbol{F}$ denotes the external force vector exerted by the human operator toward the handle of the manipulator. The net force resultant exerted from *object 1* to the *cutting point 2* can be derived from equations (3.22) and (3.23) as

$${}^{\mathbf{T_{cc}}}\boldsymbol{F} = {}^{\mathbf{T_{cc}}}\boldsymbol{U}_{\mathbf{O_1}}\,{}^{\mathbf{O_1}}\boldsymbol{F}^* + {}^{\mathbf{T_{cc}}}\boldsymbol{U}_{\mathbf{S_{tcp}}}\,{}^{\mathbf{S_{tcp}}}\boldsymbol{F} \tag{3.24}$$

Dynamics of the four rigid links of the *closed chain 1* can be computed in a similar manner as in (3.22) as

$$\mathbf{M}_{\mathbf{B_{12}}}\frac{d}{dt}({}^{\mathbf{B_{12}}}\boldsymbol{V}) + \mathbf{C}_{\mathbf{B_{12}}}({}^{\mathbf{B_{12}}}\omega){}^{\mathbf{B_{12}}}\boldsymbol{V} + \mathbf{G}_{\mathbf{B_{12}}} = {}^{\mathbf{B_{12}}}\boldsymbol{F}^* \tag{3.25}$$

$$\mathbf{M}_{\mathbf{B_{11}}}\frac{d}{dt}({}^{\mathbf{B_{11}}}\boldsymbol{V}) + \mathbf{C}_{\mathbf{B_{11}}}({}^{\mathbf{B_{11}}}\omega){}^{\mathbf{B_{11}}}\boldsymbol{V} + \mathbf{G}_{\mathbf{B_{11}}} = {}^{\mathbf{B_{11}}}\boldsymbol{F}^* \tag{3.26}$$

$$\mathbf{M}_{\mathbf{B_{22}}}\frac{d}{dt}({}^{\mathbf{B_{22}}}\boldsymbol{V}) + \mathbf{C}_{\mathbf{B_{22}}}({}^{\mathbf{B_{22}}}\omega){}^{\mathbf{B_{22}}}\boldsymbol{V} + \mathbf{G}_{\mathbf{B_{22}}} = {}^{\mathbf{B_{22}}}\boldsymbol{F}^* \tag{3.27}$$

$$\mathbf{M}_{\mathbf{B_{21}}}\frac{d}{dt}({}^{\mathbf{B_{21}}}\boldsymbol{V}) + \mathbf{C}_{\mathbf{B_{21}}}({}^{\mathbf{B_{21}}}\omega){}^{\mathbf{B_{21}}}\boldsymbol{V} + \mathbf{G}_{\mathbf{B_{21}}} = {}^{\mathbf{B_{21}}}\boldsymbol{F}^*, \tag{3.28}$$

where ${}^{\mathbf{B_{11}}}\boldsymbol{V}$, ${}^{\mathbf{B_{12}}}\boldsymbol{V}$, ${}^{\mathbf{B_{21}}}\boldsymbol{V}$ and ${}^{\mathbf{B_{22}}}\boldsymbol{V}$ are obtained from equations (3.14) – (3.18)

To compute resultant forces of *open chain 1* and *open chain 2*, an *internal force vector*, ${}^{\mathbf{T_{cc}}}\boldsymbol{\eta} \in \mathbb{R}^6$, and *load distribution factors* $\boldsymbol{\alpha_1}$ and $\boldsymbol{\alpha_2}$, need to be defined. The force resultant at *cutting point 2* is divided among *open chain 1* and *open chain 2* as

$$ {}^{\mathbf{T_{cc}}}\boldsymbol{F} = {}^{\mathbf{T_1}}\boldsymbol{F} + {}^{\mathbf{T_2}}\boldsymbol{F} \tag{3.29} $$

The distribution of ${}^{\mathbf{T_{cc}}}\boldsymbol{F}$ into ${}^{\mathbf{T_1}}\boldsymbol{F}$ and ${}^{\mathbf{T_2}}\boldsymbol{F}$ is governed by the load distribution factors, which are governed by geometric conditions and an internal force vector that is used to satisfy joint constraints. Joints located at frames $\{\mathbf{T_{cc}}\}$, $\{\mathbf{B_{12}}\}$ and $\{\mathbf{B_{22}}\}$ are unactuated and that constraints forces at these frames. In addition the following assumption is used to define joint constraints for all revolute joints throughout this thesis.

Assumption 1. *Frictional torques of each rotational joints of the Phantom Premium are considered zero.*

Derivation of load distribution factors and internal force vector are given in Appendix C and D, respectively, according to [23]. With internal force vector and load distribution factors defined, resultant forces of the two *open chains* can be written as

$$ {}^{\mathbf{T_1}}\boldsymbol{F} = \boldsymbol{\alpha}_{\mathbf{1}}^{\mathbf{T_{cc}}}\boldsymbol{F} + {}^{\mathbf{T_{cc}}}\boldsymbol{\eta} \tag{3.30} $$

$$ {}^{\mathbf{T_2}}\boldsymbol{F} = \boldsymbol{\alpha}_{\mathbf{2}}^{\mathbf{T_{cc}}}\boldsymbol{F} - {}^{\mathbf{T_{cc}}}\boldsymbol{\eta} \tag{3.31} $$

The resultant forces of *open chain 1* can be computed from (3.25), (3.26) and (3.30) as

$$ {}^{\mathbf{B_{12}}}\boldsymbol{F} = {}^{\mathbf{B_{12}}}\boldsymbol{F}^{*} + {}^{\mathbf{B_{12}}}\boldsymbol{U}_{\mathbf{T_1}}\,{}^{\mathbf{T_1}}\boldsymbol{F} \tag{3.32} $$

$$ {}^{\mathbf{B_{11}}}\boldsymbol{F} = {}^{\mathbf{B_{11}}}\boldsymbol{F}^{*} + {}^{\mathbf{B_{11}}}\boldsymbol{U}_{\mathbf{B_{12}}}\,{}^{\mathbf{B_{12}}}\boldsymbol{F} \tag{3.33} $$

In a similar manner, resultant forces of *open chain 2* can be computed from (3.27), (3.28) and (3.31) as

$$ {}^{\mathbf{B_{22}}}\boldsymbol{F} = {}^{\mathbf{B_{22}}}\boldsymbol{F}^{*} + {}^{\mathbf{B_{22}}}\boldsymbol{U}_{\mathbf{T_1}}\,{}^{\mathbf{T_2}}\boldsymbol{F} \tag{3.34} $$

$$ {}^{\mathbf{B_{21}}}\boldsymbol{F} = {}^{\mathbf{B_{21}}}\boldsymbol{F}^{*} + {}^{\mathbf{B_{21}}}\boldsymbol{U}_{\mathbf{B_{22}}}\,{}^{\mathbf{B_{22}}}\boldsymbol{F} \tag{3.35} $$

Motors 2 of the Phantom Premium can be used to apply torque around frame $\{\mathbf{B_{11}}\}$ that affects *open chain 1*. Similarly, motor 3 can be used to apply torque around frame $\{\mathbf{B_{21}}\}$ that affects *open chain 2* [24]. Torques affecting the motors of the Phantom Premium, induced from the external operating force and the dynamics of the manipulator can be

written as

$$\boldsymbol{\tau_{M1}} = {\mathbf{z}_\tau}^{T\,\mathbf{B_{11}}}\boldsymbol{F} \tag{3.36}$$

$$\boldsymbol{\tau_{M2}} = {\mathbf{z}_\tau}^{T\,\mathbf{B_{21}}}\boldsymbol{F} \tag{3.37}$$

3.2.5 Control Equations

Now that kinematics and dynamics equations for the Phantom Premium have been defined, the model-based control equations of the manipulator can be introduced. Control equations are first given for the required linear/angular velocity vectors of each frame, and then the required net force/moment vectors are defined.

Required velocities of the manipulator can be derived from the known θ_{2r} and θ_{3r}, which are the required values of θ_2 and θ_3, respectively. In accordance with (3.13) – (3.21), the required velocities of each frame can be defined by substituting θ_2 with θ_{2r}, and θ_3 with θ_{3r}. The required velocity of the first non moving frame $\{\mathbf{B_1}\}$ can be written as

$${}^{\mathbf{B_{cc}}}\boldsymbol{V}_r = {}^{\mathbf{B_1}}\boldsymbol{V}_r = {}^{\mathbf{B_2}}\boldsymbol{V}_r = \begin{bmatrix}0 & 0 & 0 & 0 & 0 & 0\end{bmatrix}^T \in \mathbb{R}^6 \tag{3.38}$$

Further, the required linear/angular velocity vectors of the open chain 1 can be computed as

$${}^{\mathbf{B_{11}}}\boldsymbol{V}_r = {}^{\mathbf{B_1}}\boldsymbol{U}^T_{\mathbf{B_{11}}}\,{}^{\mathbf{B_1}}\boldsymbol{V} + \mathbf{z}_\tau\dot{\boldsymbol{\theta}}_{\boldsymbol{2r}} \tag{3.39}$$

$${}^{\mathbf{B_{12}}}\boldsymbol{V}_r = {}^{\mathbf{B_{11}}}\boldsymbol{U}^T_{\mathbf{B_{12}}}\,{}^{\mathbf{B_{11}}}\boldsymbol{V} + \mathbf{z}_\tau\dot{\boldsymbol{\theta}}_{\boldsymbol{3r}} \tag{3.40}$$

$${}^{\mathbf{T_1}}\boldsymbol{V}_r = {}^{\mathbf{B_{12}}}\boldsymbol{U}^T_{\mathbf{T_1}}\,{}^{\mathbf{B_{12}}}\boldsymbol{V} \tag{3.41}$$

In the same manner, the required linear/angular velocities of the open chain 2 can be computed as

$${}^{\mathbf{B_{21}}}\boldsymbol{V}_r = {}^{\mathbf{B_2}}\boldsymbol{U}^T_{\mathbf{B_{21}}}\,{}^{\mathbf{B_2}}\boldsymbol{V} + \mathbf{z}_\tau\left(\dot{\boldsymbol{\theta}}_{\boldsymbol{2r}} + \dot{\boldsymbol{\theta}}_{\boldsymbol{3r}}\right) \tag{3.42}$$

$${}^{\mathbf{B_{22}}}\boldsymbol{V}_r = {}^{\mathbf{B_{21}}}\boldsymbol{U}^T_{\mathbf{B_{22}}}\,{}^{\mathbf{B_{21}}}\boldsymbol{V} - \mathbf{z}_\tau\dot{\boldsymbol{\theta}}_{\boldsymbol{3r}} \tag{3.43}$$

$${}^{\mathbf{T_2}}\boldsymbol{V}_r = {}^{\mathbf{B_{22}}}\boldsymbol{U}^T_{\mathbf{T_2}}\,{}^{\mathbf{B_{22}}}\boldsymbol{V} + \mathbf{z}_\tau\dot{\boldsymbol{\theta}}_{\boldsymbol{3r}} \tag{3.44}$$

Finally, the required linear/angular velocity of the frame $\{\mathbf{O_1}\}$ and $\{\mathbf{B_{tcp}}\}$ can be com-

puted as

$$
\begin{aligned}
{}^{\mathbf{T_{cc}}}\boldsymbol{V}_r &= {}^{\mathbf{T_1}}\boldsymbol{V}_r = {}^{\mathbf{T_2}}\boldsymbol{V}_r && (3.45)\\
{}^{\mathbf{O_1}}\boldsymbol{V}_r &= {}^{\mathbf{T_{cc}}}\boldsymbol{U}_{\mathbf{O_1}}^T\ {}^{\mathbf{T_{cc}}}\boldsymbol{V}_r \\
&= {}^{\mathbf{S_{tcp}}}\boldsymbol{U}_{\mathbf{O_1}}^T\ {}^{\mathbf{S_{tcp}}}\boldsymbol{V}_r && (3.46)\\
{}^{\mathbf{B_{tcp}}}\boldsymbol{V}_r &= {}^{\mathbf{T_{cc}}}\boldsymbol{U}_{\mathbf{B_{tcp}}}^T\ {}^{\mathbf{T_{cc}}}\boldsymbol{V} && (3.47)
\end{aligned}
$$

After required linear/angular velocity vectors has been designed, the required net force/-moment vectors for each rigid link and object can be created. The required net force/-moment vector comprises of the model-based feedforward term, that compensates the dynamic forces, and velocity feedback term between the measured velocity and the required velocity. The required net force/moment vector is given in [5, p. 75] as

$$
{}^{\mathbf{A}}\boldsymbol{F}_r^* = \mathbf{Y}_{\mathbf{A}}\boldsymbol{\theta}_{\mathbf{A}} + \mathbf{K}_{\mathbf{A}}\left({}^{\mathbf{A}}V_r - {}^{\mathbf{A}}V\right), \tag{3.48}
$$

where the first term on the right hand side is the model-based feedforward term, defined in (2.29), and the second term is the velocity feedback term, where $\mathbf{K_A}$ is a diagonal positive definite gain matrix. Since the scope of this thesis is constrained to a 2-DOF motion, as in [23], the regressor matrix can be simplified into $\boldsymbol{Y_{2A}} \in \mathbb{R}^{6\times 6}$ from the original $\boldsymbol{Y_A} \in \mathbb{R}^{6\times 13}$, and the parameter vector from $\boldsymbol{\theta_A} \in \mathbb{R}^{13}$ into $\boldsymbol{\theta_{2A}} \in \mathbb{R}^{6}$. The derivation of the simplified regressor matrix and parameter vector is shown in [23]. The resulting simplified regressor matrix and parameter vector are shown in Appendix A.

With equation (3.48), the net force/moment vectors of each rigid link and object can be computed as

$$
\begin{aligned}
{}^{\mathbf{O_1}}\boldsymbol{F}_r^* &= \mathbf{Y}_{\mathbf{2O_1}}\boldsymbol{\theta}_{\mathbf{2O_1}} + \mathbf{K}_{\mathbf{O_1}}\left({}^{\mathbf{O_1}}V_r - {}^{\mathbf{O_1}}V\right) && (3.49)\\
{}^{\mathbf{B_{12}}}\boldsymbol{F}_r^* &= \mathbf{Y}_{\mathbf{2B_{12}}}\boldsymbol{\theta}_{\mathbf{2B_{12}}} + \mathbf{K}_{\mathbf{B_{12}}}\left({}^{\mathbf{B_{12}}}V_r - {}^{\mathbf{B_{12}}}V\right) && (3.50)\\
{}^{\mathbf{B_{11}}}\boldsymbol{F}_r^* &= \mathbf{Y}_{\mathbf{2B_{11}}}\boldsymbol{\theta}_{\mathbf{2B_{11}}} + \mathbf{K}_{\mathbf{B_{11}}}\left({}^{\mathbf{B_{11}}}V_r - {}^{\mathbf{B_{11}}}V\right) && (3.51)\\
{}^{\mathbf{B_{22}}}\boldsymbol{F}_r^* &= \mathbf{Y}_{\mathbf{2B_{22}}}\boldsymbol{\theta}_{\mathbf{2B_{22}}} + \mathbf{K}_{\mathbf{B_{22}}}\left({}^{\mathbf{B_{22}}}V_r - {}^{\mathbf{B_{22}}}V\right) && (3.52)\\
{}^{\mathbf{B_{21}}}\boldsymbol{F}_r^* &= \mathbf{Y}_{\mathbf{2B_{21}}}\boldsymbol{\theta}_{\mathbf{2B_{21}}} + \mathbf{K}_{\mathbf{B_{21}}}\left({}^{\mathbf{B_{21}}}V_r - {}^{\mathbf{B_{21}}}V\right) && (3.53)
\end{aligned}
$$

With all the required net force/moment vectors defined, the final step for calculating the required actuating forces is to define the required force/moment vectors of each frame, calculating in opposite direction of the simple oriented graph beginning from object 1 as

$$
{}^{\mathbf{T_{cc}}}\boldsymbol{F}_r = {}^{\mathbf{T_{cc}}}\boldsymbol{U}_{\mathbf{O_1}}\ {}^{\mathbf{O_1}}\boldsymbol{F}_r^* + {}^{\mathbf{T_{cc}}}\boldsymbol{U}_{\mathbf{S_{tcp}}}\ {}^{\mathbf{S_{tcp}}}\boldsymbol{F} \tag{3.54}
$$

The distribution of forces at *closed chain 1*, shown in (3.29), can be computed by using the same internal force vector and load distribution factors as in (3.55) and (3.31).

The required force/moment vectors of *open chain* 1 can be computed as

$$^{\mathbf{T_1}}\boldsymbol{F}_r = \boldsymbol{\alpha}_{\mathbf{1}}^{\mathbf{T_{cc}}}\boldsymbol{F}_r + {}^{\mathbf{T_{cc}}}\boldsymbol{\eta} \tag{3.55}$$

$$^{\mathbf{B_{12}}}\boldsymbol{F}_r = {}^{\mathbf{B_{12}}}\boldsymbol{F}_r^{*} + {}^{\mathbf{B_{12}}}\boldsymbol{U}_{\mathbf{T_1}}\,{}^{\mathbf{T_1}}\boldsymbol{F}_r \tag{3.56}$$

$$^{\mathbf{B_{11}}}\boldsymbol{F}_r = {}^{\mathbf{B_{11}}}\boldsymbol{F}_r^{*} + {}^{\mathbf{B_{11}}}\boldsymbol{U}_{\mathbf{B_{12}}}\,{}^{\mathbf{B_{12}}}\boldsymbol{F}_r \tag{3.57}$$

Similarly the force/moment vectors of *open chain* 2 can be computed as

$$^{\mathbf{T_2}}\boldsymbol{F}_r = \boldsymbol{\alpha}_{\mathbf{2}}^{\mathbf{T_{cc}}}\boldsymbol{F}_r - {}^{\mathbf{T_{cc}}}\boldsymbol{\eta} \tag{3.58}$$

$$^{\mathbf{B_{22}}}\boldsymbol{F}_r = {}^{\mathbf{B_{22}}}\boldsymbol{F}_r^{*} + {}^{\mathbf{B_{22}}}\boldsymbol{U}_{\mathbf{T_2}}\,{}^{\mathbf{T_2}}\boldsymbol{F}_r \tag{3.59}$$

$$^{\mathbf{B_{21}}}\boldsymbol{F}_r = {}^{\mathbf{B_{21}}}\boldsymbol{F}_r^{*} + {}^{\mathbf{B_{21}}}\boldsymbol{U}_{\mathbf{B_{22}}}\,{}^{\mathbf{B_{22}}}\boldsymbol{F}_r \tag{3.60}$$

Finally, the required actuating forces of the manipulator can be obtained as

$$\boldsymbol{\tau}_{\boldsymbol{M1r}} = {\mathbf{z}_\tau}^{T}\,{}^{\mathbf{B_{11}}}\boldsymbol{F}_r \tag{3.61}$$

$$\boldsymbol{\tau}_{\boldsymbol{M2r}} = {\mathbf{z}_\tau}^{T}\,{}^{\mathbf{B_{21}}}\boldsymbol{F}_r \tag{3.62}$$

3.3 Exogenous Force Estimation of the Phantom Premium

The teleoperation scheme, presented in the next chapter, requires force measurement from the handle of the master manipulator. However the Phantom Premium 3.0 is not equipped with a force sensor. To overcome this problem, a force estimation method needs to be implemented. This section present the force estimation of the master manipulator.

Assumption 2. *Exogenous force, exerted by the operator toward the handle of the master manipulator, is compensated by the applied motor torques.*

Because the dynamics of the manipulator are known and can be calculated with equations given in subsection 3.2.4, the force estimation can be done indirectly by comparing the dynamic forces to the applied motor torques and using Assumption 2. The exogenous force input of the operator can be computed from the motor torque error as

$$^{\mathbf{S_{tcp}}}\boldsymbol{F}_m = \begin{bmatrix} \dfrac{a\cos(\theta_3) - b}{\sin(\theta_3)} \\ b \end{bmatrix}, \tag{3.63}$$

where

$$a = \frac{\boldsymbol{\tau_{M1}}}{l_1}, \tag{3.64}$$

and

$$b = \frac{\boldsymbol{\tau_{M2}}}{l_1}, \tag{3.65}$$

with $\boldsymbol{\tau_{M1}}$ and $\boldsymbol{\tau_{M2}}$, denoting the torque differences between the dynamics required and the applied torques of motor 2 and 3, respectively. Formulation of equation (3.63) is shown in Appendix E.

Figure 3.8 presents the entire control system in the master side of the teleoperation system. In addition, it presents the method of obtaining an estimate of the exogenous force input from the operator visually.

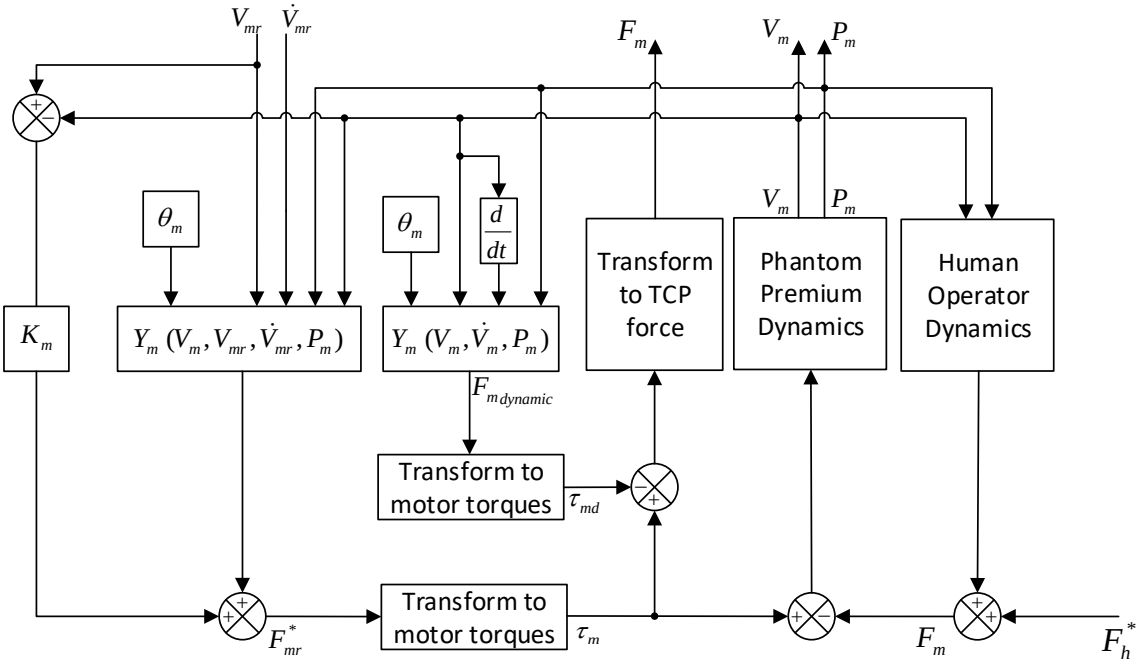

Figure 3.8 *Structure of the master manipulator control system*

4. FORCE-REFLECTED BILATERAL TELEOPERATION

In this chapter, force-reflected bilateral teleoperation is discussed, starting from short historical survey on teleoperation, and ending with description of teleoperation scheme developed by W. H. Zhu, presented first in [17] and later with more detail in [5] chapter 11. This teleoperation scheme is later in thesis applied to control HIAB 031 hydraulic manipulator with Phantom Premium 3.0/6DOF acting as a master manipulator. Notable in this setup is that electrically driven manipulator is used to control hydraulically driven manipulator.

Teleoperation is used to extend humans reach on a remote site, where direct operation is uncomfortable, impossible to reach, or hazardous for a human operator. These kind of environments may be within high levels of radiation, extraterrestrial or otherwise dangerous for human health. In addition, teleoperated systems may be used to scale human operations to micro and macro environments for accurate and non fatiguing operations.

Aim of force-reflected bilateral teleoperation is to have a teleoperation system, where the slave manipulator tracks the motion of the master manipulator and allow the human operator to feel the contact forces at the remote environment from the master manipulator [5, p. 303]. Figure 4.1 presents a typical teleoperation system that comprises of human operator, master manipulator, communication channel, slave manipulator and a remote environment.

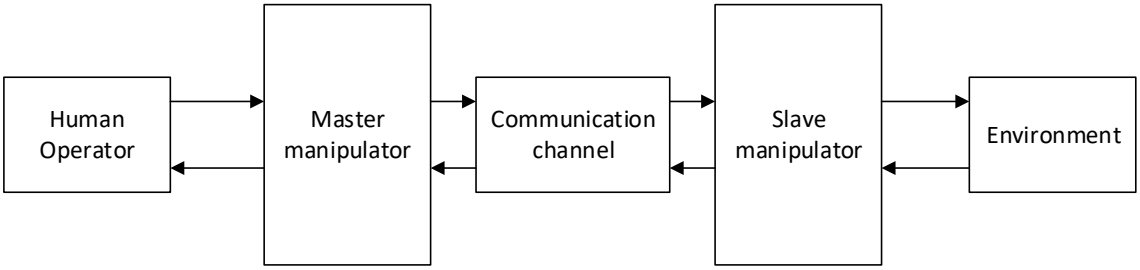

Figure 4.1 *A typical force-reflected bilateral teleoperation system*

4.1 Summary of Study Related to Teleoperation

Study on haptic teleoperation systems has started from the need to manipulate objects in environments, where humans could not operate, in the mid 1940s, when the first mechanical master-slave manipulators were built to provide safe way to handle nuclear material within a hot cell [2]. Today extensive studies concerning teleoperation has led to vast variety of applications ranging from teleoperated surgery [25], forestry applications [26,27], nuclear waste handling and hot cell decontamination [28, 29], maintenance operations in highly radioactive environment [30], to space teleoperation [31].

A comprehensive history about teleoperation and telerobotics was given in [32]. The development of teleoperation boomed in the 1950s when the first electric master slave manipulators were built, and soon the applications of teleoperation started to gain interest of researchers. In the 1960s, when space exploration and lunar flights were in development, space teleoperation was studied and the problem of time delay arose. It was found that the "move-and-wait" control slowed down even the simplest manipulation tasks notably and was simply not feasible.

Transparency of a teleoperation system has been a goal of researchers for a long time and it has been used as a performance measure of a teleoperation system. In [33], transparency was found conflicting with the stability of the system, and a four-channel control architecture was proposed. Prior to the four-channel architecture, a two-port model, as shown in Figure 4.2, was generally used to analyze bilateral teleoperation systems.

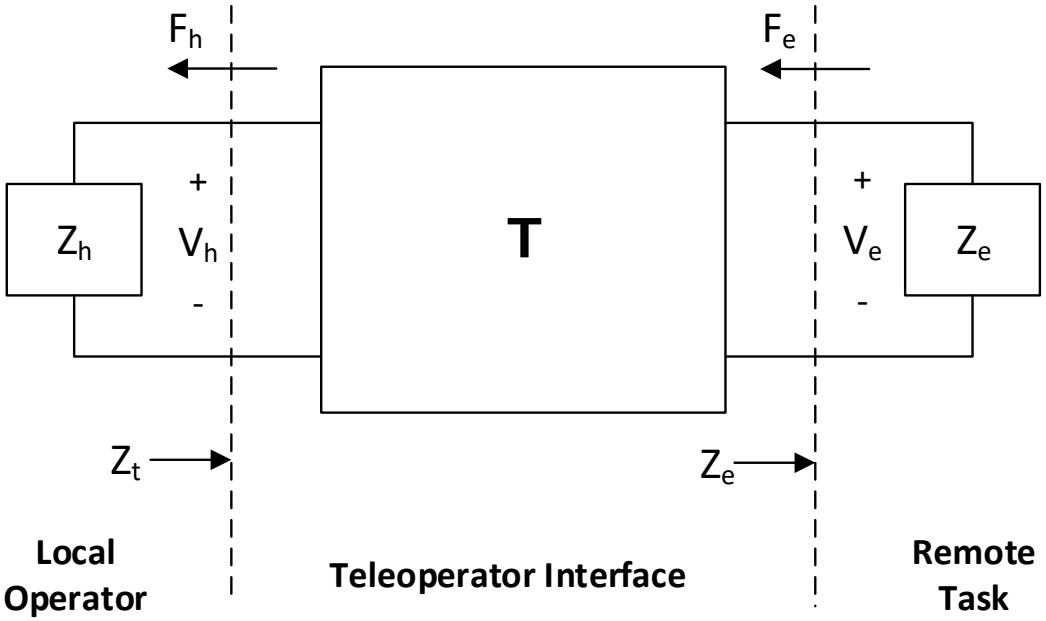

Figure 4.2 *A typical two-port model for bilateral teleoperation system [33].*

Transparency of a teleoperation system can be defined as how well the slave manipulator tracks the commands of the master manipulator, and how well the operator can feel the forces of the slave manipulator. In perfect transparency, the operator can't distinguish telemanipulation from direct manipulation [34]. When the slave is in contact with the environment, the relation between the slave manipulators velocity and force can be described with the environmental impedance as

$$\boldsymbol{F}_e = \boldsymbol{Z}_e \boldsymbol{V}_e, \tag{4.1}$$

where $\boldsymbol{F}_e$ is the force exerted from the environment toward the slave manipulator, $\boldsymbol{Z}_e$ denotes the mechanical impedance of the environment and $\boldsymbol{V}_e$ the velocity of the slave manipulator. In order for the operator to feel exactly the same forces from the master manipulator, the transmitted or "felt" impedance must match that of the environment. The impedance felt by the operator can be defined as

$$\boldsymbol{F}_h = \boldsymbol{Z}_t \boldsymbol{V}_h, \tag{4.2}$$

where $\boldsymbol{F}_h$ is the force exerted by the operator toward the master manipulator, $\boldsymbol{V}_h$ is the velocity of the master manipulator and $\boldsymbol{Z}_t$ denotes the transmitted impedance, with $\boldsymbol{Z}_t = \boldsymbol{Z}_e$ hold. [33]

Bilateral control architectures, aimed for transparent teleoperation, were presented in [35], and the four-channel architecture, presented in Figure 4.3, was extensively covered in [33], where the general four-channel architecture for a teleoperation systems was introduced. In the general four-channel architecture, local controllers for both master and slave manipulator velocities are implemented along side separate force and velocity controllers for both manipulators, connecting them to each other. The same architecture can be used for many different control structures and it has been used especially for position-position, position-force and rate-force control strategies.

Transparency performance of the above control architecture can be optimized by tuning the controllers C_s, C_m and C_1 – C_4. In position-position control architecture perfect transparency can be achieved according to [33] with the following tuning

$$\begin{cases} C_1 &= Z_s + C_s \\ C_2 &= 1 \\ C_3 &= 1 \\ C_4 &= -\left(Z_m + C_m\right). \end{cases} \tag{4.3}$$

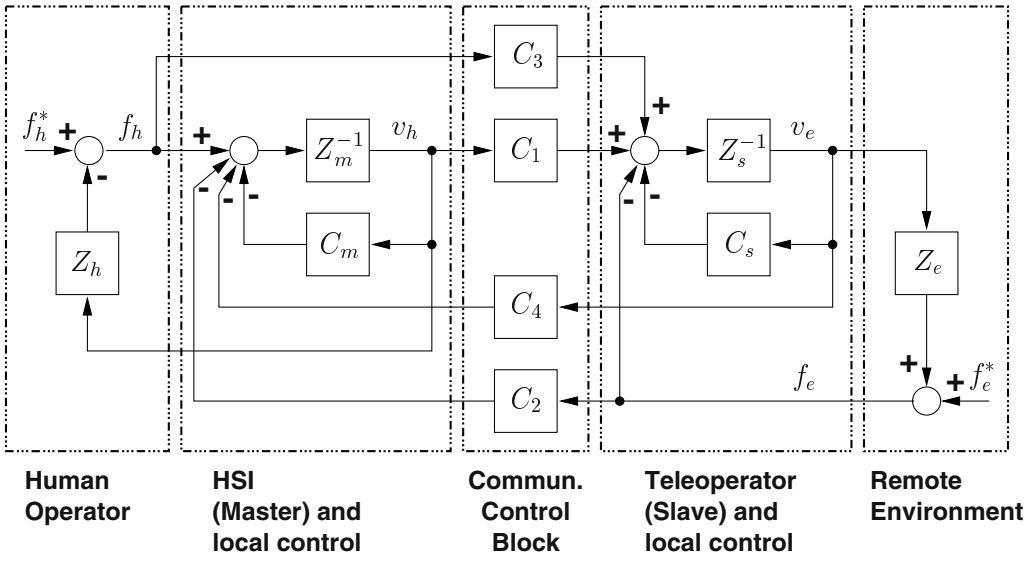

Figure 4.3 *A block diagram of a four-channel bilateral teleoperation system [35]*

Symbols in the figure 4.3 are described below:

Z_s Impedance of the slave manipulator

Z_e Impedance of the environment

Z_m Impedance of the master manipulator

Z_h Impedance of the operator's hand

C_m Local velocity controller at master manipulator's side

C_s Local velocity controller at slave manipulator's side

C_1 Master manipulator coordinating force feedforward channel

C_2 Slave manipulator coordinating velocity feedforward channel

C_3 Master manipulator coordinating velocity feedforward channel

C_4 Slave manipulator coordinating force feedforward channel

v_h Velocity of the master manipulator handle

v_e Velocity of the slave manipulator tool center point

f_h Net force of the master manipulator

f_h^* Operator exogenous force exerted toward the handle of the master manipulator

f_e Net force of the slave manipulator

f_e^* Environment exogenous force exerted toward the TCP of the slave manipulator

To address the time-delay issue of teleoperation systems, scattering operators has been used with strictly passive environment and operator in [36], to overcome instability. The proposed scheme has been proven asymptotically stable, but no convergence of force/position tracking is provided [37]. The proposed scheme was further improved by eliminating the requirement of strictly passive operator and environment by using $\mathcal{H}_\infty$ theory with μ-synthesis, in [38].

In [17], an adaptive motion/force controller for bilateral teleoperation system was presented. The proposed teleoperation scheme is L_2 and L_∞ stable in both free motion and flexible/rigid contact motion. Furthermore, it is stability guaranteed against any time-delay and perhaps most importantly, asymptotic motion tracking and force tracking is achieved in both contact motion and free motion.

4.2 Modeling the Environment and The Human Operator

In this section, the dynamical models for the environment and the human operator are discussed and given based on [5, p.305–313]. These models are used to approximate the external forces and are needed to maintain and guarantee stability.

4.2.1 The Environment

Within this thesis, environment is defined unilateral and rigid in an $n_c \geq 0$ dimensional space and flexible in an $n_f \geq 0$ dimensional space with $n_c + n_f = 6$. The environment is considered rigid if it possesses much higher mechanical impedance than the slave robot [5, p. 305]. Otherwise the environment is considered flexible. To define if the slave is in contact with a rigid/flexible environment or in free motion, two binary factors are defined as

$$\sigma_f = \begin{cases} 0 & \text{free motion} \\ 1 & \text{contact with flexible constraints} \end{cases}$$

$$\sigma_c = \begin{cases} 0 & \text{free motion} \\ 1 & \text{contact with rigid constraints.} \end{cases}$$

The contact dynamics of the manipulator need to be defined separately to both flexible and rigid environment, as shown in [5, p. 306]. For a rigid environment, contact dynamics are

governed by

$$\mathbf{v}_{sc} = (1 - \sigma_c)\, \mathbf{v}_{sc} \tag{4.4}$$

$$\mathbf{f}_{sc} = \sigma_c \mathbf{f}_{sc}, \tag{4.5}$$

where $\mathbf{f}_{sc} \in \mathbb{R}^{n_c}$ denotes rigid contact forces, and $\mathbf{v}_{sc} \in \mathbb{R}^{n_c}$ denotes velocity of the boom tip. For a flexible environment, contact dynamics are governed by

$$\sigma_f \left[\mathbf{M}_f \ddot{\mathbf{x}}_{sf} + \mathbf{D}_f \dot{\mathbf{x}}_{sf} + \mathbf{K}_f \mathbf{x}_{sf}\right] = \mathbf{f}_{sf} \tag{4.6}$$

$$\dot{\mathbf{x}}_{sf} = \sigma_f \mathbf{v}_{sf} \tag{4.7}$$

where $\mathbf{f}_{sf} \in \mathbb{R}^{n_c}$ denotes rigid contact forces, and $\mathbf{v}_{sf} \in \mathbb{R}^{n_c}$ denotes velocity of the boom tip.

In (4.6), $\mathbf{M}_f \in \mathbb{R}^{n_f \times n_f}$, $\mathbf{D}_f \in \mathbb{R}^{n_f \times n_f}$, and $\mathbf{K}_f \in \mathbb{R}^{n_f \times n_f}$ are time-invariant symmetric positive-definite matrices defining inertia, damping and stiffness of the environment, respectively, and $\boldsymbol{x}_{sf}$ denotes the deformation of the environment [5, p. 306].

4.2.2 The Human Operator

Similarly, as with the environment, the human operator is modeled with a two-order LTI model. According to [39,40], the following model is found effective for modeling human arm dynamics

$$\mathbf{M}_h \ddot{\mathbf{x}}_h + \mathbf{D}_h \dot{\mathbf{x}}_h + \mathbf{K}_h \mathbf{x}_h = \mathbf{f}_m - \mathbf{f}_h^*, \tag{4.8}$$

where $\mathbf{M}_h \in \mathbb{R}^{6\times6}$, $\mathbf{D}_h \in \mathbb{R}^{6\times6}$, and $\mathbf{K}_h \in \mathbb{R}^{6\times6}$ are symmetric positive-definite matrices defining inertia, damping and stiffness of the human operator, respectively, $\mathbf{f}_m \in \mathbb{R}^6$ denotes the reaction force/moment vector exerted from the master manipulator toward the operator, $\mathbf{x}_h$ is the position/orientation vector of the human operator's arm and $\dot{\mathbf{x}}_h$ and $\ddot{\mathbf{x}}_h$, the first and the second time-derivative of the position/orientation vector, respectively. Finally, $\mathbf{f}_h^* \in \mathbb{R}^6$ denotes the exogenous force/moment vector generated by the human operator. From a stability point of view, the exogenous force/moment vector is subject to

$$\|\mathbf{f}_h^*\|_\infty \leq \alpha_h \leq +\infty, \tag{4.9}$$

where α_h is a positive constant.

It should be noted, that the dynamics of a real human operator are much more complicated and varying between different operators, depending on the operators posture and many

other things. The dynamics equation given in (4.8) is only an approximation of the real dynamics. [5, p.310]

Within the scope of this thesis, only the Cartesian forces of the operator are considered, and the transformation of the exogenous force/moment and linear/angular velocity vectors can be written as

$$^{\mathbf{S_{tcp}}}\boldsymbol{F} = \mathbf{f}_h^* \tag{4.10}$$

$$^{\mathbf{S_{tcp}}}\boldsymbol{V} = \dot{\mathbf{x}}_h. \tag{4.11}$$

The handle of the master manipulator is connected to the rest of the manipulator with a 3-DOF unactuated wrist. Therefore, only cartesian forces are translated into the manipulator through the wrist.

4.3 Combined Control of the Master Manipulator with the Operator and the Slave Manipulator With the Environment

The control equations for both master and slave manipulator are given within this section based on [5, p.308–313]. Both the human operator and the environment have been taken into account within the control equations defined in this section.

4.3.1 Control of the Slave Manipulator

Let the desired velocity and contact force be denoted as $\mathbf{v}_{sd} = \left[\mathbf{v}_{sfd}^T\ \mathbf{v}_{scd}^T\right]^T \in \mathbb{R}^6$ and $\mathbf{f}_{sd} = \left[\mathbf{f}_{sfd}^T\ \mathbf{f}_{scd}^T\right]^T \in \mathbb{R}^6$, respectively. Further, let $\mathbf{v}_r = \left[\mathbf{v}_{sfr}^T\ \mathbf{v}_{scr}^T\right]^T \in \mathbb{R}^6$ and $\boldsymbol{f}_r = \left[\mathbf{f}_{sfr}^T\ \mathbf{f}_{scr}^T\right]^T \in \mathbb{R}^6$ be the required vectors of the firstly defined vectors with

$$\mathbf{v}_{sr} = \mathbf{v}_{sd} - \mathbf{A}\tilde{\mathbf{f}}_s \tag{4.12}$$

hold, where $\mathbf{A} = \mathrm{diag}\left(\mathbf{A}_f, \mathbf{A}_c\right) \in \mathbb{R}^{6\times6}$ is a positive definite gain matrix, and $\tilde{\mathbf{f}}_s \in \mathbb{R}^6$ denotes a filtered contact force vector [5, p. 308]. The filtered contact force vector is formed with a first order filter as

$$\dot{\tilde{\mathbf{f}}}_s + \mathbf{C}\tilde{\mathbf{f}}_s = \mathbf{C}\mathbf{f}_s, \tag{4.13}$$

where $\mathbf{C} = \mathrm{diag}\left(\mathbf{C}_f, \mathbf{C}_c\right) \in \mathbb{R}^{6\times6}$ is a diagonal positive-definite matrix defining time constants for the filter. The benefit of filtered contact force term in required velocity vector for both master and slave manipulator is the guaranteed asymptotic motion tracking between master and slave manipulators in all directions [5, p. 308]

The desired vector of the slave manipulators force is divided into two parts as $\mathbf{f}_{sd} = \left[\, \mathbf{f}_{sfd}^T \; \mathbf{f}_{scd}^T \,\right]^T \in \mathbb{R}^6$, where $\mathbf{f}_{sfd}^T \in \mathbb{R}^{nf}$ is associated with the flexible environment, and $\mathbf{f}_{scd}^T \in \mathbb{R}^{nc}$ is associated with the constrained environment. The desired dynamics equations for flexible and rigid environment are designed according to [5, p. 307–308] as

$$\mathbf{f}_{sfd} = \sigma_f \left[\mathbf{M}_f \ddot{\boldsymbol{x}}_{sf} + \mathbf{D}_f \dot{\boldsymbol{x}}_{sf} + \mathbf{K}_f \boldsymbol{x}_{sf}\right] \tag{4.14}$$

$$\mathbf{f}_{scd} = \sigma_c \mathbf{A}_c^{-1} (\mathbf{C}_c^{-1} \dot{\mathbf{v}}_{scd} + \mathbf{v}_{scd}) \tag{4.15}$$

The required force/moment and linear/angular velocity vectors at the tool center point frame $\{\mathbf{S_s}\}$ can be written according to [5, p. 309] as

$${}^{\mathbf{S}_s}\boldsymbol{F}_r = \mathbf{T}_s^{-T} \left[\mathbf{S}_f \; \mathbf{S}_c\right] \begin{bmatrix} \sigma_f \boldsymbol{f}_{sfd} \\ \sigma_c \boldsymbol{f}_{scd} \end{bmatrix} \tag{4.16}$$

$${}^{\mathbf{S}_s}\boldsymbol{V}_r = \mathbf{T}_s \left[\mathbf{S}_f \; \mathbf{S}_c\right] \begin{bmatrix} \boldsymbol{v}_{sfr} \\ \boldsymbol{v}_{scr} \end{bmatrix}, \tag{4.17}$$

where $\mathbf{T}_s \in \mathbb{R}^{6\times 6}$ is an invertible transformation matrix translating the contact forces and velocities $\boldsymbol{f}_s$ and $\boldsymbol{v}_s$ to ${}^{\mathbf{S}_s}\boldsymbol{F}$ and ${}^{\mathbf{S}_s}\boldsymbol{V}$, respectively, and $\mathbf{S}_f \in \mathbb{R}^{6\times n_f}$ and $\mathbf{S}_c \in \mathbb{R}^{6\times n_c}$ contain unit orthogonal vectors that span the flexible and rigid contact subspace, respectively.

Let frame $\{\mathbf{O_s}\}$ be attached to the last object of the slave manipulator, and frame $\{\mathbf{T_{cc2}}\}$ be located at the *cutting point* between the last object and the previous *open/closed chain*. It follows that the required net force/moment and the linear/angular velocity vectors of the last object can be defined as

$${}^{\mathbf{O}_s}\boldsymbol{F}_r^* = {}^{\mathbf{O_s}}\boldsymbol{U}_{\mathbf{T_{cc2}}} \, {}^{\mathbf{T_{cc2}}}\boldsymbol{F}_r - {}^{\mathbf{O_s}}\boldsymbol{U}_{\mathbf{S_s}} \, {}^{\mathbf{S_s}}\boldsymbol{F}_r \tag{4.18}$$

$${}^{\mathbf{O}_s}\boldsymbol{V}_r = {}^{\mathbf{T_{cc2}}}\boldsymbol{U}_{\mathbf{O_s}}^T \, {}^{\mathbf{T_{cc2}}}\boldsymbol{V}_r = {}^{\mathbf{S_s}}\boldsymbol{U}_{\mathbf{O_s}}^T \, {}^{\mathbf{S_s}}\boldsymbol{V}_r, \tag{4.19}$$

where ${}^{\mathbf{O}_s}\boldsymbol{F}_r^* \in \mathbb{R}^6$ can be obtained similarly as in (3.48).

Virtual stability of the last object of the slave manipulator, with and without contact to the environment, combined with its respective control equations, is shown in [5, p. 309]. Virtual stability of the slave manipulator further leads to

$$\left(\mathbf{v}_{sd} - \mathbf{v}_s - \mathbf{A}\tilde{\mathbf{f}}_{sd}\right) \in L_2 \bigcap L_\infty. \tag{4.20}$$

Equation (4.20) can be further rewritten into

$$\boldsymbol{\rho}_s \overset{def}{=} \mathbf{v}_{sd} - \mathbf{v}_s - \mathbf{A}\tilde{\mathbf{f}}_{sd} \in L_2 \bigcap L_\infty, \tag{4.21}$$

to describe the motion control error of the slave manipulator.

4.3.2 Control of the Master Manipulator

Control of the master manipulator follows largely the same way shown in previous subsection concerning the slave manipulator. Again, desired vectors for the force/moment and linear/angular velocity of the master manipulator handle are formed as $\mathbf{f}_{md} \in \mathbb{R}^6$ and $\mathbf{v}_{md} \in \mathbb{R}^6$, respectively. Further, let $\mathbf{v}_{mr} \in \mathbb{R}^6$ and $\boldsymbol{f}_{mr} \in \mathbb{R}^6$ be the required vectors of $\mathbf{v}_m$ and $\mathbf{f}_m$, respectively, with

$$\mathbf{v}_{mr} = \mathbf{v}_{md} - \mathbf{A}\tilde{\mathbf{f}}_m \tag{4.22}$$

hold, where $\tilde{\mathbf{f}}_m \in \mathbb{R}^6$ denotes a filtered contact force vector, formed similarly as in (4.13).

Desired contact force of the master manipulator is designed, using both the estimated operator dynamics and a velocity feedback term as

$$\mathbf{f}_{md} = \mathbf{M}_h\dot{\mathbf{v}}_{mr} + \mathbf{D}_h\dot{\mathbf{x}}_h + \mathbf{K}_h\mathbf{x}_h + \alpha_h \text{sign}(\mathbf{v}_{mr} - \mathbf{v}_m). \tag{4.23}$$

Further, the required vectors of ${}^{\mathbf{S_{tcp}}}\boldsymbol{F}$ and ${}^{\mathbf{S_{tcp}}}\boldsymbol{V}$ can be defined as

$${}^{\mathbf{S_{tcp}}}\boldsymbol{F}_r = \mathbf{f}_{md} \tag{4.24}$$

$${}^{\mathbf{S_{tcp}}}\boldsymbol{V}_r = \mathbf{v}_{mr}. \tag{4.25}$$

Let frame $\{\mathbf{T_{cc}}\}$ be attached to the *cutting point* that separates the handle from the last *open/closed chain*, and frame $\{\mathbf{O_m}\}$ be attached to the handle of the master manipulator. Finally, the motion and force control specifications for the last object of the master manipulator can be written as

$${}^{\mathbf{O_m}}\boldsymbol{F}_r^* = {}^{\mathbf{O_m}}\boldsymbol{U}_{\mathbf{T_{cc}}}\,{}^{\mathbf{T_{cc}}}\boldsymbol{F}_r - {}^{\mathbf{O_m}}\boldsymbol{U}_{\mathbf{S_{tcp}}}\,{}^{\mathbf{S_{tcp}}}\boldsymbol{F}_r \tag{4.26}$$

$${}^{\mathbf{O_m}}\boldsymbol{V}_r = {}^{\mathbf{O_m}}\boldsymbol{U}^T_{\mathbf{T_{cc}}}\,{}^{\mathbf{T_{cc}}}\boldsymbol{V}_r - {}^{\mathbf{O_m}}\boldsymbol{U}^T_{\mathbf{S_{tcp}}}\,{}^{\mathbf{S_{tcp}}}\boldsymbol{V}_r, \tag{4.27}$$

Virtual stability of the master manipulator with the human operator, combined with its respective control equations, is shown in [5, p. 313]. It is also shown that virtual stability of the master manipulator leads to

$$\left(\mathbf{v}_{md} - \mathbf{v}_m - \mathbf{A}\tilde{\mathbf{f}}_{md}\right) \in L_2 \bigcap L_\infty. \tag{4.28}$$

Equation (4.28) can be further rewritten into

$$\boldsymbol{\rho}_m \overset{def}{=} \mathbf{v}_{md} - \mathbf{v}_m - \mathbf{A}\tilde{\mathbf{f}}_{md} \in L_2 \bigcap L_\infty, \tag{4.29}$$

to describe the motion control error of the master manipulator.

4.4 Adaptive Bilateral Teleoperation

After independent controls for both master and slave manipulators have been designed, the communication block, transferring velocity and force commands between the master ans slave manipulator bilaterally, can be designed. The aim of the communication block is to transfer commands between manipulator in low latency, and in a manner that provides transparent motion and force tracking for each manipulator. This section presents the structure of the communication block starting from the control structure, then briefly discussing the stability aspects and finally defining transparency.

4.4.1 Control Design

Control equations for bilateral position-force teleoperation system are given according to [5, p. 314]. To ensure usability with different kind of manipulators and operating forces, position and force scaling gains are implemented as $\boldsymbol{\kappa_f}$ and $\boldsymbol{\kappa_p}$ being the force scaling and the position scaling, respectively. Design vectors for the master and slave manipulator velocities are then designed based on (4.21) and (4.29) as

$$\mathbf{v}_{sd} = \boldsymbol{\kappa}_p(\tilde{\mathbf{v}}_m + \boldsymbol{\Lambda}\tilde{\mathbf{p}}_m) - \boldsymbol{\Lambda}\mathbf{p}_s - \mathbf{A}\kappa_f\tilde{\mathbf{f}}_m \tag{4.30}$$

$$\mathbf{v}_{md} = \boldsymbol{\kappa}_p^{-1}\left\{\tilde{\mathbf{v}}_s + \boldsymbol{\Lambda}\tilde{\mathbf{p}}_s - \boldsymbol{\kappa}_p\boldsymbol{\Lambda}\mathbf{p}_m - \mathbf{A}\left[\tilde{\mathbf{f}}_s + (\boldsymbol{\kappa}_f - \boldsymbol{\kappa}_p)\,\tilde{\mathbf{f}}_m\right]\right\}, \tag{4.31}$$

where $\Lambda \in \mathbb{R}^{6\times 6}$ is a diagonal positive-definite matrix, and $\mathbf{p}_m$ and $\mathbf{p}_s$ denote the position/orientation of the master and slave manipulator, respectively, subject to $\dot{\mathbf{p}}_m = \mathbf{v}_m$ and $\dot{\mathbf{p}}_s = \mathbf{v}_s$. A tilde on top of any of the four state vectors, $\mathbf{v}_m$, $\mathbf{v}_s$, $\mathbf{p}_m$ and $\mathbf{p}_s$, denotes a filtered vector, obtained in a similar manner as in (4.13).

Finally, two equations are formed to characterize the transparency of the entire teleoperation system and ensure asymptotic motion tracking between the master and slave manipulators. Substitute (4.30) and (4.31) into (4.21) and (4.29) using $\dot{\mathbf{p}}_m = \mathbf{v}_m$ and $\dot{\mathbf{p}}_s = \mathbf{v}_s$.

Then, summation and subtraction yields

$$\begin{aligned}\boldsymbol{\rho}_s - \boldsymbol{\kappa}_p\boldsymbol{\rho}_m &= \boldsymbol{\kappa}_p\tilde{\mathbf{v}}_m - \tilde{\mathbf{v}}_s + \boldsymbol{\Lambda}\left[\boldsymbol{\kappa}_p\tilde{\mathbf{p}}_m - \tilde{\mathbf{p}}_s\right] \\ &\quad + \boldsymbol{\kappa}_p\mathbf{v}_m - \mathbf{v}_s + \boldsymbol{\Lambda}\left[\boldsymbol{\kappa}_p\mathbf{p}_m - \mathbf{p}_s\right] \end{aligned} \tag{4.32}$$

$$\begin{aligned}\boldsymbol{\rho}_s + \boldsymbol{\kappa}_p\boldsymbol{\rho}_m &= \boldsymbol{\kappa}_p\left(\tilde{\mathbf{v}}_m - \mathbf{v}_m\right) + \tilde{\mathbf{v}}_s - \mathbf{v}_s \\ &\quad + \boldsymbol{\Lambda}\boldsymbol{\kappa}_p\left(\tilde{\mathbf{p}}_m - \mathbf{p}_m\right) + \boldsymbol{\Lambda}\left(\tilde{\mathbf{p}}_s - \mathbf{p}_s\right) - 2\boldsymbol{A}\left(\tilde{\mathbf{f}}_s + \boldsymbol{\kappa}_f\tilde{\mathbf{f}}_m\right) \\ &= -\boldsymbol{C}^{-1}\left(\boldsymbol{\kappa}_p\dot{\tilde{\mathbf{v}}}_m + \dot{\tilde{\mathbf{v}}}_s + \boldsymbol{\Lambda}\left(\boldsymbol{\kappa}_p\tilde{\mathbf{v}}_m + \tilde{\mathbf{v}}_s\right)\right) \\ &\quad - 2\boldsymbol{A}\left(\tilde{\mathbf{f}}_s + \boldsymbol{\kappa}_f\tilde{\mathbf{f}}_m\right)\end{aligned} \tag{4.33}$$

4.4.2 Stability

L_2 and L_∞ stability of the master and slave motion tracking can be proven according to [5, p. 315] by first re-writing (4.32) as

$$\tilde{\mathbf{e}} + \mathbf{e} = \boldsymbol{\rho}_s - \boldsymbol{\kappa}_p\boldsymbol{\rho}_m, \tag{4.34}$$

where

$$\mathbf{e} \overset{def}{=} \boldsymbol{\kappa}_p\mathbf{v}_m - \mathbf{v}_s + \boldsymbol{\Lambda}(\boldsymbol{\kappa}_p\mathbf{p}_m - \mathbf{p}_s), \tag{4.35}$$

subject to

$$\dot{\tilde{\mathbf{e}}} + \mathbf{C}\tilde{\mathbf{e}} = \mathbf{C}\mathbf{e}, \tag{4.36}$$

where C denotes a diagonal positive-definite matrix.

In [5, p. 20], Lemma 2.6, it has been proven that if $\mathbf{e} \in L_2 \bigcap L_\infty$, then $\tilde{\mathbf{e}} \in L_2 \bigcap L_\infty$ and $\dot{\tilde{\mathbf{e}}} \in L_2 \bigcap L_\infty$. Substituting (4.36) into (4.34) yields

$$\mathbf{e} \in L_2 \bigcap L_\infty \tag{4.37}$$

Position and force tracking of master and slave manipulator can then be shown to be L_2 and L_∞ stable using results from (4.35), (4.37) and Lemma 2.6 in [5]. It follows that

$$\boldsymbol{\rho}_p \overset{def}{=} \boldsymbol{\kappa}_p\mathbf{p}_m - \mathbf{p}_s \in L_2 \bigcap L_\infty \tag{4.38}$$

$$\boldsymbol{\rho}_v \overset{def}{=} \boldsymbol{\kappa}_p\mathbf{v}_m - \mathbf{v}_s \in L_2 \bigcap L_\infty \tag{4.39}$$

hold in both flexible and rigid environment.

The stability of the entire teleoperation system can be proven by showing that the velocities of both manipulators remain bounded for bounded exogenous forces/moments, $\mathbf{f}_h^* \in \mathbb{R}^6$, exerted by the operator toward the handle of the master manipulator. In [5, p. 316–317], this is shown for four different operating cases; first when slave manipulator is in free motion, then in contact with a flexible environment, after that contact with a rigid environment, and lastly when the slave manipulator is in contact with both rigid and flexible environments at the same time. In all these four cases it is shown that velocities of both master and slave manipulator remain bounded for bounded exogenous forces/moments.

Last part of stability analysis of the teleoperation system is to show asymptotic stability for motion control of the teleoperation system. To ensure asymptotic stability, the common algebraic loop issue of force control strategies need to be addressed first. Conditions, to ensure stability of the algebraic loop issue, are shown in [5, p. 317]. When the algebraic loop stability has been ensured, it follows that both $\boldsymbol{\rho}_m$ and $\boldsymbol{\rho}_s$ defined by (4.29) and (4.21), respectively, are uniformly continuous functions in both L_2 and L_∞ spaces [5, p. 320]. This further leads to

$$\boldsymbol{\rho}_m \to \mathbf{0} \tag{4.40}$$

$$\boldsymbol{\rho}_s \to \mathbf{0} \tag{4.41}$$

using Lemma 2.8, given in [41]. From the asymptotic stability of the master and slave manipulator, it inevitably follows that

$$\boldsymbol{\rho}_p = \boldsymbol{\kappa}_p \mathbf{p}_m - \mathbf{p}_s \to \mathbf{0} \tag{4.42}$$

$$\boldsymbol{\rho}_v = \boldsymbol{\kappa}_p \mathbf{v}_m - \mathbf{v}_s \to \mathbf{0} \tag{4.43}$$

hold, and thus ensure asymptotic position control in position-force control mode. It should be noted that this result holds for both the free motion and the contact motion with a rigid/flexible environment. According to Zhu, this result is not common with other teleoperation control approaches, where asymptotic position tracking can be ensured usually only for free motion. [5, p. 320]

4.4.3 Transparency

Transparency of the teleoperation system is governed by equation 4.33. To analyze the transparency, re-write (4.33) as

$$-\tilde{\mathbf{f}}_m = \boldsymbol{\kappa}_f^{-1}\tilde{\mathbf{f}}_s + \boldsymbol{\kappa}_f^{-1}\boldsymbol{\kappa}_p \mathbf{A}^{-1}\mathbf{C}^{-1}(s\mathbf{I} + \boldsymbol{\Lambda})\tilde{\mathbf{v}}_m + \frac{1}{2}\boldsymbol{\kappa}_f^{-1}\boldsymbol{\rho}. \tag{4.44}$$

Within certain, low enough frequency range, bounded by the filtering coefficient $\mathbf{C}$, the filtering doesn't affect the transparency of the system. In addition, $\boldsymbol{\rho} \to 0$ holds, in view of stability analysis shown in previous subsection. Equation (4.44) comprises of three separate parts. It should be noted that the term on the left hand site denotes exogenous force from the operator toward the handle of the master manipulator. The first term on the right hand side denotes contribution of the operator force to the task execution. The second term on the right hand side characterizes the teleoperation system as a free-floating mass with a linear damper. Last term on the right hand side denotes the motion tracking error.

Transparency of the system can be increased by choosing large control parameters $\mathbf{A}$ and $\mathbf{C}$. However they cannot be too large to avoid algebraic loop caused by the force control and further discussed in [5, p. 317].

4.5 Remarks

The teleoperation defined in this chapter is in many ways more sophisticated than conventional teleoperation systems.

1. Asymptotic motion tracking between master and slave manipulator is guaranteed in both free motion and contact motion.
2. Arbitrary motion/force scaling to interact with both micro and macro environments and in addition allow that the manipulator workspaces between slave and master can differ notably.
3. Non-linear model-based dynamics of both master and slave manipulator are taken into account in control.
4. Slave robot can be operated in free space, rigid environment and flexible environment
5. The entire teleoperation system behaves as a mass and a damper specified solely by the control parameters $\mathbf{A}$, $\mathbf{C}$, $\boldsymbol{\Lambda}$, $\boldsymbol{\kappa}_p$ and $\boldsymbol{\kappa}_f$.

Further, although not shown within the scope of this thesis, the teleoperation system is stability guaranteed against any time-delay and if implemented can handle parametric uncertainties by independent fast parameter adaption algorithm. [5, p. 304]

5. EXPERIMENTAL FORCE-REFLECTED BILATERAL TELEOPERATION SYSTEM

In this chapter, experimental force-reflected bilateral teleoperation system implementation is introduced and results are discussed. The experimental system is formed as a natural continuum of the work previously discussed within this thesis. The experimental implementation and testing, along with all the measurements shown in this chapter, were carried out in the heavy machinery laboratory of department of Automation and Hydraulics (AUT), in Tampere University of Technology (TUT).

This chapter is divided into two main parts. First the experimental system implementation is defined. The experimental implementation can be further divided to the master manipulator, the slave manipulator and the real time computer, where real time control is performed. After the experimental implementation is introduced, the results of the experiment are discussed.

5.1 Experimental Implementation

The experimental setup comprises of four main components; Phantom Premium 3.0L 6-DOF as a master manipulator, host computer for the master manipulator, HIAB 031 as a slave manipulator and dSpace real-time computer running independent VDC models for both master and slave manipulator. The communication between the dSpace and the host computer for the master manipulator is implemented via UDP protocol. Figure 5.1 illustrates this experimental system in a very high level.

5.1.1 Phantom Premium

Virtual decomposition control for the master manipulator, defined in Chapter 3, is used to control the master manipulator. Desired velocity of the master manipulator is obtained using the teleoperation scheme defined in Chapter 4. Parameter identification for parameter vector $\boldsymbol{\theta_{2A}} \in \mathbb{R}^6$ for each rigid body has been done by modeling the manipulator first in SolidWorks 3D CAD program. All unknown parameters for each rigid body were calculated separately and verified by using the VDC to cancel the dynamics of the manipulator

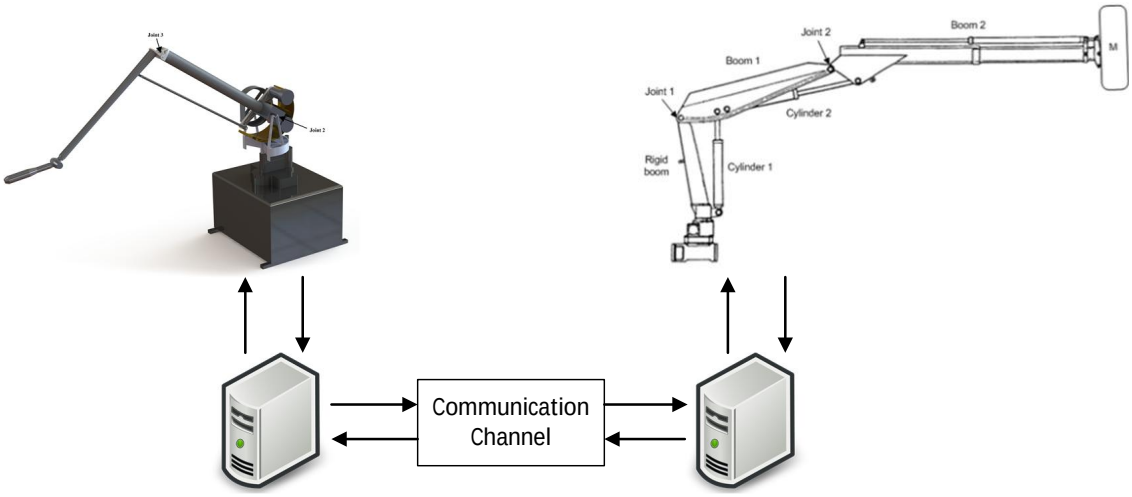

Figure 5.1 *High level overview of the experimental implementation*

within the whole workspace. Obtained values for each parameter vector are presented below in table 5.1. How these parameters are used to form the parameter vector $\boldsymbol{\theta_{2A}}$ is shown in Appendix A.

Table 5.1 *Rigid body parameters*

Rigid body	Body frame	$m_{\mathbf{A}}$ [g]	${}^{\mathbf{A}}r_{mx}$ [mm]	${}^{\mathbf{A}}r_{my}$ [mm]	$I_{\mathbf{A}zz}$ [kgm^2]
Link$_{11}$	$\{\mathbf{B_{11}}\}$	3900	-57.0	-4.69	27.43×10^{-3}
Link$_{12}$	$\{\mathbf{B_{12}}\}$	28.7	27.7	15.1	0.026×10^{-3}
Link$_{21}$	$\{\mathbf{B_{21}}\}$	377	-71.3	0	0.368×10^{-3}
Link$_{22}$	$\{\mathbf{B_{22}}\}$	26.8	221	0	0.518×10^{-3}
Object$_1$	$\{\mathbf{T_{cc}}\}$	410	400	2.14	4.144×10^{-3}

In table 5.1, $m_{\mathbf{A}}$ denotes the mass of the rigid body, ${}^{\mathbf{A}}r_{mx}$ and ${}^{\mathbf{A}}r_{my}$ the x and y coordinate of the center of mass with respect to the appropriate body frame, respectively, and $I_{\mathbf{A}zz}$ the moment of inertia of the rigid body around Z-axis, measured from the center of mass. It should be noted that the rigid body parameters for the last object are given in frame $\{\mathbf{T_{cc}}\}$ instead of $\{\mathbf{O_1}\}$. Motion and force control equations for *object 1* need to be adjusted from (3.24) into

$$ {}^{\mathbf{T_{cc}}}\boldsymbol{F}_r = {}^{\mathbf{T_{cc}}}\boldsymbol{F}_r^* + {}^{\mathbf{T_{cc}}}\boldsymbol{U}_{\mathbf{S_{tcp}}}\, {}^{\mathbf{S_{tcp}}}\boldsymbol{F}, \tag{5.1} $$

where

$$ {}^{\mathbf{T_{cc}}}\boldsymbol{F}_r^* = \mathbf{Y}_{\mathbf{2T_{cc}}}\boldsymbol{\theta}_{\mathbf{2T_{cc}}} + \mathbf{K}_{\mathbf{T_{cc}}}\left({}^{\mathbf{T_{cc}}}V_r - {}^{\mathbf{T_{cc}}}V\right). \tag{5.2} $$

On a more physical level the Phantom Premium haptic manipulator was connected to a Linux computer running Ubuntu 14.1. The system was running on multi user mode, but system services and other unnecessary functionality was disabled to improve deterministic behavior of the system. The host computer of the master manipulator was not used for any VDC related calculation, but was solely use as a communication medium to transfer joint angles and button state from the Phantom Premium to the dSpace running the VDC algorithms and sending torque commands from the dSpace to the current amplifiers of the Phantom Premium. The communication between the host computer and the dSpace was done using UDP protocol.

Communication with the haptic manipulator was done using Phantom Device Drivers and OpenHaptics API. The OpenHaptics API allowed direct torque control of the manipulators arms. Further, it is used to measure joint angles of the manipulator and sense the state of the pushbutton at the handle of the manipulator. [24]

5.1.2 Hiab 031

HIAB 031 Hydraulic manipulator was chosen to act as the slave manipulator, within the experimental implementation. Figure 5.2 presents the chosen manipulator in it's laboratory implementation. Within the experiments, only two cylinders, controlling the booms of the HIAB are actuated. Rotation and extension are both unactuated and considered rigid.

On hardware side, the HIAB is equipped with Heidenhain ROD 456 incremental encoder (5000 inc/rev) with IVB interpolation units for joints 1 and 2, providing a theoretical piston position resolution < 1.2×10^{-3} mm. In place of the original valves, Bosch Rexroth servo solenoid valves (Type: 4WRPEH10) with control bandwidth of 100 Hz at $\pm 5\%$ signals. For the first cylinder, controlling the lift of the boom, the nominal flow of the valve was 100 dm^3 at 3.5 MPa per notch, while for the second cylinder, controlling the tilt of the boom, the nominal flow of the valve was 50 dm^3 at 3.5 MPa per notch. All system pressures used for modeling hydraulic fluid dynamics and valve dynamics as well as cylinder actuating forces, were measured using Trafag NAH hydraulic pressure transmitters. Measurement range of the pressure sensors were 25 MPa, and they had pressure resolution of 0.025 MPa. Lastly, the slave manipulator was equipped with a 475 kg payload at the end of the manipulator, denoted as M in Figure 5.3(a).

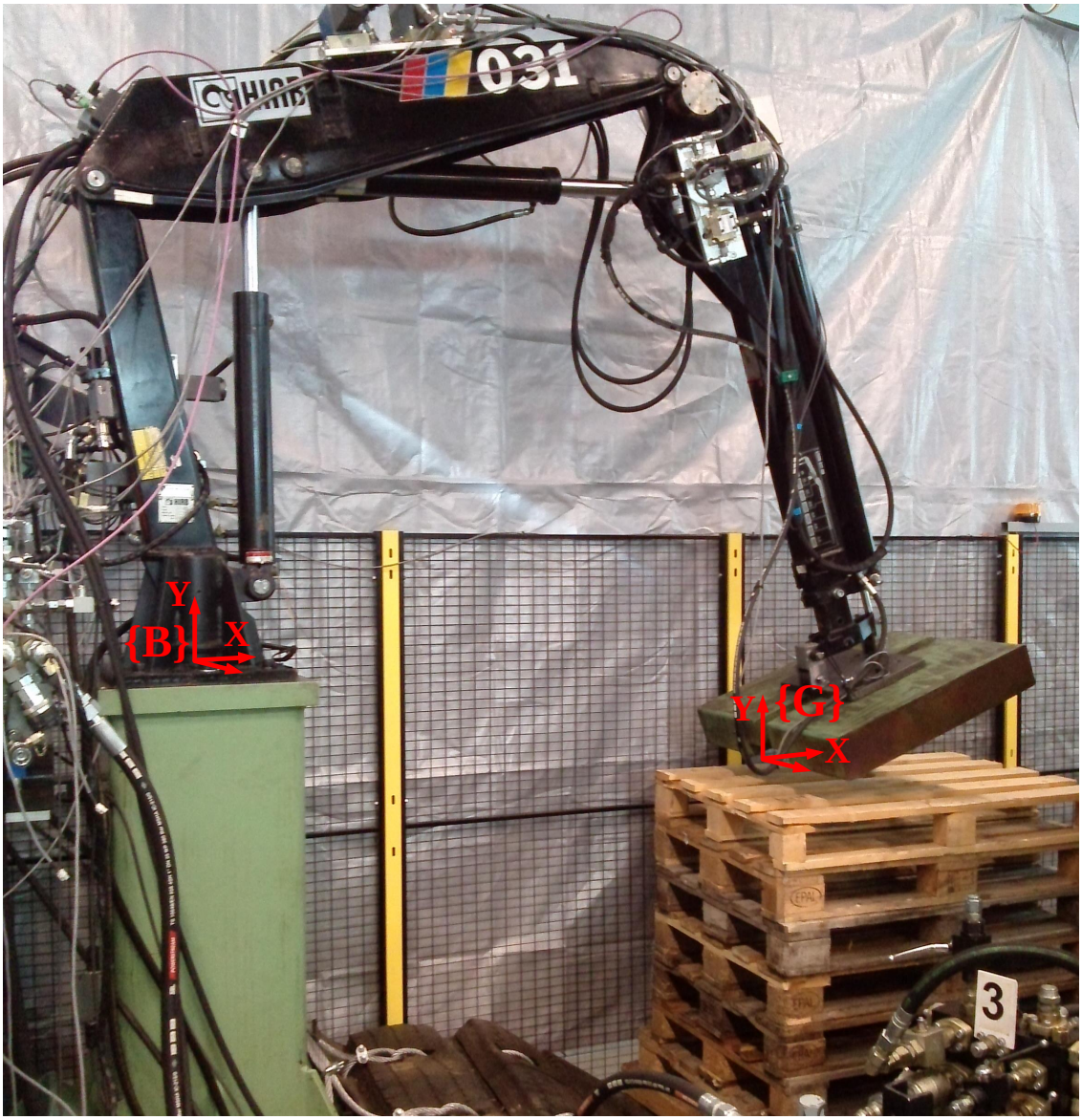

Figure 5.2 *Hiab 031 hydraulic manipulator and the experiment environment. [15]*

Control of the slave manipulator was done in a similar manner as with the master manipulator in Chapter 3, using VDC approach. Control system for the master manipulator had been implemented first in [23]. Further, a fast parameter adaptation algorithm was implemented on the control system to compensate parametric uncertainties of the friction models and rigid body parameters, as shown in [15]. Virtual decomposition of the slave manipulator is shown in Figure 5.3(a-b) and a simple oriented graph of the system in Figure 5.3(c).

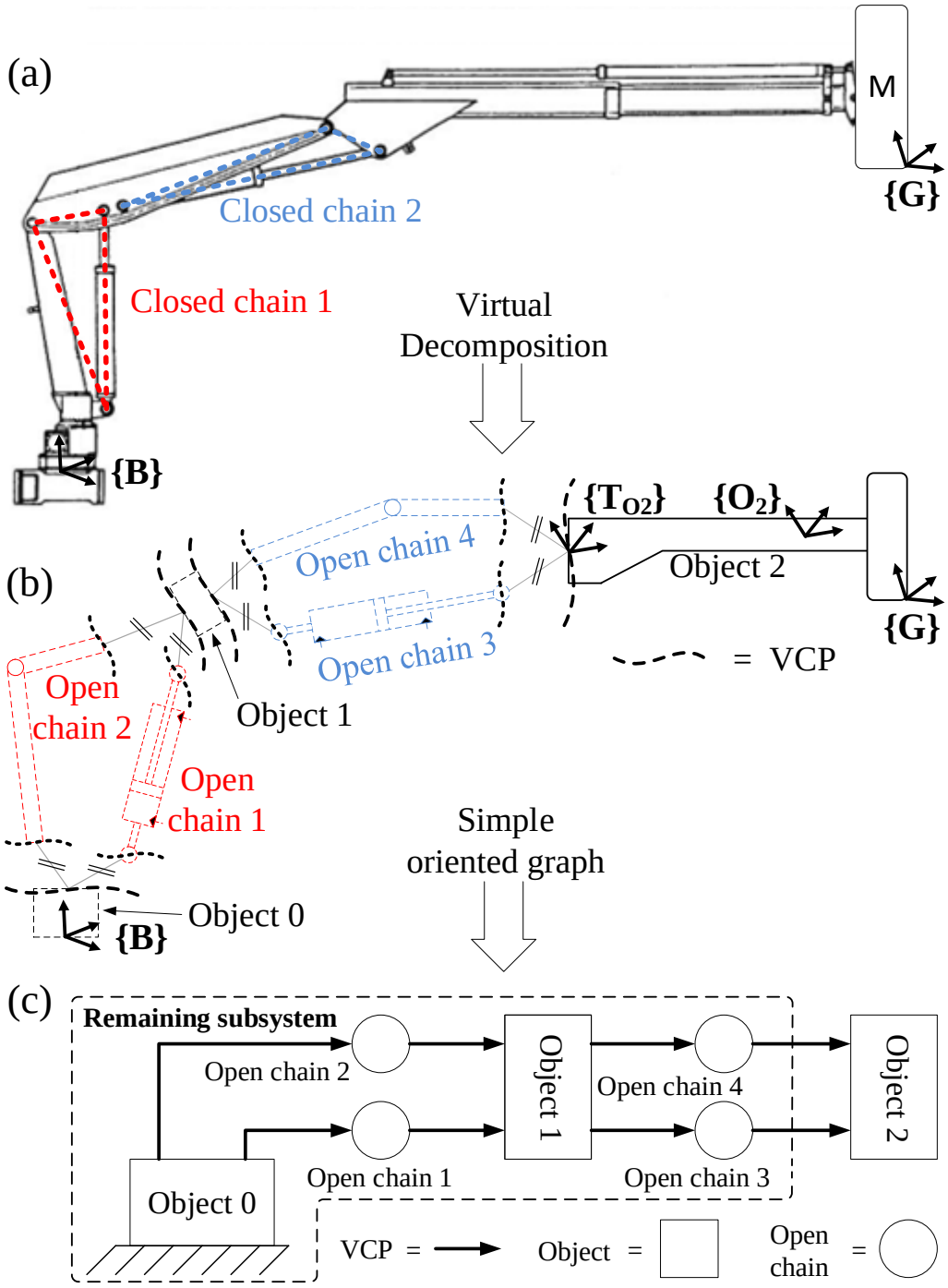

Figure 5.3 *Virtual Decomposition of the slave manipulator. [15]*

5.1.3 dSpace

Real time control system of the master and slave manipulators were implemented on a modular dSpace model DS1005 real time controller. The dSpace was equipped with real-time processor, along with analog and digital 16-bit I/O boards, and incremental encoder interface board, to accomplish the needs of measuring and control of the HIAB. Further,

a networking interface board was installed on the dSpace to enable communication with the host computer of the master manipulator.

Control system used to control the two manipulators along with the communication channel, was created with Simulink® block diagram environment, created by MathWorks®. Control loop used throughout the measurement was running at 1 ms sample time. Same sample time was used for the control loop of the phantom host computer, translating communications between the dSpace and the Phantom Premium.

Monitoring of the system signals as well as adjusting control parameter was done with yet another separate computer, connected to the dSpace, running dSpace ControlDesk 5.6. All the measurements during the experiments were also captured using the ControlDesk. The same computer, used for monitoring system data, was also used to compile real-time code and upload it to the dSpace.

Since velocity measurement was necessary in the framework of VDC approach, but both master and slave manipulators were equipped with only incremental encoders providing joint angles, derivative of the joint angles was necessary to compute. Further, due to noise in the measurement signal, simple backward differential would lead to a very noisy outputs, an estimation algorithm, given in [42], was used to estimate all necessary derivatives. The estimation algorithm in [42] is formed as

$$\dot{x}(kh) = \frac{5x(kh)+3x(kh-h)+x(kh-2h)-x(kh-3h)-3x(kh-4h)-5x(5h)}{35h}, \tag{5.3}$$

where h is the sample time of the control loop, x is the signal being derived and $\dot{x}$ is the derivative of x. The estimate of the derivative of x is based on five past values of x.

5.2 Results and Discussion

This section presents results from initial measurements, obtained using the novel VDC approach and the teleoperation scheme, presented in this thesis. Measurements shown in this section, present motion tracking performance of the experimental teleoperation system, discuss shortly about the successfulness of the controller design for the phantom premium, and evaluate the obtained results.

5.2.1 Evaluation of VDC Controller for the Phantom Premium

Control design for the Phantom Premium 3.0L 6-DOF haptic manipulator was successful and worked as intended. The performance of the controller was evaluated using rather subjective method of holding the manipulator by hand and moving it around within the workspace of the manipulator. Without the VDC controller, the manipulator felt "heavy" to move around due to its gravity and inertia. When the controller was turned on, the manipulator felt "weightless" and was easy to move around even near the edges of the workspace, where the gravity of the manipulator felt the largest without the controller.

Another evaluated aspect on the controllers performance was the ability to create artificial forces with the communication block. Further, the performance of the designed force estimation method was evaluated at the same time. This was done by placing a virtual spring on the workspace of the manipulator. When the operator tried to push against the spring, the controller generated a force opposing the operator, proportional to the displacement from the nominal position of the spring. This is presented in Figure 5.4.

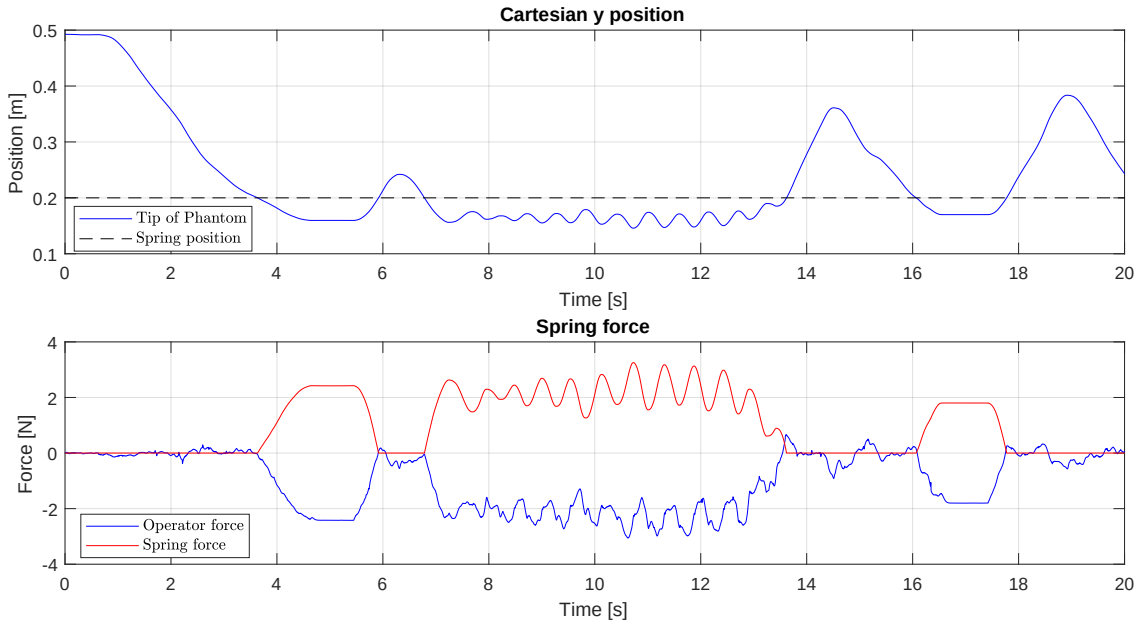

Figure 5.4 *Virtual spring on Y-axis of the master manipulator*

As the above figure shows, the virtual spring is placed at the height of 0,2 m. Below that level, the spring generates force toward positive Y-axis. Force estimation results are also presented in the same figure. Based on the results, the exogenous force estimation is working as it should. The small differences on the estimated forces, compared to the spring force, and also force when no contact with the spring occurs, are caused by dynamic forces exerted by the operator to move the manipulator around. Further, based on subjective results from the experiment, the virtual spring felt intuitive and real.

5.2.2 Free Space Motion Tracking

Experiments concerning the teleoperation system were done solely in free motion with no contact to environment. In free space motion, the most notable measurable signals to analyze performance of the teleoperation system are position and velocity tracking between the two manipulators.

Due to unfortunate events before the experiments, one of the motors generating torque for the force feedback of the Phantom broke down before measurement's from the teleoperation experiments were conducted. As a result, all the experimental results shown here are conducted with an incomplete system. In all the experiments, force feedback gain $\mathbf{A}$ was set to zero.

In the measurements, the pushbutton on the handle of the master manipulator was mapped to engage control of the slave manipulator. When the button was pressed, position of the slave manipulator and the master manipulator was set to zero in view of the communication channel. This allowed better position scaling between the two manipulators and also the position error between the manipulators is initially set to zero. Measurements shown in Figures 5.5–5.7 are obtained from arbitrarily moving the master manipulator around its workspace.

The following parameters, shown in Table 5.2, were used throughout the measurements. $\mathbf{K_{rigids}}$ denotes velocity feedback gain for each rigid body, $\mathbf{K_{fp\,cyl1}}$ and $\mathbf{K_{fp\,cyl2}}$ the force feedback gain of cylinder 1 and 2, respectively, and $\mathbf{K_{x\,cyl1}}$ and $\mathbf{K_{x\,cyl2}}$ the velocity feedback gain of cylinder 1 and 2, respectively.

Table 5.2 *Parameters used in the experimets*

Communication Channel	Slave Manipulator
$\boldsymbol{\kappa_p}$ = 1.0	$\mathbf{K_{x\,cyl1}} = 0.055$
$\boldsymbol{\kappa_f}$ = 1.0	$\mathbf{K_{fp\,cyl1}} = 4.00 \cdot 10^{-8}$
$\mathbf{\Lambda}$ = 4.0	$\mathbf{K_{x\,cyl2}} = 0.040$
$\mathbf{A}$ = 0	$\mathbf{K_{fp\,cyl2}} = 7.00 \cdot 10^{-8}$
$\mathbf{C}$ = 30	$\mathbf{K_{rigids}} = 700$

Figure 5.5 presents position tracking results from the teleoperation experiment. Biased position of the master and slave manipulator means that the position offset at the beginning of time has been set to zero. Because position scaling was set to 1, the slave manipulator replicated motion of the master manipulator exactly. As seen from the figure, position tracking accuracy is exceptionally good for a nonlinear hydraulic manipulator having almost 500 kg mass attached to its tip. Tracking error in Cartesian X-direction is at most 14,3 mm and in Y-direction 4,5 mm.

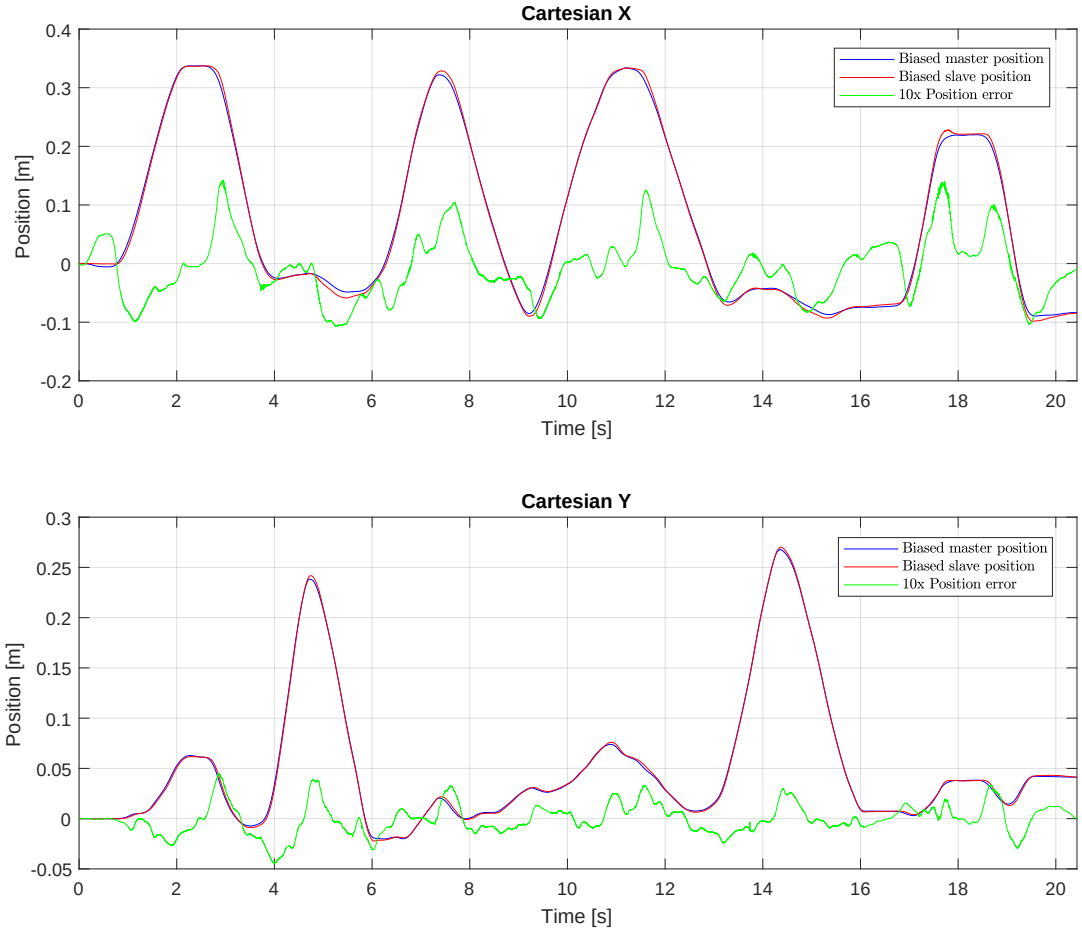

Figure 5.5 *Biased positions of the master and slave manipulator*

Figure 5.6 presents velocity tracking results from the same experiment. The desired velocity of the slave manipulator is calculated in the communication block, as shown in chapter 4. In the measurements, maximum velocity tracking error in Cartesian space was in X-direction 0.118 m/s and in Y-direction 0.055 m/s. Velocity tracking results of the slave manipulator are also presented in cylinder space, in Figure 5.7.

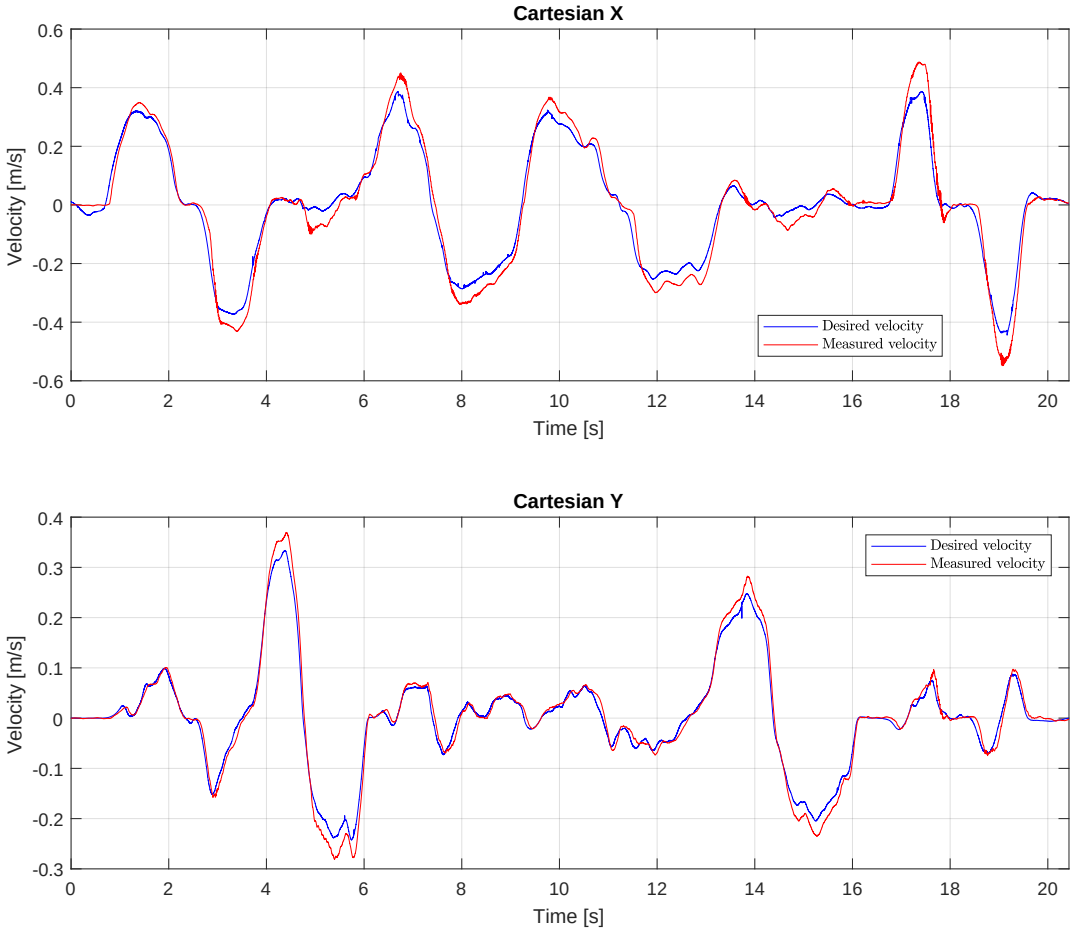

Figure 5.6 *Velocity tracking of the slave manipulator*

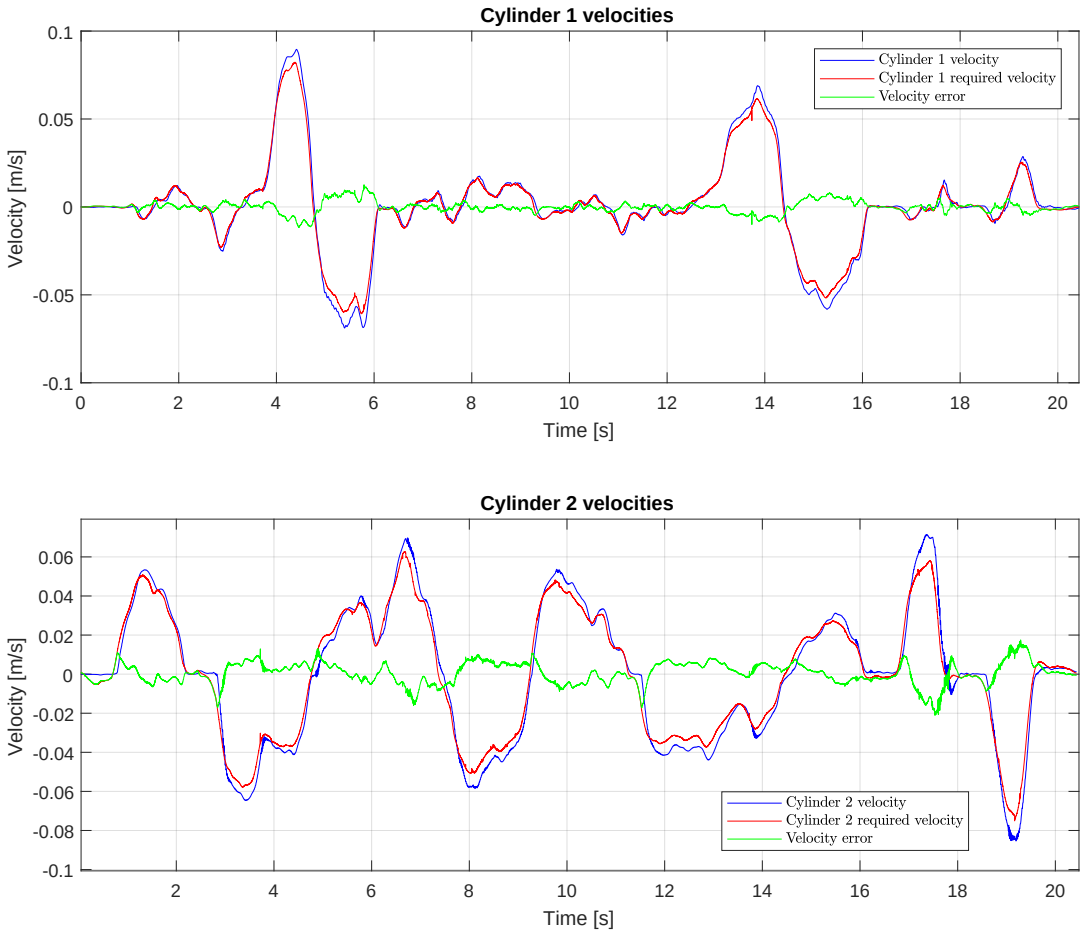

Figure 5.7 *Slave manipulator's velocity tracking in cylinder space*

6. CONCLUSIONS AND FUTURE WORK

Goal of this thesis was to design a controller for the Phantom Premium 3.0L 6-DOF haptic manipulator according to VDC approach, and develop a teleoperation system to connect the aforementioned manipulator to a HIAB 031 hydraulic manipulator, for which the controller had been developed first in [23]. In order to develop the controller for the Phantom Premium, kinematics and dynamics of the manipulator was first identified. In addition, a force estimation method was developed to identify exogenous forces exerted by the operator, without a force sensor. Further, aim of this thesis was to evaluate the performance of the designed teleoperation scheme with measurements done in free space teleoperation as well as having the slave manipulator interact with flexible environment.

This thesis had two novel features that as of the knowledge of the author, haven't been implemented before. First, force-sensorless force estimation was used within the concept of VDC to estimate exogenous forces of an electrically driven manipulator. Similar method has been applied in [23] for a hydraulic manipulator, where cylinder forces were estimated from cylinder pressures. Second, an electric manipulator was used to control a hydraulic manipulator, with both manipulators independently controlled with VDC, and using teleoperation scheme, presented in [17], to connect the manipulators to each other.

The designed controller for the Phantom Premium was found effective and capable. Unfortunately one motor of the manipulator broke before obtaining measurements from the experimental implementation. Due to this, measurements of the experimental implementation were carried out with a simplified form. The force feedback of the master manipulator was disabled and the performance of the teleoperation system was evaluated only in free space motion.

Experimental results from the teleoperation indicate that a good motion tracking was achievable, and even with very little tuning of the system parameters, maximum error of the position tracking was less than 15 mm in Cartesian X-direction, and less than 5 mm in Y-direction. The difference between x- and Y-direction is an indirect result of problematic dynamical behavior of the cylinder 2 of the HIAB. In the posture of the slave manipulator during the experiments, cylinder 2 was mostly responsible of Cartesian X-direction motion.

As future studies, the teleoperation system should be evaluated further. Controlling the slave manipulator in environments with flexible and rigid constraints was originally intended as a part of this thesis, but couldn't be tested since the Phantom broke down. Another possible future study would be to implement parameter adaptation for the controller of the Phantom Premium to overcome parametric uncertainties. Although this might prove unnecessary due to small masses of the manipulator and the linear behavior of electric motors.

BIBLIOGRAPHY

[1] euRobotics, "Strategic research agenda for robotics in europe 2014–2020." Available: https://www.eu-robotics.net/cms/upload/topic_groups/SRA2020_SPARC.pdf

[2] P. F. Hokayem and M. W. Spong, "Bilateral teleoperation: An historical survey," *Automatica*, vol. 42, no. 12, pp. 2035 – 2057, 2006.

[3] M. Krstić, I. Kanellakopoulos, and P. Kokotović, *Nonlinear and adaptive control design*, ser. Adaptive and learning systems for signal processing, communications, and control. Wiley, 1995.

[4] J. Slotine and W. Li, *Applied Nonlinear Control*. Prentice Hall, 1991.

[5] W.-H. Zhu, *Virtual decomposition control: toward hyper degrees of freedom robots*, 1st ed. Springer Science & Business Media, 2010, vol. 60.

[6] W.-H. Zhu, Z. Bien, and J. D. Schutter, "Adaptive motion/force control of multiple manipulators with joint flexibility based on virtual decomposition," *IEEE Transactions on Automatic Control*, vol. 43, no. 1, pp. 46–60, Jan 1998.

[7] W.-H. Zhu and J. D. Schutter, "Experiment with two industrial robot manipulators rigidly holding an egg," in *Proceedings. 1998 IEEE International Conference on Robotics and Automation (Cat. No.98CH36146)*, vol. 2, May 1998, pp. 1534–1539 vol.2.

[8] W.-H. Zhu and J. D. Schutter, "Adaptive control of mixed rigid/flexible joint robot manipulators based on virtual decomposition," *IEEE Transactions on Robotics and Automation*, vol. 15, no. 2, pp. 310–317, Apr 1999.

[9] W.-H. Zhu and J. D. Schutter, "Experimental verifications of virtual-decomposition-based motion/force control," *IEEE Transactions on Robotics and Automation*, vol. 18, no. 3, pp. 379–386, Jun 2002.

[10] W.-H. Zhu and G. Vukovich, "Virtual decomposition control for modular robot manipulators," *IFAC Proceedings Volumes*, vol. 44, no. 1, pp. 13 486 – 13 491, 2011, 18th IFAC World Congress.

[11] W.-H. Zhu and J.-C. Piedboeuf, "Adaptive output force tracking control of hydraulic cylinders with applications to robot manipulators," *Journal of dynamic systems, measurement, and control*, vol. 127, no. 2, pp. 206–217, 2005.

[12] J. Koivumäki and J. Mattila, "The automation of multi degree of freedom hydraulic crane by using virtual decomposition control," in *2013 IEEE/ASME International Conference on Advanced Intelligent Mechatronics*, July 2013, pp. 912–919.

[13] J. Koivumäki and J. Mattila, "An energy-efficient high performance motion control of a hydraulic crane applying virtual decomposition control," in *2013 IEEE/RSJ International Conference on Intelligent Robots and Systems*, Nov 2013, pp. 4426–4433.

[14] J. Koivumäki and J. Mattila, "Stability-guaranteed force-sensorless contact force/-motion control of heavy-duty hydraulic manipulators," *IEEE Transactions on Robotics*, vol. 31, no. 4, pp. 918–935, Aug 2015.

[15] J. Koivumäki and J. Mattila, "Stability-guaranteed impedance control of hydraulic robotic manipulators," *IEEE/ASME Transactions on Mechatronics*, vol. 22, no. 2, pp. 601–612, April 2017.

[16] J. Koivumäki and J. Mattila, "High performance nonlinear motion/force controller design for redundant hydraulic construction crane automation," *Automation in Construction*, vol. 51, no. Supplement C, pp. 59 – 77, 2015.

[17] W.-H. Zhu and S. E. Salcudean, "Stability guaranteed teleoperation: an adaptive motion/force control approach," *IEEE Transactions on Automatic Control*, vol. 45, no. 11, pp. 1951–1969, Nov 2000.

[18] L. Sciavicco and B. Siciliano, *Modelling and Control of Robot Manipulators*, 2nd ed., ser. Advanced Textbooks in Control and Signal Processing. Springer-Verlag London, 2012.

[19] R. N. Jazar, *Theory of applied robotics: kinematics, dynamics, and control*, 2nd ed. Springer Science & Business Media, 2010.

[20] J. Craig, *Introduction to Robotics: Mechanics and Control*, 3rd ed., ser. Addison-Wesley series in electrical and computer engineering: control engineering. Pearson/Prentice Hall, 2005.

[21] Chartrand, *Directed Graphs as Mathematical Models*. Courier Dover Publications, 1985, pp. 16–19.

[22] W.-H. Zhu, "Advanced robotics control - the virtual decomposition control approach," p. 117, 2014, presentation slides.

[23] J. Koivumäki, *Virtual decomposition control of a hydraulic manipulator: Master of Science Thesis*. Tampere: Tampere University of Technology, 2012.

[24] 3DSystems, *OpenHaptics Toolkit*, 2015, [Online]. Seen: 21 August 2017. Available: https://3dsystems.teamplatform.com/pages/102773?t=3g4x4z9prybr

[25] J. Funda, R. H. Taylor, B. Eldridge, S. Gomory, and K. G. Gruben, "Constrained cartesian motion control for teleoperated surgical robots," *IEEE Transactions on Robotics and Automation*, vol. 12, no. 3, pp. 453–465, Jun 1996.

[26] A. A. Goldenberg, J. Wiercienski, P. Kuzan, C. Szymczyk, R. G. Fenton, and B. Shaver, "A remote manipulator for forestry operation," *IEEE Transactions on Robotics and Automation*, vol. 11, no. 2, pp. 185–197, Apr 1995.

[27] S. Westerberg, I. R. Manchester, U. Mettin, P. L. Hera, and A. Shiriaev, "Virtual environment teleoperation of a hydraulic forestry crane," in *2008 IEEE International Conference on Robotics and Automation*, May 2008, pp. 4049–4054.

[28] K. A. Manocha, N. Pernalete, and R. V. Dubey, "Variable position mapping based assistance in teleoperation for nuclear cleanup," in *Proceedings 2001 ICRA. IEEE International Conference on Robotics and Automation (Cat. No.01CH37164)*, vol. 1, 2001, pp. 374–379 vol.1.

[29] G. Immega and K. Antonelli, "The ksi tentacle manipulator," in *Proceedings of 1995 IEEE International Conference on Robotics and Automation*, vol. 3, May 1995, pp. 3149–3154 vol.3.

[30] M. Viinikainen, *Computer-aided bilateral teleoperation of manipulators: Master of Science Thesis*. Tampere: Tampere University of Technology, 2014.

[31] T. B. Sheridan, "Space teleoperation through time delay: review and prognosis," *IEEE Transactions on Robotics and Automation*, vol. 9, no. 5, pp. 592–606, Oct 1993.

[32] T. B. Sheridan, "Telerobotics," *Automatica*, vol. 25, no. 4, pp. 487–507, 1989.

[33] D. A. Lawrence, "Stability and transparency in bilateral teleoperation," *IEEE Transactions on Robotics and Automation*, vol. 9, no. 5, pp. 624–637, Oct 1993.

[34] G. J. Raju, G. C. Verghese, and T. B. Sheridan, "Design issues in 2-port network models of bilateral remote manipulation," in *Proceedings, 1989 International Conference on Robotics and Automation*, May 1989, pp. 1316–1321 vol.3.

[35] S. Hirche, M. Ferre, J. Barrio, C. Melchiorri, and M. Buss, *Bilateral Control Architectures for Telerobotics*. Berlin, Heidelberg: Springer Berlin Heidelberg, 2007, pp. 163–176.

[36] R. J. Anderson and M. W. Spong, "Bilateral control of teleoperators with time delay," *IEEE Transactions on Automatic Control*, vol. 34, no. 5, pp. 494–501, May 1989.

[37] R. J. Anderson and M. W. Spong, "Asymptotic stability for force reflecting teleoperators with time delays," in *Proceedings, 1989 International Conference on Robotics and Automation*, May 1989, pp. 1618–1625 vol.3.

[38] G. M. H. Leung, B. A. Francis, and J. Apkarian, "Bilateral controller for teleoperators with time delay via mu;-synthesis," *IEEE Transactions on Robotics and Automation*, vol. 11, no. 1, pp. 105–116, Feb 1995.

[39] H. Kazerooni and M.-G. Her, "The dynamics and control of a haptic interface device," *IEEE Transactions on Robotics and Automation*, vol. 10, no. 4, pp. 453–464, Aug 1994.

[40] J. D. Cooke, "Dependence of human arm movements on limb mechanical properties," *Brain Research*, vol. 165, no. 2, pp. 366–369, 1979.

[41] G. Tao, "A simple alternative to the barbalat lemma," *IEEE Transactions on Automatic Control*, vol. 42, no. 5, pp. 698–, May 1997.

[42] A. J. L. Harrison and D. P. Stoten, "Generalized finite difference methods for optimal estimation of derivatives in real-time control problems," *Proceedings of the Institution of Mechanical Engineers, Part I: Journal of Systems and Control Engineering*, vol. 209, no. 2, pp. 67–78, 1995.

APPENDIX A. APPLIED REGRESSOR MATRIX AND PARAMETER VECTOR

This appendix presents the applied regressor matrix, $\mathbf{Y_{2A}} \in \mathbb{R}^{6\times 6}$, and parameter vector, $\boldsymbol{\theta}_\mathbf{A} \in \mathbb{R}^6$, used for virtual decomposition control and defined in [23], Appendix B. The regressor matrix is designed for a rigid body attached to frame $\{\mathbf{A}\}$ and covers only 2 DOF dynamics of the rigid body. It is simplified from the original 6 DOF version which has much more elements to compute.

The non-zero elements of the regressor matrix are listed as

$$y_\mathbf{A}(1,1) = \frac{d}{dt}({}^\mathbf{A}v_r)(1) - {}^\mathbf{A}v(6){}^\mathbf{A}v_r(2) + {}^\mathbf{A}g(1) \tag{A.1}$$
$$y_\mathbf{A}(1,2) = -{}^\mathbf{A}v(6){}^\mathbf{A}v_r(6) \tag{A.2}$$
$$y_\mathbf{A}(1,3) = -\frac{d}{dt}({}^\mathbf{A}v_r)(6) \tag{A.3}$$
$$y_\mathbf{A}(2,1) = \frac{d}{dt}({}^\mathbf{A}v_r)(2) - {}^\mathbf{A}v(6){}^\mathbf{A}v_r(1) + {}^\mathbf{A}g(2) \tag{A.4}$$
$$y_\mathbf{A}(2,2) = -y_\mathbf{A}(1,3) \tag{A.5}$$
$$y_\mathbf{A}(2,3) = \ \ y_\mathbf{A}(1,2) \tag{A.6}$$
$$y_\mathbf{A}(6,2) = \ \ y_\mathbf{A}(2,1) \tag{A.7}$$
$$y_\mathbf{A}(6,3) = -y_\mathbf{A}(1,1) \tag{A.8}$$
$$y_\mathbf{A}(6,4) = \ \ y_\mathbf{A}(2,2) \tag{A.9}$$
$$y_\mathbf{A}(6,5) = -y_\mathbf{A}(1,3) \tag{A.10}$$
$$y_\mathbf{A}(6,6) = -y_\mathbf{A}(1,3) \tag{A.11}$$

The applied regressor matrix can then be presented using equations (A.1) – (A.11) as

$$\mathbf{Y_{2A}} = \begin{bmatrix} y_\mathbf{A}(1,1) & y_\mathbf{A}(1,2) & y_\mathbf{A}(1,3) & 0 & 0 & 0 \\ y_\mathbf{A}(2,1) & y_\mathbf{A}(2,2) & y_\mathbf{A}(2,3) & 0 & 0 & 0 \\ y_\mathbf{A}(3,1) & y_\mathbf{A}(3,2) & y_\mathbf{A}(3,3) & 0 & 0 & 0 \\ 0 & 0 & 0 & 0 & 0 & 0 \\ 0 & 0 & 0 & 0 & 0 & 0 \\ 0 & y_\mathbf{A}(6,2) & y_\mathbf{A}(6,3) & y_\mathbf{A}(6,4) & y_\mathbf{A}(6,5) & y_\mathbf{A}(6,6) \end{bmatrix} \tag{A.12}$$

The applied parameter vector can be written as

$$\boldsymbol{\theta_{2A}} = \begin{bmatrix} m_{\mathbf{A}} \\ m_{\mathbf{A}}{}^{\mathbf{A}}r_{mx} \\ m_{\mathbf{A}}{}^{\mathbf{A}}r_{my} \\ m_{\mathbf{A}}{}^{\mathbf{A}}r_{mx}^2 \\ m_{\mathbf{A}}{}^{\mathbf{A}}r_{my}^2 \\ I_{\mathbf{A}zz} \end{bmatrix}, \tag{A.13}$$

where $m_{\mathbf{A}}$ denotes the mass of the rigid body, ${}^{\mathbf{A}}r_{mx}$ and ${}^{\mathbf{A}}r_{my}$ the x and y coordinate of the center of mass with respect to the appropriate body frame, respectively, and $I_{\mathbf{A}zz}$ the moment of inertia of the rigid body around z-axis, measured from the center of mass.

APPENDIX B. FORWARD KINEMATICS OF PHANTOM PREMIUM

$$A_{T_{tcp}}^{B_0} = \begin{bmatrix} R_{11} & R_{12} & R_{13} & P_x \\ R_{21} & R_{22} & R_{23} & P_y \\ R_{31} & R_{32} & R_{33} & P_z \\ 0 & 0 & 0 & 1 \end{bmatrix}, \tag{B.1}$$

where

$$\begin{aligned} R_{11} = {} & \cos(\theta_6)\,(\cos(\theta_5)\,(\cos(\theta_2+\theta_3)\,\cos(\theta_1)\,\cos(\theta_4) \\ & -\sin(\theta_2+\theta_3)\,\cos(\theta_1)\,\sin(\theta_4)) - \sin(\theta_1)\,\sin(\theta_5)) \\ & -\sin(\theta_6)\,(\cos(\theta_2+\theta_3)\,\cos(\theta_1)\,\sin(\theta_4) \\ & +\sin(\theta_2+\theta_3)\,\cos(\theta_1)\,\cos(\theta_4)) \end{aligned} \tag{B.2}$$

$$\begin{aligned} R_{21} = {} & \cos(\theta_6)\,(\cos(\theta_1)\,\sin(\theta_5) \\ & +\cos(\theta_5)\,(\cos(\theta_2+\theta_3)\,\cos(\theta_4)\,\sin(\theta_1) \\ & -\sin(\theta_2+\theta_3)\,\sin(\theta_1)\,\sin(\theta_4))) \\ & -\sin(\theta_6)\,(\cos(\theta_2+\theta_3)\,\sin(\theta_1)\,\sin(\theta_4) \\ & +\sin(\theta_2+\theta_3)\,\cos(\theta_4)\,\sin(\theta_1)) \end{aligned} \tag{B.3}$$

$$\begin{aligned} R_{31} = {} & \cos(\theta_2+\theta_3+\theta_4)\,\sin(\theta_6) \\ & +\sin(\theta_2+\theta_3+\theta_4)\,\cos(\theta_5)\,\cos(\theta_6) \end{aligned} \tag{B.4}$$

$$\begin{aligned} R_{12} = {} & -\sin(\theta_6)\,(\cos(\theta_5)\,(\cos(\theta_2+\theta_3)\,\cos(\theta_1)\,\cos(\theta_4) \\ & -\sin(\theta_2+\theta_3)\,\cos(\theta_1)\,\sin(\theta_4)) - \sin(\theta_1)\,\sin(\theta_5)) \\ & -\cos(\theta_6)\,(\cos(\theta_2+\theta_3)\,\cos(\theta_1)\,\sin(\theta_4) \\ & +\sin(\theta_2+\theta_3)\,\cos(\theta_1)\,\cos(\theta_4)) \end{aligned} \tag{B.5}$$

$$\begin{aligned} R_{22} = {} & -\sin(\theta_6)\,(\cos(\theta_1)\,\sin(\theta_5) \\ & +\cos(\theta_5)\,(\cos(\theta_2+\theta_3)\,\cos(\theta_4)\,\sin(\theta_1) \\ & -\sin(\theta_2+\theta_3)\,\sin(\theta_1)\,\sin(\theta_4))) \\ & -\cos(\theta_6)\,(\cos(\theta_2+\theta_3)\,\sin(\theta_1)\,\sin(\theta_4) \\ & +\sin(\theta_2+\theta_3)\,\cos(\theta_4)\,\sin(\theta_1)) \end{aligned} \tag{B.6}$$

$$\begin{aligned} R_{32} = {} & \cos(\theta_2+\theta_3+\theta_4)\,\cos(\theta_6) \\ & -\sin(\theta_2+\theta_3+\theta_4)\,\cos(\theta_5)\,\sin(\theta_6) \end{aligned} \tag{B.7}$$

$$\begin{aligned} \boldsymbol{R_{13}} = & \ \mathbf{cos}(\boldsymbol{\theta_5})\ \mathbf{sin}(\boldsymbol{\theta_1}) \\ & + \mathbf{sin}(\boldsymbol{\theta_5})\ (\mathbf{cos}(\boldsymbol{\theta_2}+\boldsymbol{\theta_3})\ \mathbf{cos}(\boldsymbol{\theta_1})\ \mathbf{cos}(\boldsymbol{\theta_4}) \\ & - \mathbf{sin}(\boldsymbol{\theta_2}+\boldsymbol{\theta_3})\ \mathbf{cos}(\boldsymbol{\theta_1})\ \mathbf{sin}(\boldsymbol{\theta_4})) \end{aligned} \tag{B.8}$$

$$\begin{aligned} \boldsymbol{R_{23}} = & \ \mathbf{sin}(\boldsymbol{\theta_5})\ (\mathbf{cos}(\boldsymbol{\theta_2}+\boldsymbol{\theta_3})\ \mathbf{cos}(\boldsymbol{\theta_4})\ \mathbf{sin}(\boldsymbol{\theta_1}) \\ & - \mathbf{sin}(\boldsymbol{\theta_2}+\boldsymbol{\theta_3})\ \mathbf{sin}(\boldsymbol{\theta_1})\ \mathbf{sin}(\boldsymbol{\theta_4})) - \mathbf{cos}(\boldsymbol{\theta_1})\ \mathbf{cos}(\boldsymbol{\theta_5}) \end{aligned} \tag{B.9}$$

$$\boldsymbol{R_{33}} = \ \mathbf{sin}(\boldsymbol{\theta_2}+\boldsymbol{\theta_3}+\boldsymbol{\theta_4})\ \mathbf{sin}(\boldsymbol{\theta_5}) \tag{B.10}$$

$$\boldsymbol{P_x} = \boldsymbol{l_1}\ \mathbf{cos}(\boldsymbol{\theta_1})\ (\mathbf{cos}(\boldsymbol{\theta_2}+\boldsymbol{\theta_3}) + \mathbf{cos}(\boldsymbol{\theta_2})) \tag{B.11}$$

$$\boldsymbol{P_y} = \boldsymbol{l_1}\ \mathbf{sin}(\boldsymbol{\theta_1})\ (\mathbf{cos}(\boldsymbol{\theta_2}+\boldsymbol{\theta_3}) + \mathbf{cos}(\boldsymbol{\theta_2})) \tag{B.12}$$

$$\boldsymbol{P_z} = \boldsymbol{l_1}\ (\mathbf{sin}(\boldsymbol{\theta_2}+\boldsymbol{\theta_3}) + \mathbf{sin}(\boldsymbol{\theta_2}) + \mathbf{1}), \tag{B.13}$$

where $l_1 = 460mm$.

$$\mathbf{J}_D = \begin{bmatrix} \frac{\partial p_x}{\partial \theta_1} & \frac{\partial p_x}{\partial \theta_2} & \frac{\partial p_x}{\partial \theta_3} \\ \frac{\partial p_y}{\partial \theta_1} & \frac{\partial p_y}{\partial \theta_2} & \frac{\partial p_y}{\partial \theta_3} \\ \frac{\partial p_z}{\partial \theta_1} & \frac{\partial p_z}{\partial \theta_2} & \frac{\partial p_z}{\partial \theta_3} \end{bmatrix} \tag{B.14}$$

where

$$\frac{\partial p_x}{\partial \theta_1} = -l_1\ \sin(\theta_1)\ (\cos(\theta_2+\theta_3) + \cos(\theta_2)) \tag{B.15}$$

$$\frac{\partial p_x}{\partial \theta_2} = -l_1\ \cos(\theta_1)\ (\sin(\theta_2+\theta_3) + \sin(\theta_2)) \tag{B.16}$$

$$\frac{\partial p_x}{\partial \theta_3} = -l_1\ \sin(\theta_2+\theta_3)\ \cos(\theta_1) \tag{B.17}$$

$$\frac{\partial p_y}{\partial \theta_1} = l_1\ \cos(\theta_1)\ (\cos(\theta_2+\theta_3) + \cos(\theta_2)) \tag{B.18}$$

$$\frac{\partial p_y}{\partial \theta_2} = -l_1\ \sin(\theta_1)\ (\sin(\theta_2+\theta_3) + \sin(\theta_2)) \tag{B.19}$$

$$\frac{\partial p_y}{\partial \theta_3} = -l_1\ \sin(\theta_2+\theta_3)\ \sin(\theta_1) \tag{B.20}$$

$$\frac{\partial p_z}{\partial \theta_1} = 0 \tag{B.21}$$

$$\frac{\partial p_z}{\partial \theta_2} = l_1\ (\cos(\theta_2+\theta_3) + \cos(\theta_2)) \tag{B.22}$$

$$\frac{\partial p_z}{\partial \theta_3} = l_1\ \cos(\theta_2+\theta_3) \tag{B.23}$$

inversely

$$\mathbf{J}_D^{-1} = \begin{bmatrix} -\frac{\sin(\theta_1)}{l_1\,(\cos(\theta_2+\theta_3)+\cos(\theta_2))} & \frac{\cos(\theta_1)}{l_1\,(\cos(\theta_2+\theta_3)+\cos(\theta_2))} & 0 \\ \frac{\cos(\theta_2+\theta_3)\,\cos(\theta_1)}{l_1\,\sin(\theta_3)} & \frac{\cos(\theta_2+\theta_3)\,\sin(\theta_1)}{l_1\,\sin(\theta_3)} & \frac{\sin(\theta_2+\theta_3)}{l_1\,\sin(\theta_3)} \\ -\frac{\cos(\theta_1)\,(\cos(\theta_2+\theta_3)+\cos(\theta_2))}{l_1\,\sin(\theta_3)} & -\frac{\sin(\theta_1)\,(\cos(\theta_2+\theta_3)+\cos(\theta_2))}{l_1\,\sin(\theta_3)} & -\frac{\sin(\theta_2+\theta_3)+\sin(\theta_2)}{l_1\,\sin(\theta_3)} \end{bmatrix} \tag{B.24}$$

APPENDIX C. DERIVATION OF LOAD DISTRIBUTION FACTORS

The derivation of the *load distribution factors* α_1 and α_2 are shown in this appendix. This appendix follows loosely the way shown in [23, p. 82]. The load distribution factors define how the forces at frame $\{\mathbf{T_{cc}}\}$ are distributed among rigid links based on geometric conditions. To calculate the load distribution factors, the resultant force at frame $\{\mathbf{T_{cc}}\}$, exerted on *cutting point 2*, and the joint variable θ_3 must be known.

First step in calculating the load distribution factors is to define the angle of the resultant force ${}^{\mathbf{T_{cc}}}\boldsymbol{F} \in \mathbb{R}^6$ with respect to the x-axis of the frame $\{\mathbf{T_{cc}}\}$. This can be done with a simple trigonometric calculus as

$$\alpha = \arctan\left(\frac{{}^{\mathbf{T_{cc}}}f_x}{{}^{\mathbf{T_{cc}}}f_y}\right). \tag{C.1}$$

Newtons third law states that when a body exerts a force to another body, the second body exerts simultaneously an equal counter force on the first body, that is equal in magnitude but opposite in direction. Accordingly the closed chain 1 must exert a reaction force $-{}^{\mathbf{T_{cc}}}F \in \mathbb{R}^6$ toward *driven cutting point* at $\{\mathbf{T_{cc}}\}$ This reaction force will further decompose into supporting reactive forces along the rigid links of the *closed chain*. These forces are f_{L22} and f_{L32} along link 22 and 32 axis, respectively. These supportive reaction forces can be projected into ${}^{\mathbf{T_{cc}}}f_{L22}$ and ${}^{\mathbf{T_{cc}}}f_{L32}$, parallel to ${}^{\mathbf{T_{cc}}}f$ and subject to

$$\left\|{}^{\mathbf{T_{cc}}}f_{L22}\right\| + \left\|{}^{\mathbf{T_{cc}}}f_{L32}\right\| = \left\|{}^{\mathbf{T_{cc}}}f\right\|. \tag{C.2}$$

Based on the constraint presented in (C.2), the projected reaction forces can be written as

$${}^{\mathbf{T_{cc}}}f_{L22} = \alpha_1 {}^{\mathbf{T_{cc}}}f \tag{C.3}$$

$${}^{\mathbf{T_{cc}}}f_{L32} = \alpha_2 {}^{\mathbf{T_{cc}}}f, \tag{C.4}$$

where α_1 and α_2 present the load distribution factors.

Figure C.1(a) demonstrates the load distribution and decomposition of ${}^{\mathbf{T_{cc}}}f$ into components parallel to the links of the *closed chain* at frame $\{\mathbf{T_{cc}}\}$. Projection of the decomposed forces into forces parallel to the resultant force of frame $\{\mathbf{T_{cc}}\}$ is presented in Figure C.1(b).

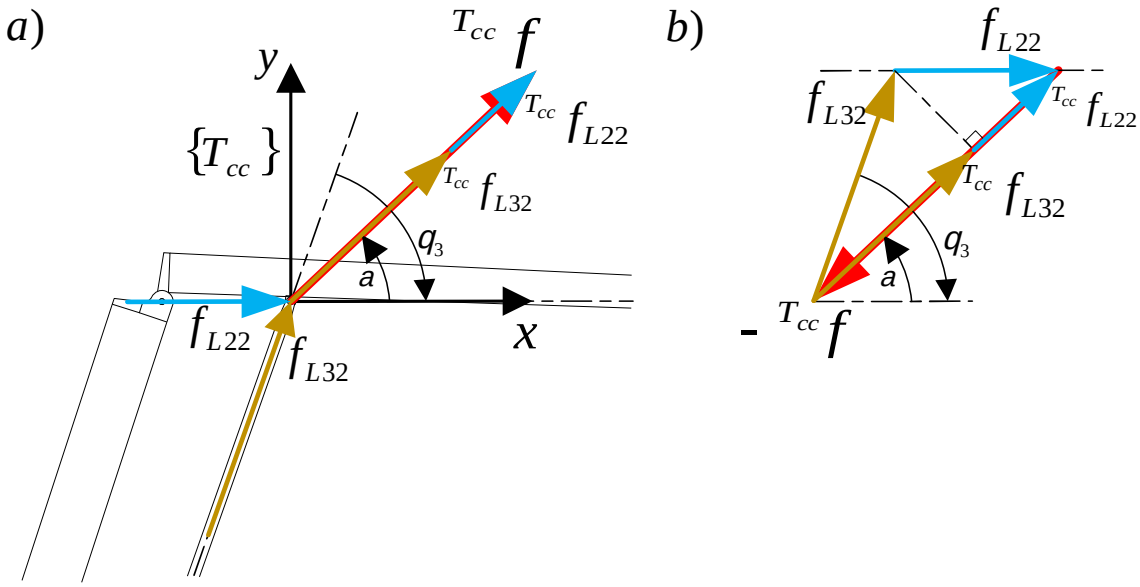

Figure C.1 *Load distribution at frame* $\{\mathbf{T_{cc}}\}$

The resultant force, ${}^{\mathbf{T_{cc}}}f$ $\left(\text{From the force/moment vector } {}^{\mathbf{T_{cc}}}F = \left[{}^{\mathbf{T_{cc}}}f \quad {}^{\mathbf{T_{cc}}}m\right]\right)$, can be obtained from (3.24) and the joint angle θ_3 is obtained from the manipulator's rotary encoders. Furthermore by using (C.1) – (C.4), the load distribution factors can be computed with some trigonometric calculations, notably the law of sines. Equations to calculate load distribution factors are given in (C.5) – (C.12).

According to law of sines, the composite forces $\|f_{L22}\|$ and $\|f_{L32}\|$ can be obtained as

$$\begin{aligned} & \frac{\|f_{L22}\|}{\sin(-\theta_3-\alpha)} = \frac{\left\|{}^{\mathbf{T_{cc}}}f\right\|}{\sin(\pi+\theta_3)} \\ \Leftrightarrow \quad & \|f_{L22}\| = \frac{\sin(-\theta_3-\alpha)}{\sin(\pi+\theta_3)}\left\|{}^{\mathbf{T_{cc}}}f\right\| \end{aligned} \tag{C.5}$$

$$\begin{aligned} & \frac{\|f_{L32}\|}{\sin(\alpha)} = \frac{\left\|{}^{\mathbf{T_{cc}}}f\right\|}{\sin(\pi+\theta_3)} \\ \Leftrightarrow \quad & \|f_{L32}\| = \frac{\sin(\alpha)}{\sin(\pi+\theta_3)}\left\|{}^{\mathbf{T_{cc}}}f\right\|. \end{aligned} \tag{C.6}$$

The composite forces can further be projected to be parallel to the resultant force ${}^{\mathbf{T_{cc}}}f$ with simple trigonometric computations as

$$\left\|{}^{\mathbf{T_{cc}}}f_{L22}\right\| = \cos(\alpha)\,\|f_{L22}\| \tag{C.7}$$

$$\left\|{}^{\mathbf{T_{cc}}}f_{L32}\right\| = \cos(-\theta_3-\alpha)\,\|f_{L32}\|. \tag{C.8}$$

Finally the load distribution factors can be computed as

$$\begin{aligned}
& \alpha_1 \left\| {}^{\mathbf{T_{cc}}} f \right\| = \left\| {}^{\mathbf{T_{cc}}} f_{L22} \right\| \\
\Leftrightarrow \quad & \alpha_1 \left\| {}^{\mathbf{T_{cc}}} f \right\| = \cos(\alpha) \left\| f_{L22} \right\| \\
\Leftrightarrow \quad & \alpha_1 \left\| {}^{\mathbf{T_{cc}}} f \right\| = \cos(\alpha) \frac{\sin(-\theta_3 - \alpha)}{\sin(\pi + \theta_3)} \left\| {}^{\mathbf{T_{cc}}} f \right\| \qquad \text{(C.9)} \\
\Leftrightarrow \quad & \alpha_1 = \cos(\alpha) \frac{\sin(-\theta_3 - \alpha)}{\sin(\pi + \theta_3)} \\
& \alpha_2 \left\| {}^{\mathbf{T_{cc}}} f \right\| = \left\| {}^{\mathbf{T_{cc}}} f_{L32} \right\| \\
\Leftrightarrow \quad & \alpha_2 \left\| {}^{\mathbf{T_{cc}}} f \right\| = \cos(-\theta_3 - \alpha) \left\| f_{L32} \right\| \\
\Leftrightarrow \quad & \alpha_2 \left\| {}^{\mathbf{T_{cc}}} f \right\| = \cos(-\theta_3 - \alpha) \frac{\sin(\alpha)}{\sin(\pi + \theta_3)} \left\| {}^{\mathbf{T_{cc}}} f \right\| \qquad \text{(C.10)} \\
\Leftrightarrow \quad & \alpha_2 = \sin(\alpha) \frac{\cos(-\theta_3 - \alpha)}{\sin(\pi + \theta_3)}.
\end{aligned}$$

With some additional trigonometric simplifications, the equations for α_1 and α_2, given in (C.9) – (C.10) can be further simplified into

$$\alpha_1 = \frac{1}{2} + \frac{\sin(2\alpha + \theta_3)}{2\sin(\theta_3)} \qquad \text{(C.11)}$$

$$\alpha_2 = \frac{1}{2} - \frac{\sin(2\alpha + \theta_3)}{2\sin(\theta_3)}. \qquad \text{(C.12)}$$

From this format it can clearly be seen that $\alpha_1 + \alpha_2 = 1$. □

APPENDIX D. DERIVATION OF THE INTERNAL FORCE VECTOR

In this appendix the derivation of the *internal force vector*, ${}^{\mathbf{T_{cc}}}\boldsymbol{\eta} \in \mathbb{R}^6$ is presented. The internal force vector is used to satisfy joint constraints of the unactuated joints of the manipulator. In this case joints located at frames $\{\mathbf{T_{cc}}\}$, $\{\mathbf{B_{22}}\}$ and $\{\mathbf{B_{32}}\}$. In view of Assumption 1, the torque of the unactuated joints must be zero. This can be expressed as

$$\boldsymbol{z}_\tau^T \, {}^{\mathbf{T_2}}F = 0 \tag{D.1}$$

$$\boldsymbol{z}_\tau^T \, {}^{\mathbf{B_{22}}}F = 0 \tag{D.2}$$

$$\boldsymbol{z}_\tau^T \, {}^{\mathbf{B_{32}}}F = 0, \tag{D.3}$$

where

$$\boldsymbol{z}_\tau^T = \begin{bmatrix} 0 & 0 & 0 & 0 & 0 & 1 \end{bmatrix} \in \mathbb{R}^6. \tag{D.4}$$

The internal force vector is composed as shown below, with only three non-zero elements needed to satisfy the joint constrains defined in (D.1) – (D.3). The derivation of these three meaningful elements is shown in (D.5) – (D.25)

$${}^{\mathbf{T_{cc}}}\boldsymbol{\eta} = \begin{bmatrix} {}^{\mathbf{T_{cc}}}\boldsymbol{\eta}_{vx} \\ {}^{\mathbf{T_{cc}}}\boldsymbol{\eta}_{vy} \\ 0 \\ 0 \\ 0 \\ {}^{\mathbf{T_{cc}}}\boldsymbol{\eta}_{\omega z} \end{bmatrix} \tag{D.5}$$

The first joint constraint (D.1) can be satisfied with ${}^{\mathbf{T_{cc}}}\boldsymbol{\eta}_{\omega z}$ as follows

$$\boldsymbol{z}_\tau^T \, {}^{\mathbf{T_2}}F = 0 \tag{D.6}$$

$$\Leftrightarrow \quad \boldsymbol{z}_\tau^T \left(\alpha_2 {}^{\mathbf{T_{cc}}}F - {}^{\mathbf{T_{cc}}}\boldsymbol{\eta} \right) = 0 \tag{D.7}$$

$$\Leftrightarrow \quad \alpha_2 \, \boldsymbol{z}_\tau^T \, {}^{\mathbf{T_{cc}}}F - \boldsymbol{z}_\tau^T \, {}^{\mathbf{T_{cc}}}\boldsymbol{\eta} = 0 \tag{D.8}$$

$$\Leftrightarrow \quad \boldsymbol{z}_\tau^T \, {}^{\mathbf{T_{cc}}}\boldsymbol{\eta} = -\alpha_2 \, \boldsymbol{z}_\tau^T \, {}^{\mathbf{T_{cc}}}F \tag{D.9}$$

$$\Leftrightarrow \quad {}^{\mathbf{T_{cc}}}\boldsymbol{\eta}_{\omega z} = -\alpha_2 \, \boldsymbol{z}_\tau^T \, {}^{\mathbf{T_{cc}}}F \tag{D.10}$$

The second constraint at frame $\{\mathbf{B_{22}}\}$ can be solved in a similar manner as

$$
\begin{aligned}
& {\boldsymbol{z}_\tau^T}^{\mathbf{B_{22}}} F = 0 && \text{(D.11)}\\
\Leftrightarrow\quad & \boldsymbol{z}_\tau^T \left[{}^{\mathbf{B_{22}}}F^* + {}^{\mathbf{B_{22}}}\boldsymbol{U}_{\mathbf{T_{cc}}} \left(\alpha_1 \, {}^{\mathbf{T_{cc}}}F + {}^{\mathbf{T_{cc}}}\boldsymbol{\eta} \right) \right] = 0 && \text{(D.12)}\\
\Leftrightarrow\quad & \boldsymbol{z}_\tau^{T\,\mathbf{B_{22}}} F^* + \alpha_1 \, \boldsymbol{z}_\tau^{T\,\mathbf{B_{22}}} \boldsymbol{U}_{\mathbf{T_{cc}}} \, {}^{\mathbf{T_{cc}}}F + \boldsymbol{z}_\tau^{T\,\mathbf{B_{22}}} \boldsymbol{U}_{\mathbf{T_{cc}}} \, {}^{\mathbf{T_{cc}}}\boldsymbol{\eta} = 0 && \text{(D.13)}\\
\Leftrightarrow\quad & \boldsymbol{z}_\tau \, {}^{\mathbf{B_{22}}}\boldsymbol{U}_{\mathbf{T_{cc}}} \, {}^{\mathbf{T_{cc}}}\boldsymbol{\eta} = -\boldsymbol{z}_\tau^T \left({}^{\mathbf{B_{22}}}F^* + \alpha_1 \, {}^{\mathbf{B_{22}}}\boldsymbol{U}_{\mathbf{T_{cc}}} \, {}^{\mathbf{T_{cc}}}F \right) && \text{(D.14)}
\end{aligned}
$$

Left side of D.14 can be solved as

$$
\begin{aligned}
\boldsymbol{z}_\tau \, {}^{\mathbf{B_{22}}}\boldsymbol{U}_{\mathbf{T_{cc}}} \, {}^{\mathbf{T_{cc}}}\boldsymbol{\eta} = & \begin{bmatrix} 0 \\ 0 \\ 0 \\ 0 \\ 0 \\ 1 \end{bmatrix}^T \begin{bmatrix} 1 & 0 & 0 & 0 & 0 & 0 \\ 0 & 1 & 0 & 0 & 0 & 0 \\ 0 & 0 & 1 & 0 & 0 & 0 \\ 0 & 0 & 0 & 1 & 0 & 0 \\ 0 & 0 & -l_2 & 0 & 1 & 0 \\ 0 & l_2 & 0 & 0 & 0 & 1 \end{bmatrix} \begin{bmatrix} {}^{\mathbf{T_{cc}}}\boldsymbol{\eta}_{vx} \\ {}^{\mathbf{T_{cc}}}\boldsymbol{\eta}_{vy} \\ 0 \\ 0 \\ 0 \\ {}^{\mathbf{T_{cc}}}\boldsymbol{\eta}_{\omega z} \end{bmatrix} \\
= & l_2 \, {}^{\mathbf{T_{cc}}}\boldsymbol{\eta}_{vy} + {}^{\mathbf{T_{cc}}}\boldsymbol{\eta}_{\omega z}
\end{aligned} \qquad \text{(D.15)}
$$

By using the solution from (D.15), the second relevant element of the internal force vector can be solved from (D.14) as

$$
\begin{aligned}
& l_2 \, {}^{\mathbf{T_{cc}}}\boldsymbol{\eta}_{vy} + {}^{\mathbf{T_{cc}}}\boldsymbol{\eta}_{\omega z} = -\boldsymbol{z}_\tau^T \left({}^{\mathbf{B_{22}}}F^* + \alpha_1 \, {}^{\mathbf{B_{22}}}\boldsymbol{U}_{\mathbf{T_{cc}}} \, {}^{\mathbf{T_{cc}}}F \right) && \text{(D.16)}\\
\Leftrightarrow\quad & {}^{\mathbf{T_{cc}}}\boldsymbol{\eta}_{vy} = \frac{-\boldsymbol{z}_\tau^T \left({}^{\mathbf{B_{22}}}F^* + \alpha_1 \, {}^{\mathbf{B_{22}}}\boldsymbol{U}_{\mathbf{T_{cc}}} \, {}^{\mathbf{T_{cc}}}F \right) - {}^{\mathbf{T_{cc}}}\boldsymbol{\eta}_{\omega z}}{l_2} && \text{(D.17)}
\end{aligned}
$$

The last meaningful element of the internal force vector is the force along x-axis and it can be solved as

$$
\begin{aligned}
& {\boldsymbol{z}_\tau^T}^{\mathbf{B_{32}}} F = 0 && \text{(D.18)}\\
\Leftrightarrow\quad & \boldsymbol{z}_\tau^T \left[{}^{\mathbf{B_{32}}}F^* + {}^{\mathbf{B_{32}}}\boldsymbol{U}_{\mathbf{T_{cc}}} \left(\alpha_1 \, {}^{\mathbf{T_{cc}}}F - {}^{\mathbf{T_{cc}}}\boldsymbol{\eta} \right) \right] = 0 && \text{(D.19)}\\
\Leftrightarrow\quad & \boldsymbol{z}_\tau^{T\,\mathbf{B_{32}}} F^* + \alpha_2 \, \boldsymbol{z}_\tau^{T\,\mathbf{B_{32}}} \boldsymbol{U}_{\mathbf{T_{cc}}} \, {}^{\mathbf{T_{cc}}}F - \boldsymbol{z}_\tau^{T\,\mathbf{B_{32}}} \boldsymbol{U}_{\mathbf{T_{cc}}} \, {}^{\mathbf{T_{cc}}}\boldsymbol{\eta} = 0 && \text{(D.20)}\\
\Leftrightarrow\quad & \boldsymbol{z}_\tau \, {}^{\mathbf{B_{32}}}\boldsymbol{U}_{\mathbf{T_{cc}}} \, {}^{\mathbf{T_{cc}}}\boldsymbol{\eta} = \boldsymbol{z}_\tau^T \left({}^{\mathbf{B_{32}}}F^* + \alpha_2 \, {}^{\mathbf{B_{32}}}\boldsymbol{U}_{\mathbf{T_{cc}}} \, {}^{\mathbf{T_{cc}}}F \right) && \text{(D.21)}
\end{aligned}
$$

Similarly as in the case of the second joint constraint, the left side of equation (D.21) can

be solved as

$$
\begin{aligned}
&\boldsymbol{z}_\tau{}^{\mathbf{B32}}\boldsymbol{U}_{\mathbf{T_{cc}}} \\
&= \begin{bmatrix} 0 \\ 0 \\ 0 \\ 0 \\ 0 \\ 1 \end{bmatrix}^T \begin{bmatrix} \cos(\theta_3) & -\sin(\theta_3) & 0 & 0 & 0 & 0 \\ \sin(\theta_3) & \cos(\theta_3) & 0 & 0 & 0 & 0 \\ 0 & 0 & 1 & 0 & 0 & 0 \\ 0 & 0 & 0 & \cos(\theta_3) & -\sin(\theta_3) & 0 \\ 0 & 0 & -l_1 & \sin(\theta_3) & \cos(\theta_3) & 0 \\ l_1\,\sin(\theta_3) & l_1\,\cos(\theta_3) & 0 & 0 & 0 & 1 \end{bmatrix} \\
&= \begin{bmatrix} l_1\,\sin(\theta_3) & l_1\,\cos(\theta_3) & 0 & 0 & 0 & 1 \end{bmatrix}
\end{aligned} \tag{D.22}
$$

$$
\begin{aligned}
\boldsymbol{z}_\tau{}^{\mathbf{B32}}\boldsymbol{U}_{\mathbf{T_{cc}}}{}^{\mathbf{T_{cc}}}\boldsymbol{\eta} &= \begin{bmatrix} l_1\,\sin(\theta_3) & l_1\,\cos(\theta_3) & 0 & 0 & 0 & 1 \end{bmatrix} \begin{bmatrix} {}^{\mathbf{T_{cc}}}\boldsymbol{\eta}_{vx} \\ {}^{\mathbf{T_{cc}}}\boldsymbol{\eta}_{vy} \\ 0 \\ 0 \\ 0 \\ {}^{\mathbf{T_{cc}}}\boldsymbol{\eta}_{\omega z} \end{bmatrix} \\
&= l_1\,\sin(\theta_3)\,{}^{\mathbf{T_{cc}}}\boldsymbol{\eta}_{vx} + l_1\,\cos(\theta_3)\,{}^{\mathbf{T_{cc}}}\boldsymbol{\eta}_{vy} + {}^{\mathbf{T_{cc}}}\boldsymbol{\eta}_{\omega z}
\end{aligned} \tag{D.23}
$$

With the results from (D.23), the last element of the internal force vector can finally be solved from (D.21) as

$$
\begin{aligned}
& l_1\,\sin(\theta_3)\,{}^{\mathbf{T_{cc}}}\boldsymbol{\eta}_{vx} + l_1\,\cos(\theta_3)\,{}^{\mathbf{T_{cc}}}\boldsymbol{\eta}_{vy} + {}^{\mathbf{T_{cc}}}\boldsymbol{\eta}_{\omega z} \\
= \;& \boldsymbol{z}_\tau^T\left(\mathbf{B32}\,F^* + \alpha_2{}^{\mathbf{B32}}\boldsymbol{U}_{\mathbf{T_{cc}}}{}^{\mathbf{T_{cc}}}F\right)
\end{aligned} \tag{D.24}
$$

$$
\Leftrightarrow \quad {}^{\mathbf{T_{cc}}}\boldsymbol{\eta}_{vy}
$$

$$
= \frac{-\boldsymbol{z}_\tau^T\left(\mathbf{B32}\,F^* + \alpha_2{}^{\mathbf{B32}}\boldsymbol{U}_{\mathbf{T_{cc}}}{}^{\mathbf{T_{cc}}}F\right) - l_1\,\cos(\theta_3)\,{}^{\mathbf{T_{cc}}}\boldsymbol{\eta}_{vy} - {}^{\mathbf{T_{cc}}}\boldsymbol{\eta}_{\omega z}}{l_1\sin(\theta_3)} \tag{D.25}
$$

□

APPENDIX E. FORCE-SENSORLESS CONTACT FORCE ESTIMATION

In this appendix the derivation of the *exogenous force vector*, ${}^{\mathbf{S_{tcp}}}\boldsymbol{F} \in \mathbb{R}^3$ is presented. This force vector represents the exogenous force exerted by the operator toward the handle of the master manipulator. This method is necessary to estimate the external force because the Phantom Premium haptic manipulator is not equipped with a force sensor at the handle.

This appendix uses the assumption that the torques required to cancel the dynamics of the manipulator, has already been deducted from the torques. With this assumption, the torques $\boldsymbol{\tau_1}$, $\boldsymbol{\tau_2}$ and $\boldsymbol{\tau_3}$ are the corresponding motor torques, respectively.

The motors of the Phantom Premium are organized so that the motor 1 controls the rotation of the manipulator alone, while motor 2 and 3 control the xy-plane. Further it can be shown that although the motors 2 and 3 are located at the same location, the torques applied by motor 3 can be transfered directly to torques applied to the end of the first arm of the manipulator, due to geometric conditions. These conditions are that the first arm of the manipulator and the second link, connected to motor 3, are parallel and the torque arm of motor 3 and the second arm of the manipulator are parallel. This is also illustrated in Figure E.1.

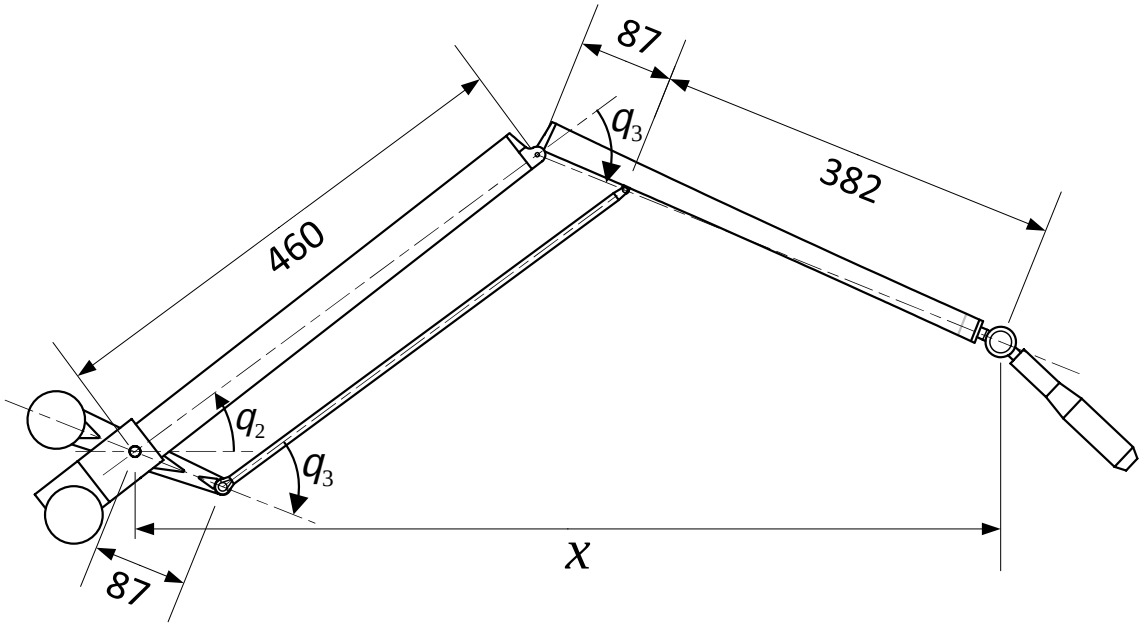

Figure E.1 *Geometric structure of the manipulator*

The distance x in the Figure E.1 can be solved using the kinematics equations defined in (3.6) as

$$l_1 \left(\cos\left(\theta_2 + \theta_3\right) + \cos\left(\theta_2\right)\right), \tag{E.1}$$

where l_1 denotes the length of the manipulator arm, which is $0.46m$.

The approach to estimate the external force at the manipulator handle can be divided into three parts. Firstly the torque generated by the external force at the connection point of the first and second arm is compensated by motor 3 torque. On the other hand, the external force can be transferred to act on the end of the first arm of the manipulator, in which case, the torque generated by the external force, on the base of the first arm, is compensated by the torque from motor 2. Thirdly, the torque generated by the z-component of the external force, is compensated by the torque of motor 1, located at the base of the manipulator. Figure E.2 illustrates the situation.

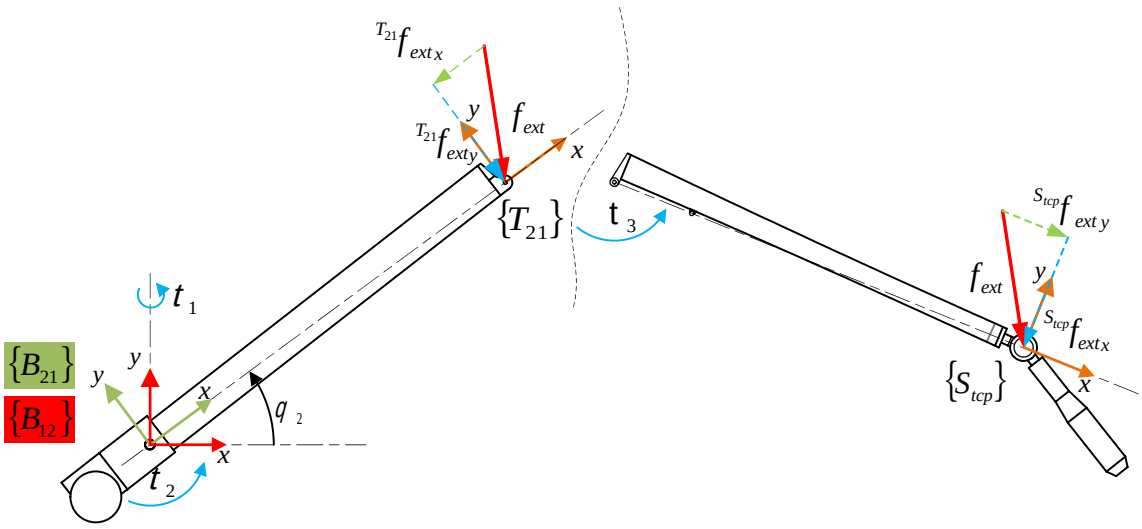

Figure E.2 *Exogenous force estimation of the manipulator handle*

The applied torques of each motor are known and from them, the component of f_{ext} directly perpendicular to the torque arm can be obtained. With three motors those components are $^{\mathbf{S_{tcp}}}f_{ext\,y}$, $^{\mathbf{S_{tcp}}}f_{ext\,z}$ and $^{\mathbf{T_{21}}}f_{ext\,y}$. Further it should be noted that the arms of the manipulator cannot align due to mechanical constraints of the manipulator, so a singular configuration of the manipulator is not possible.

All but the x-component of the external force f_{ext}, expressed in frame $\{\mathbf{S_{tcp}}\}$, can be determined in a rather straight forward manner. The last component of the external force

vector can be computed using equations (E.1)–(E.10).

$$\begin{aligned} {}^{\boldsymbol{S_{tcp}}}F_{ext} &= {}^{\boldsymbol{T_{21}}}\mathbf{R}_{\boldsymbol{S_{tcp}}}\, {}^{\boldsymbol{T_{21}}}F_{ext} \\ &= \begin{bmatrix} {}^{\boldsymbol{T_{21}}}f_{ext\,x}\cos(\theta_3) + {}^{\boldsymbol{T_{21}}}f_{ext\,y}\sin(\theta_3) \\ {}^{\boldsymbol{T_{21}}}f_{ext\,y}\cos(\theta_3) - {}^{\boldsymbol{T_{21}}}f_{ext\,x}\sin(\theta_3) \\ {}^{\boldsymbol{T_{21}}}f_{ext\,z} \end{bmatrix}, \end{aligned} \tag{E.2}$$

where ${}^{\boldsymbol{T_{21}}}F_{ext} \in \mathbb{R}^3$ is the external force expressed in frame $\{\boldsymbol{T_{21}}\}$ and

$${}^{\boldsymbol{T_{21}}}\mathbf{R}_{\boldsymbol{S_{tcp}}} = \begin{bmatrix} \cos(\theta_3) & \sin(\theta_3) & 0 \\ -\sin(\theta_3) & \cos(\theta_3) & 0 \\ 0 & 0 & 1 \end{bmatrix}. \tag{E.3}$$

On the other hand

$${}^{\boldsymbol{S_{tcp}}}F_{ext} = \begin{bmatrix} {}^{\boldsymbol{S_{tcp}}}f_{ext\,x} \\ {}^{\boldsymbol{S_{tcp}}}f_{ext\,y} \\ {}^{\boldsymbol{S_{tcp}}}f_{ext\,z} \end{bmatrix}. \tag{E.4}$$

Further

$${}^{\boldsymbol{S_{tcp}}}f_{ext\,y} = -\frac{\tau_3}{l_1} \tag{E.5}$$

$${}^{\boldsymbol{T_{21}}}f_{ext\,y} = -\frac{\tau_2}{l_1} \tag{E.6}$$

$${}^{\boldsymbol{S_{tcp}}}f_{ext\,y} = -\frac{\tau_3}{l_1\,(\cos(\theta_2+\theta_3)+\cos(\theta_2))}. \tag{E.7}$$

Using equations (E.2) and (E.4), ${}^{\boldsymbol{T_{21}}}f_{ext\,x}$ can be solved as

$${}^{\boldsymbol{S_{tcp}}}f_{ext\,y} = {}^{\boldsymbol{T_{21}}}f_{ext\,y}\cos(\theta_3) - {}^{\boldsymbol{T_{21}}}f_{ext\,x}\sin(\theta_3) \tag{E.8}$$

$$\Leftrightarrow \quad {}^{\boldsymbol{T_{21}}}f_{ext\,x} = \frac{{}^{\boldsymbol{T_{21}}}f_{ext\,y}\cos(\theta_3) - {}^{\boldsymbol{S_{tcp}}}f_{ext\,y}}{\sin(\theta_3)} \tag{E.9}$$

Finally substituting (E.1), (E.5), (E.6), (E.7) and (E.9) into (E.2) yields

$${}^{\boldsymbol{S_{tcp}}}F_{ext} = -\begin{bmatrix} \dfrac{\tau_2 - \tau_3\cos(\theta_3)}{l_1\sin(\theta_3)} \\ \dfrac{\tau_3}{l_1} \\ \dfrac{\tau_1}{l_1\,(\cos(\theta_2+\theta_3)+\cos(\theta_2))} \end{bmatrix}. \tag{E.10}$$